

UNIVERSITÉ DU QUÉBEC À MONTRÉAL

IMPROVING MODELS OF THE LAND THERMAL REGIME FOR  
CLIMATE SIMULATION

THESIS

PRESENTED

AS PARTIAL REQUIREMENT

OF THE DOCTORATE OF ENVIRONMENTAL SCIENCES

BY

IGNACIO HERMOSO DE MENDOZA NAVAL

APRIL 2019

UNIVERSITÉ DU QUÉBEC À MONTRÉAL

AMÉLIORATION DES MODÈLES DU RÉGIME THERMIQUE DU SOL  
DANS LA MODÉLISATION CLIMATIQUE.

THÈSE  
PRÉSENTÉE  
COMME EXIGENCE PARTIELLE  
DU DOCTORAT EN SCIENCES DE L'ENVIRONNEMENT

PAR  
IGNACIO HERMOSO DE MENDOZA NAVAL

AVRIL 2019

UNIVERSITÉ DU QUÉBEC À MONTRÉAL  
Service des bibliothèques

Avertissement

La diffusion de cette thèse se fait dans le respect des droits de son auteur, qui a signé le formulaire *Autorisation de reproduire et de diffuser un travail de recherche de cycles supérieurs* (SDU-522 – Rév.10-2015). Cette autorisation stipule que «conformément à l'article 11 du Règlement no 8 des études de cycles supérieurs, [l'auteur] concède à l'Université du Québec à Montréal une licence non exclusive d'utilisation et de publication de la totalité ou d'une partie importante de [son] travail de recherche pour des fins pédagogiques et non commerciales. Plus précisément, [l'auteur] autorise l'Université du Québec à Montréal à reproduire, diffuser, prêter, distribuer ou vendre des copies de [son] travail de recherche à des fins non commerciales sur quelque support que ce soit, y compris l'Internet. Cette licence et cette autorisation n'entraînent pas une renonciation de [la] part [de l'auteur] à [ses] droits moraux ni à [ses] droits de propriété intellectuelle. Sauf entente contraire, [l'auteur] conserve la liberté de diffuser et de commercialiser ou non ce travail dont [il] possède un exemplaire.»

## ACKNOWLEDGMENTS

I would like to thank in the first place Hugo Beltrami, who gave me this opportunity and provided the financial support, and Jean-Claude Mareschal, whose special charisma and reverence to Friday's drinking time played a special part in bringing our office together. This thesis would have not been possible without your involvement, thanks to your quality both in a professional and in a personal level.

I thank specially the core members of our office. Fernando, who showed me the possibility of doing this doctorate. Carolyne, who as fellow but more advanced PhD student, helped me so much. I specially thank you both for the patience you showed to me during my worst moments. Lidia, you made me enjoy this time ever since you stole that pickle. You are the only person I know crazy enough to make me feel normal. The time we four were together was the best part of these four years. Our office could not have been the same without you.

Thanks to the other members of our office. Petar for making me laugh so much, I have loved your jokes as much as your stories. It's crazy, you know? Our latest members, Anna and Omid, for preventing this office from becoming boring, and for giving me free food. Luping, for your time in this office was brief but fun. My predecessor Francesco, for giving us so many funny stories to talk about. Your legend continues through Dr. Francesco Fish, who lives to bite the hand that feeds him, and surprises everybody for having survived under my care. Thanks to Kim-Jon-Fridge as well, for you were the best 50\$ I ever invested.

Thanks to Fiona for bringing new members, to Dolors for discussing with me the

news from Spain nobody else cared about, and to both of you as well as Hanika and Alessandro for hanging out with our group.

My deepest gratitude to Rigoberto, the best friend I found in these four years. You supported me in my lowest point, when nobody else could. This thesis would have never been without you. *Quién encuentra un amigo, encuentra un tesoro.*

## CONTENTS

LIST OF TABLES . . . . .	vii
LIST OF FIGURES . . . . .	viii
LIST OF SYMBOLS . . . . .	xv
LIST OF ACRONYMS . . . . .	xvi
RÉSUMÉ . . . . .	xvii
ABSTRACT . . . . .	xix
INTRODUCTION . . . . .	1
CHAPTER I	
LOWER BOUNDARY CONDITIONS IN LAND SURFACE MODELS. PART	
1: HEAT STORAGE AND TEMPERATURE-DEPTH PROFILES. . . . .	10
1.1 Abstract . . . . .	10
1.2 Introduction . . . . .	11
1.3 Theoretical analysis . . . . .	14
1.3.1 Geothermal gradient . . . . .	17
1.4 Methodology . . . . .	18
1.4.1 Original Land Model . . . . .	18
1.4.2 Modifications of the original model . . . . .	20
1.4.3 Simulations . . . . .	21
1.5 Results . . . . .	24
1.5.1 Effect of the depth of the bottom boundary . . . . .	24
1.5.2 Effect of the bottom heat flux . . . . .	26
1.6 Discussion and conclusions . . . . .	27
CHAPTER II	
LOWER BOUNDARY CONDITIONS IN LAND SURFACE MODELS. PART	
2: EFFECTS ON THE PERMAFROST AND CARBON POOLS. . . . .	43

2.1	Abstract . . . . .	43	
2.2	Introduction . . . . .	44	
2.3	Methodology . . . . .	46	
2.3.1	Community Land Model 4.5 . . . . .	46	
2.3.2	Carbon model . . . . .	46	
2.3.3	Permafrost treatment . . . . .	48	
2.3.4	Simulation of the 1901-2300 period . . . . .	49	
2.4	Results: Permafrost . . . . .	51	
2.4.1	Intermediate-depth Permafrost . . . . .	51	
2.4.2	Near-surface permafrost . . . . .	52	
2.5	Results: Carbon . . . . .	53	
2.5.1	Soil Carbon . . . . .	53	
2.5.2	Vegetation Carbon . . . . .	55	
2.5.3	Methane . . . . .	56	
2.6	Discussion and Conclusions . . . . .	57	
2.7	Acknowledgements . . . . .	63	
CHAPTER III			
CONSTRAINTS ON GLACIER FLOW FROM TEMPERATURE-DEPTH PROFILES IN THE ICE. APPLICATION TO EPICA DOME C. . . . .			86
3.1	Abstract . . . . .	86	
3.2	Introduction . . . . .	87	
3.3	Basic assumptions and equations . . . . .	89	
3.4	Boundaries . . . . .	92	
3.4.1	Ice thickness history . . . . .	92	
3.4.2	Surface accumulation and SAT histories . . . . .	93	
3.4.3	Temperature offset and snow-firn cover . . . . .	94	
3.5	Methodology . . . . .	95	
3.5.1	Basal melting . . . . .	95	

3.5.2	Glacier movement . . . . .	96
3.5.3	Shear heating . . . . .	97
3.5.4	Free parameters . . . . .	98
3.6	Initial conditions . . . . .	99
3.7	Results . . . . .	99
3.8	Discussion and conclusions . . . . .	101
3.9	Acknowledgements . . . . .	104
	CONCLUSION . . . . .	115
	APPENDIX A	
	CONSTRAINTS ON GLACIER FLOW FROM TEMPERATURE-DEPTH PROFILES IN THE ICE. APPLICATION TO EPICA DOME C: NUMER- ICAL MODEL . . . . .	123
1.1	Layer discretization and thinning . . . . .	123
	APPENDIX B	
	CONSTRAINTS ON GLACIER FLOW FROM TEMPERATURE-DEPTH PROFILES IN THE ICE. APPLICATION TO EPICA DOME C: METHOD SENSITIVITY . . . . .	126
	APPENDIX C	
	CONSTRAINTS ON GLACIER FLOW FROM TEMPERATURE-DEPTH PROFILES IN THE ICE. APPLICATION TO EPICA DOME C: CALCU- LATION OF SHEAR HEATING . . . . .	129

## LIST OF TABLES

Table		Page
1.1	Heat stored in the subsurface since 1901 CE in the year 2000, and predicted for years 2100, 2200 and 2300 CE for the RCP 4.5 and RCP 8.5 scenarios. . . . .	41
1.2	Heat stored in the soil (upper 3.8 m) since 1901 CE in the year 2000 and predicted for the year 2300 CE for the RCP 4.5 and RCP 8.5 scenarios. . . . .	42
2.1	Areal extent of intermediate-depth permafrost at 1901 CE, 2000 CE and 2300 CE for the RCP 4.5 and RCP 8.5 scenarios. . . . .	84
2.2	Areal extent of near-surface permafrost at 1901 CE, 2000 CE and 2300 CE for the RCP 4.5 and RCP 8.5 scenarios. . . . .	85

## LIST OF FIGURES

Figure	Page
1.01 Departure from the initial temperature profile due to constant rate of surface temperature increase of $0.01 \text{ K yr}^{-1}$ . Analytical solutions for the half space model (black), and for the finite thickness model with bottom boundary at 42.1 m (blue) and at 342.1 m (red). a) Temperature anomaly after 100 yr. b) Temperature anomaly after 400 yr. . . . .	31
1.02 Heat absorbed by the land column per unit of area ( $Q$ ), following the start of a linear surface temperature increase of $0.01 \text{ K yr}^{-1}$ . a): $Q$ as a function of time for the half space model and two models of finite thicknesses 42.1 m and 342.1 m. b): $Q$ as a function of the thickness $d$ of the finite model, at 100 yr and 400 yr. . . . .	32
1.03 Mean Surface Air Temperature (SAT) over land relative to the 20th century mean, from the CRUNCEP dataset (black) and the RCP 4.5 (red) and RCP 8.5 (blue) scenarios. Data taken from Viovy (2018); Thomson et al. (2011); Riahi et al. (2011). . . . .	33
1.04 Heat stored in the subsurface as function of time, for models of subsurface thickness $d$ of 42.1 m (black), 92.1 m (blue) 192.1 m (red) and 342.1 m (green). a) Simulations forced with CRUNCEP + RCP 4.5 data. b) Simulations forced with CRUNCEP + RCP 8.5 data. Note the scale difference between scenarios RCP 4.5 and RCP 8.5. . . . .	34
1.05 Heat stored in the subsurface as function of subsurface thickness, at the years 2000 (black), 2100 (blue), 2200 (red) and 2300 (green). a) Simulations forced with CRUNCEP + RCP 4.5 data. b) Simulations forced with CRUNCEP + RCP 8.5 data. Note the scale difference between scenarios RCP 4.5 and RCP 8.5. . . . .	35

1.06	Heat stored in the upper 42.1 m as function of time, for models of subsurface thickness $d$ of 42.1 m (black), 92.1 m (blue) 192.1 m (red) and 342.1 m (green). a) Simulations forced with CRUNCEP + RCP 4.5 data. b) Simulations forced with CRUNCEP + RCP 8.5 data. Note the scale difference between scenarios RCP 4.5 and RCP 8.5. . . . .	36
1.07	Heat stored in the soil (upper 3.8 m), for models of subsurface thickness $d$ of 42.1 m (black), 92.1 m (blue) 192.1 m (red) and 342.1 m (green). a) Simulations forced with CRUNCEP + RCP 4.5 data. b) Simulations forced with CRUNCEP + RCP 8.5 data. Note the scale difference between scenarios RCP 4.5 and RCP 8.5.	37
1.08	Heat stored in the soil as function of subsurface thickness, as fraction of that the thinnest model ( $d=42.1$ m). Years 2000 (black), 2100 (blue), 2200 (red) and 2300 (green). a) Simulations forced with CRUNCEP + RCP 4.5 data. b) Simulations forced with CRUNCEP + RCP 8.5 data. . . . .	38
1.09	Heat stored in the upper 42.1 m (the thickness of all models is 42.1 m) as function of crustal heat flux, relative to the initial heat content of the original model ( $F_B = 0$ W m <sup>-2</sup> ). The heat content in each model is a static shift from that of the original model. a) Simulations forced with CRUNCEP + RCP 4.5 data. b) Simulations forced with CRUNCEP + RCP 8.5 data. Note the scale difference between scenarios RCP 4.5 and RCP 8.5. . . . .	39
1.10	Heat stored in the soil (upper 3.8 m) as function of crustal heat flux, referenced to the initial heat content of the original model ( $F_B = 0$ W m <sup>-2</sup> ). a) Simulations forced with CRUNCEP + RCP 4.5 data. b) Simulations forced with CRUNCEP + RCP 8.5 data. Note the scale difference between scenarios RCP 4.5 and RCP 8.5.	40
2.01	Schema of the carbon flux in CLM4.5-BGC. Figure redrawn from Oleson et al. (2013). . . . .	64
2.02	Region of study (blue), which corresponds to the extent of near-surface permafrost in the Northern Hemisphere in the year 1901, for the original CLM4.5 model. . . . .	65
2.03	Mean Surface Air Temperature (SAT) over the region of study relative to the 20th century mean, from the CRUNCEP dataset (black) and the RCP 4.5 (red) and RCP 8.5 (blue) scenarios. . . . .	66

2.04	Northern Hemisphere intermediate-depth (0-42.1 m) permafrost area as function of time. Model versions with bottom boundary depth $d$ at 42.1 m (black), 92.1 m (blue) 192.1 m (red) and 342.1 m (green). a) Simulations forced with CRUNCEP + RCP 4.5 data. b) Simulations forced with CRUNCEP + RCP 8.5 data. . . . .	67
2.05	Northern Hemisphere intermediate-depth permafrost area as function of subsurface thickness $d$ , at the years 2000 (black), 2100 (blue), 2200 (red) and 2300 (green). a) Simulations forced with CRUNCEP + RCP 4.5 data. b) Simulations forced with CRUNCEP + RCP 8.5 data. . . . .	68
2.06	Northern Hemisphere intermediate-depth permafrost area as function of time. Model versions using different heat flux as bottom boundary. a) Simulations forced with CRUNCEP + RCP 4.5 data. b) Simulations forced with CRUNCEP + RCP 8.5 data. . . . .	69
2.07	Northern Hemisphere near-surface permafrost area as function of time. Model versions with bottom boundary depth at 42.1 m (black), 92.1 m (blue) 192.1 m (red) and 342.1 m (green). a) Simulations forced with CRUNCEP + RCP 4.5 data. b) Simulations forced with CRUNCEP + RCP 8.5 data. . . . .	70
2.08	Northern Hemisphere near-surface permafrost area as function of time. Models using different heat flux as bottom boundary. a) Simulations forced with CRUNCEP + RCP 4.5 data. b) Simulations forced with CRUNCEP + RCP 8.5 data. . . . .	71
2.09	Active Layer Thickness for the unmodified model (top)), and differences to the original model at each time frame for the modified model with $F_B = 80 \text{ mW m}^{-2}$ (middle) and the modified model with $d = 342.1 \text{ m}$ (bottom). Time frames at 1901 CE and 2300 CE for the scenarios RCP 4.5 and RCP 8.5. . . . .	72
2.10	Evolution of soil carbon pool in the Northern Hemisphere permafrost region, compared to the size for the original model at 1901 CE. Models with varying bottom boundary depth. a) Simulations forced with CRUNCEP + RCP 4.5 data. b) Simulations forced with CRUNCEP + RCP 8.5 data. Note the different vertical scale in panel a and b. . . . .	73

2.11	Evolution of soil carbon pool in the Northern Hemisphere permafrost region, compared to the size for the original model at 1901 CE. Models with varying basal heat flux. a) Simulations forced with CRUNCEP + RCP 4.5 data. b) Simulations forced with CRUNCEP + RCP 8.5 data. Note different vertical scale in panel a and b. . . . .	74
2.12	Distribution of soil carbon for the original model (top) in $kgC/m^2$ , and differences to the original model at each time frame for the modified model with $F_B = 0.08 \text{ W m}^{-2}$ (middle) and the modified model with $d = 342.1 \text{ m}$ (bottom), in $gC/m^2$ . Time frames at 1901 CE and 2300 CE for the scenarios RCP 4.5 and RCP 8.5. . . . .	75
2.13	Mean size of the soil carbon pool in the Northern Hemisphere permafrost region between 1901-1910, as function of basal heat flux. . . . .	76
2.14	Vegetation carbon pool in the Northern Hemisphere permafrost region. Models with varying bottom boundary depth. b) Simulations forced with CRUNCEP + RCP 8.5 data. . . . .	77
2.15	Vegetation carbon pool in the Northern Hemisphere permafrost region. Models with varying basal heat flux. a) Simulations forced with CRUNCEP + RCP 4.5 data. b) Simulations forced with CRUNCEP + RCP 8.5 data. . . . .	78
2.16	Distribution of vegetation carbon for the original model (top), and differences to the original model at each time frame for the modified model with $F_B = 0.08 \text{ W m}^{-2}$ (middle) and the modified model with $d = 342.1 \text{ m}$ (bottom). Time frames at 1901 CE and 2300 CE for the scenarios RCP 4.5 and RCP 8.5. . . . .	79
2.17	Mean size between 1901-1910 of the vegetation carbon pool in the Northern Hemisphere permafrost region, for models of different bottom heat flux. . . . .	80
2.18	Distribution of methane yearly production for the original model (top), and differences to the original model at each time frame for the modified model with $F_B = 0.08 \text{ W m}^{-2}$ (middle) and the modified model with $d = 342.1 \text{ m}$ (bottom). Time frames at 1901 CE and 2300 CE for the scenarios RCP 4.5 and RCP 8.5. . . . .	81

2.19	Global yearly methane production as function of time, moving average of 10 years. Models with varying bottom boundary depth. a) Simulations forced with CRUNCEP + RCP 4.5 data. b) Simulations forced with CRUNCEP + RCP 8.5 data. . . . .	82
2.20	Global yearly methane production as function of time, moving average of 10 years. Models with varying basal heat flux. a) Simulations forced with CRUNCEP + RCP 4.5 data. b) Simulations forced with CRUNCEP + RCP 8.5 data. . . . .	83
3.01	(a): Vertical temperature profile measured in Dome C. (b): Conductive heat flux profile, calculated from the temperature profile by Fourier law with a temperature-dependent thermal conductivity. Heat flux has been truncated for the upper 225 m because the temperature profile is very noisy near the surface of the ice sheet.	106
3.02	Sketch of flow in an ice sheet. The velocity of ice particles, both vertical and horizontal components, is highest near the surface and decreases at depth. The ice motion thins the ice layers and reduces the height of the glacier, while accumulation of snow at the surface increases its height. Temperature in the ice sheet increases downward, as heat flows out of the bedrock, and melting of ice could happen at the base. The ratio of the horizontal components of velocities at the bottom and at the surface of the ice defines the sliding ratio $s$ . . . . .	107
3.03	Variations of thickness in Dome C for the last 800 kyr, simulated with the linear perturbation model developed in Parrenin et al. (2007b). . . . .	108
3.04	Surface accumulation rate history (in ice-equivalent units). . . . .	109
3.05	Surface Air Temperature (SAT) history. . . . .	110
3.06	(a) Temperature-depth and (b) heat flux-depth profiles obtained at the end of the simulation with different values for the parameters $n$ and $p$ . Note how shear heating influences the shape of the temperature and heat flux profiles. The other parameters for these calculations are $q_b = 49.4 \text{ mW m}^{-2}$ , $v_{\text{sur}} = 0.015 \text{ m yr}^{-1}$ , and $T_{\text{offset}} = 0 \text{ K}$ . . . . .	111
3.07	Histograms of retained values for the free parameters: (a) basal flux, (b) IST-SAT temperature offset, (c) Glen's exponent $n$ , (d) flux function parameter $p$ , and (e) sliding parameter $s$ . . . . .	112

- 3.08 (a): Temperature-depth profile of Dome C (black) versus a simulation using  $p = 1.8$  and  $s = 0.14$  and the most likely values of the other parameters  $q_b = 51.1 \text{ mW m}^{-2}$ ,  $n = 1.91$  and  $T_{\text{offset}} = 0.36 \text{ K}$  (blue). (b): Conductive heat flux profile determined from the temperature profile, measured at Dome C (black) and calculated for the most likely values (blue). . . . . 113
- 3.09 (a): Temperature-depth profile and (b) conductive heat flux profile determined from the temperature profile, measured at Dome C (black), calculated with artificially made zero shear heating (blue), calculated with shear heating and the theoretical value of the flux shape function parameter  $p = 9$ , and calculated with shear heating but  $p = 2$ . The values of the other parameters in the simulated profiles are  $n = 3$ ,  $s = 0.1$ ,  $q_b = 49.4 \text{ mW m}^{-2}$  and  $T_{\text{offset}} = 0 \text{ K}$ . . 114
- 2.01 Change in the position of the  $q_b$  peak, as function of: a) The temperature cutoff  $T_{\text{cutoff}}$ , with heat flux cutoff set to  $q_{\text{cutoff}} = 2 \text{ mW m}^{-2}$ , and b) The heat flux cutoff  $q_{\text{cutoff}}$ , with temperature cutoff set to  $T_{\text{cutoff}} = 0.7 \text{ K}$ . . . . . 128

## LIST OF SYMBOLS

- $F_B$  Heat flux used as bottom boundary condition ( $\text{W m}^{-2}$ ).
- $H$  Height of the glacier (m).
- $T_{\text{offset}}$  Temperature offset between the atmosphere the ice surface (K).
- $\Omega$  Rate of heat production per unit volume ( $\mu\text{W m}^{-3}$ ).
- $\kappa$  Thermal diffusivity ( $\text{m}^2 \text{s}^{-1}$ ).
- $\lambda$  Thermal conductivity ( $\text{W m}^{-1} \text{K}^{-1}$ ).
- $\omega$  Flux shape function for the glacier (unitless).
- $\rho$  Density ( $\text{kg m}^{-3}$ ).
- $\zeta$  Adimensional vertical coordinate for the glacier (unitless).
- $a$  Snow accumulation in ice equivalent units ( $\text{m y}^{-1}$ ).
- $c$  Volumetric heat capacity ( $\text{J m}^{-3} \text{K}^{-1}$ ).
- $c_p$  Specific heat ( $\text{J kg}^{-1} \text{K}^{-1}$ ).
- $d$  Depth of the bottom boundary for the finite thickness model (m).
- $m$  Melting rate at the bottom of the glacier ( $\text{m y}^{-1}$ ).
- $n$  Glen's exponent (unitless).

$p$  Flux function parameter or parameter determining the shear deformation component of the flux shape function in Lliboutry's approximation (unitless).

$q$  Conductive heat flow ( $\text{W m}^{-2}$ ).

$q_b$  Basal heat flux at the bottom of the glacier ( $\text{W m}^{-2}$ ).

$s$  Sliding ratio (unitless).

$t$  Time coordinate (yr).

$z$  Vertical coordinate (m).

## LIST OF ACRONYMS

**ALT** Active Layer Thickness.

**BGC** BioGeoChemistry.

**CESM1.2** Community Earth System Model version 1.2.

**CLM4.0** Community Land Model version 4.0.

**CLM4.5** Community Land Model version 4.5.

**CLM5.0** Community Land Model version 5.0.

**CMIP5** Climate Model Intercomparison Project phase 5.

**CN** Carbon-Nitrogen.

**CRU-TS** Climate Research Unit Time-Series.

**ESM** Earth System Model.

**GST** Ground Surface Temperature.

**IST** Ice Surface Temperature.

**LSM** Land Surface Model.

**NCEP** National Centers for Environmental Prediction.

**RCP** Representative Concentration Pathway.

**SAT** Surface Air Temperature.

## RÉSUMÉ

La modélisation numérique des processus thermiques souterrains dans les modèles de surface terrestre nécessite l'utilisation de conditions aux limites inférieures appropriées pour le sous-sol. Cette thèse est divisée en trois chapitres: les deux premiers traitent de la modification des conditions aux limites du sous-sol dans un modèle climatique, afin d'obtenir des profils de température réalistes et d'étudier leurs conséquences, tandis que le troisième concerne l'application d'un modèle numérique d'un glacier pour obtenir des contraintes d'écoulement glaciaire à partir du profil de température vertical.

Le premier chapitre examine les problèmes découlant de l'utilisation de modèles de surface terrestre avec une limite inférieure du sous-sol excessivement peu profondes dans les simulations climatiques, ainsi que les effets du flux de chaleur nul à cette limite inférieure. Une limite inférieure peu profonde reflète l'énergie à la surface, ce qui, associé à l'absence de gradient géothermique, modifie le bilan énergétique de surface et l'état thermique à long terme du sous-sol. Nous décrivons le modèle de subsurface dans le Community Land Model version 4.5 (CLM4.5) et les modifications introduites pour obtenir une limite inférieure suffisamment profonde pour le sous-sol et un flux de chaleur de la croûte non nul à la limite inférieure pour induire un gradient géothermique. Nous opérons les versions modifiées et originales du CLM4.5 entre 1901 et 2300, en utilisant le forçage historique au cours de la période 1901-2005 et deux scénarios futurs d'émissions modérées (RCP 4.5) et élevées (RCP 8.5) entre 2005-2300. L'augmentation de l'épaisseur du sous-sol de 42.1 à 342.1 m augmente la chaleur stockée dans le sous-sol entre 1901 et 2300 de 217% (RCP 4.5) à 260% (RCP 8.5). En utilisant le flux de chaleur continental moyen  $60 \text{ mW m}^{-2}$  à la base du modèle, la température à la frontière sol-substrat (3.8 m de profondeur) augmente de  $0.12 \pm 0.03 \text{ K}$  et à la base (42.1 m de profondeur) de  $0.8 \pm 0.04 \text{ K}$ , indépendamment du scénario.

En modifiant l'état thermique du sous-sol et le bilan énergétique de surface, la limite inférieure affecte d'autres éléments du modèle de surface terrestre, tels que le pergélisol, le carbone du sol, la végétation et la production de méthane. Le deuxième chapitre examine comment ces processus sont affectés au cours de la période 1901-2300 dans les mêmes simulations que celles décrites dans le deuxième chapitre. L'augmentation de l'épaisseur du sous-sol de 42.1 à 342.1 m réduit de 1.6% (RCP 4.5) à 1.9% (RCP 8.5) la perte de pergélisol près de la surface entre

1901 et 2300, et réduit la perte de carbone dans le sol de 1.6% (RCP 4.5) à 3.6% (RCP 8.5). Un flux de chaleur crustal de  $80 \text{ mW m}^{-2}$  a peu d'effet sur l'étendue du pergélisol, mais il réduit la perte de carbone dans le sol de 4.4% (RCP 4.5) à 22.4% (RCP 8.5). Ces effets sont non négligeables, ce qui suggère que l'utilisation de conditions de base appropriées pour le sous-sol est nécessaire pour obtenir une représentation robuste, non seulement du régime thermique terrestre, mais aussi des processus se produisant dans la surface et le sous-sol peu profond.

Le troisième chapitre présente un modèle numérique de l'écoulement vertical de la glace et de la génération et de la conduction de la chaleur dans un glacier. Il est appliqué au profil de température mesuré dans le forage à EPICA Dome C dans l'Antarctique de l'Est. Ce modèle utilise l'histoire de la température de l'air en surface, de l'accumulation de neige et de la hauteur du glacier en tant que conditions limites et calcule le profil vertical actuel de la température, qui dépend de plusieurs paramètres (inconnus) de l'écoulement glaciaire. Nous utilisons la méthode de Monte-Carlo pour obtenir des contraintes sur ces paramètres: nous explorons l'espace des paramètres et comparons les profils de température calculés avec le profil mesuré pour trouver des distributions de probabilités pour les paramètres inconnus. Nous avons déterminé un flux de chaleur de la croûte de  $51.1 \pm 1.4(2\sigma) \text{ mW m}^{-2}$ , supérieur à la valeur apparente (mesurée directement à la base du glacier). Nous avons trouvé une valeur pour l'exposant de Glen de  $1.91 \pm 0.11(2\sigma)$  et un couplage de température air-glace de  $0.36 \pm 1.2(2\sigma) \text{ K}$ . Le rapport de glissement est limité à une valeur maximale de 0.4 et le paramètre de la fonction flux à une valeur maximale de 7.4, avec un intervalle de confiance  $2\sigma$ . Notre modèle est capable d'obtenir des valeurs bien contraintes pour les paramètres les plus importants de l'écoulement de la glace. Le modèle peut être appliqué à d'autres sites, mais les résultats peuvent être affectés par des valeurs élevées de fusion à la base du glacier.

Mots clés: Modèles climatiques, modèles de surface terrestre, flux thermique, températures souterraines, limite inférieure, gradient géothermique.

## ABSTRACT

Numerical modelling of subsurface thermal processes in land surface models requires the use of appropriate bottom boundary conditions for the subsurface. This thesis is divided in three chapters: the first two deal with the modification of the land subsurface boundaries in a climate model to obtain realistic temperature profiles and a study of its consequences, while the last concerns the application of a numerical model of a glacier to obtain constraints of glacier flow from the vertical temperature profile.

The first chapter examines the problems that arise from the use of land surface models with too-shallow subsurface bottom boundaries in climate simulations and also the effect of zero heat flux at such bottom boundary. Shallow bottom boundaries reflect energy to the surface, which along with the lack of a geothermal gradient, alters the surface energy balance and the long-term thermal state of the subsurface. We describe the subsurface model in the Community Land Model version 4.5 (CLM4.5) and the modifications introduced to obtain a sufficiently deep bottom boundary for the subsurface and a non-zero crustal heat flux added at the bottom boundary to induce a geothermal gradient. We run the modified and original CLM4.5 between 1901 and 2300, using historical forcing during the period 1901-2005 and two future scenarios of moderate (RCP 4.5) and high (RCP 8.5) emissions between 2005-2300. Increasing the thickness of the subsurface from 42.1 m to 342.1 m increases the heat stored in the subsurface between 1901 and 2300 by 217% (RCP 4.5) to 260% (RCP 8.5). Using the mean continental heat flux  $60 \text{ mW m}^{-2}$  at the bottom of the model rises the temperature at the soil-bedrock frontier (3.8 m depth) by  $0.12 \pm 0.03 \text{ K}$  and the bottom of the model (42.1 m depth) by  $0.8 \pm 0.04 \text{ K}$ , independently of the scenario.

By altering the thermal state of the subsurface and the surface energy balance, the bottom boundary affects other elements of the land surface model such as permafrost, soil carbon, vegetation, and methane production. The second chapter investigates how these processes are affected during the period 1901-2300 in the same simulations as those described in the second chapter. Increasing the thickness of the subsurface from 42.1 m to 342.1 m reduces the loss of near-surface permafrost between 1901 and 2300 by 1.6% (RCP 4.5) to 1.9% (RCP 8.5), and reduces the loss of soil carbon by 1.3% (RCP 4.5) to 3.6% (RCP 8.5). A crustal heat flux of  $80 \text{ mW m}^{-2}$  has a small effect on permafrost extent, but it reduces

the loss of soil carbon by 4.4% (RCP 4.5) to 22.4% (RCP 8.5). In the local scale these differences can be one order of magnitude with respect to the original model. These effects are non-negligible, which suggests that the use appropriate bottom boundary conditions for the subsurface is necessary to obtain a robust representation, not only of the land thermal regime, but also of the processes taking place in the surface and the shallow subsurface.

The third chapter introduces a numerical model of vertical ice flow and the generation and conduction of heat in a glacier. It is applied to the temperature profile measured at EPICA Dome C in East Antarctica. This model uses histories of surface air temperature, snow accumulation and glacier height as boundary conditions, and calculates the present vertical profile of temperature, which is dependent on several (unknown) parameters of glacier flow. We use the Monte-Carlo method to obtain constraints on these parameters, we compare the calculated temperature profiles with the measured profile and explore the parameter space to find probability distributions for the unknown parameters. We determined a basal heat flux  $51.1 \pm 1.4(2\sigma)$  mW m<sup>-2</sup>, higher than the apparent value (measured directly at the base of the glacier). We found a value for the Glen's exponent of  $1.91 + 0.11(2\sigma)$  and an air-ice temperature coupling of  $0.36 \pm 1.2(2\sigma)$  K. The sliding ratio is constrained to a maximum value of 0.4 and the flux function parameter to a maximum value of 7.4, with a  $2\sigma$  confidence interval. Our model is able to obtain well constrained values for the most important parameters of ice flow. The model can be applied to other sites, but the results of the Monte-Carlo method can be affected by high values of melting at the base of glacier.

Keywords: Climate models, land surface models, heat flow, subsurface temperatures, bottom boundary, geothermal gradient.

## INTRODUCTION

The numerical modeling of the climatic system is a valuable tool for scientists to understand climate. Climatic models are used for a variety of purposes, from studying the dynamics of the climate system to weather forecast. One of the most common applications of climate models is the study of climate change and the investigation of the impacts of the perturbations caused by human activities. Projections of future climate are based on ensembles of Earth System Models (ESMs), large numerical models including the different subsystems of Earth's climate, the oceans, the atmosphere, the land, the cryosphere and the biosphere, coupled together (Stocker et al., 2013).

Modeling of climate is a difficult task, as the natural processes that influence Earth's climate are numerous and complex. Climate modelers have been historically been limited by their capacity to understand and model these processes, as well as by the computational resources available to them. Starting from the relatively simple early climate models (Phillips, 1956), ESMs have improved incrementally, building on previous generations of ESMs as the understanding of climatic processes and our computational capabilities kept improving (McGuffie & Henderson-Sellers, 2001). Because of the large scope of this task, modelers prioritize their efforts on the processes they consider most important for a model, which means the modeling of some natural processes can be temporally neglected in favor of others.

While the circulation of the atmosphere and the oceanic currents are the main drivers of Earth's climate, the land system plays an important role in it through

the interactions between the land and the atmospheric and oceanic circulation. For instance, the land's vegetation stores atmospheric carbon, which over time becomes part of the soil carbon pools (Scharlemann et al., 2014), soil color type and snow cover play important roles in the surface's energy budget through the albedo (Hansen & Nazarenko, 2004), and the land hydrology also affects the ocean's thermohaline circulation through river freshwater discharge (Bray, 1988). Therefore, the models of the land system or Land Surface Models (LSMs) have evolved to provide more precise descriptions of the surface energy balance (Pitman, 2003; Hansen & Nazarenko, 2004), the surface water balance (Seneviratne et al., 2010), vegetation and land use (Bonan, 2008), and carbon dynamics (Ramanathan & Carmichael, 2008).

When this thesis was started, the latest generation of LSMs was integrated in the ESMs that formed part of the Climate Model Intercomparison Project phase 5 (CMIP5) (Taylor et al., 2012). These LSMs include more complex and more complete descriptions of natural processes than the previous generation of LSMs, specially for carbon dynamics, vegetation and land use (Oleson et al., 2013; Best et al., 2011; Ji et al., 2014; Friend & Kiang, 2005; Schmidt et al., 2014; Weaver et al., 2001). However, there are important limitations in the modeling of the subsurface across these models. Among several simplifications, such as an homogeneous and unrealistically shallow regolith thickness or an hydrology restricted to the soil, most of these models lack a geothermal gradient and use an excessively shallow bottom boundary for the subsurface (Cuesta-Valero et al., 2016).

The main justification to exclude the geothermal gradient and restrict the subsurface model to the upper subsurface is that, in the short time scale, the deep subsurface does not interact with climate. Most LSMs place the bottom boundary of the subsurface at a depth of 3-4 m, which is considered adequate for basic hydrology calculations, root uptake and carbon dynamics (Cuesta-Valero et al.,

2016). At such depth, the effect of the geothermal gradient (with a global average value of  $\sim 0.02\text{K/m}$  (Jaupart & Mareschal, 2015)) is very small, and it is thus ignored in the LSMs. However, this depth is too shallow to properly model the long-term thermal behavior of the subsurface (MacDougall et al., 2008, 2010).

The dynamics for the propagation into the subsurface of long trends of temperature at the surface of the land system are well known (Carslaw & Jaeger, 1959). As a periodic thermal signal propagates into the subsurface, it is attenuated exponentially in depth, with a skin depth proportional to the square root of the period of the signal. Similarly, the time that a periodic thermal signal from the surface takes to reach a given depth is proportional to the square of this depth (Lesperance et al., 2010). This relationship allows borehole climatology to use the thermal profiles of the subsurface to reconstruct the past Ground Surface Temperature (GST) history. The reconstruction of long GST histories requires deep boreholes: boreholes of few hundred meters are only used to reconstruct events more recent than 500 yr, and boreholes of  $\sim 1500$  m are used to reconstruct climate variations on the scale of 10 to 100 kyr (Pickler et al., 2016).

This relationship between the depth reached by a thermal signal and the time that it takes for the signal to reach such depth is at the root of our concerns. State of the art ESMs in the CMIP5 are currently used to project future climate change during the next 100 to 300 yr (Stocker et al., 2013). However, the LSMs used in these ESMs place the bottom boundary at depths of 3.5 to 10 m (Cuesta-Valero et al., 2016), with one exception of 42.1 m (Oleson et al., 2013). Such depths are much smaller than those reached by centennial trends of surface temperature. As the bottom boundary in LSMs uses a constant heat flux, it acts like a barrier for the propagation of heat, and therefore an insufficient depth affects the propagation of thermal signals underground. This has been shown in theoretical estimates of the heat stored by the subsurface during a ESM simulation of the 21st century

show a one order of magnitude difference between models using subsurface thicknesses of 10 m and 600 m (MacDougall et al., 2008). Not only does this severely underestimate the amount of heat absorbed by the subsurface, but as the thermal signal is unable to propagate past the bottom boundary, it is reflected upwards, thus creating a disturbance in the portion of the subsurface that is being simulated. To avoid reflected heat signals to affect the thermal profiles, the bottom boundary of the LSMs used in ESMs must be sufficiently deep for the duration of the simulations.

As the lack of geothermal gradient and the insufficient depth of the bottom boundary perturb the thermal profiles of the subsurface, they will also affect other subsystems of a LSM that are dependent on the temperature of the subsurface. In particular, the carbon dynamics could be significantly affected. The metabolic rates of the microorganisms that intervene in the decay of organic matter or in the production of methane are sensitive to temperature, which creates a feedback between the activity of these microorganisms in the land system, and the greenhouse gas concentrations and temperatures in the atmospheric system (Heimann & Reichstein, 2008). In addition, because a LSM of insufficient subsurface thickness overestimates the speed at which the upper subsurface adapts to variations in atmospheric temperatures, it also underestimates the stability of permafrost. Changes in extension or depth of permafrost in a LSM has further repercussions in hydrology and microbial activity.

The geothermal gradient and an adequate depth of the bottom boundary are therefore two key elements, necessary for modeling the land thermal regime, that are absent in current LSMs. Their impact can be estimated analytically in terms of heat absorption by the subsurface (Stevens et al., 2007), but to know their effect on other subsystems of the land model requires to use numerical simulations.

The main objective of this thesis is to determine and analyze the effect of a too shallow bottom boundary and a nul geothermal gradient in a LSM. With this, we aim to convince modelers of the significance of these two limitations, and lead them to overcome these limitations in future LSMs. While the lack of geothermal gradient and an excessively shallow subsurface are far from being the only limitations of current LSMs, we have to limit the scope of our project, because of the limited time and resources available to us. In the same way as LSMs are improved incrementally, expanding and developing the different parts of a model one step at a time, we have focused on the improvement of the land thermal regime.

This thesis is presented as three different chapters in the form of three scientific articles. The three articles share a common theme: the use of numerical models to study the propagation of long trends of air surface temperature into the subsurface, and how the resulting temperature-depth profiles depend on the characteristics of the subsurface model.

The first and second chapters of this thesis correspond to one scientific article that was originally planned to be published in two parts, but that was finally submitted as one single paper. This article has been accepted for publication in *Geoscientific Model Development*, under the title «Lower boundary conditions in Land Surface Models. Effects on the permafrost and the carbon pools: a case study with CLM 4.5», and as for March 2019 it is in discussion phase. In these two chapters we develop the main subject of the thesis, analyzing the effect of excessively shallow bottom boundaries and lack of geothermal gradient in LSMs. To that end, we modify the Community Land Model version 4.5 (CLM4.5) (Oleson et al., 2013). We create new versions of this model by either increasing the depth of the bottom boundary or by using different values of bottom heat flux. To compare these new versions with the original CLM4.5, we run numerical simulations where these

different versions are subject to the same set of atmospheric forcings (temperature, precipitation, solar radiation, winds and atmospheric pressure).

In the first chapter, we develop the theoretical framework for the propagation of surface thermal signals into the subsurface, and the relationship between the time scale of the surface signals and the depth at which they propagate, from where we obtain estimates of how the depth of the bottom boundary affects the propagation of heat underground. We describe the subsurface model in CLM4.5 and explain how we modify the model to increase to depth of the bottom boundary and to change the basal heat flux. We also provide a complete description of the numerical experiments and the set of atmospheric data used to force the CLM4.5 during the simulations. Finally, we analyze the propagation of the surface thermal signal into the subsurface for the different versions of the CLM4.5.

In the second chapter, we expand the numerical simulations described in the first chapter, to investigate the effects of the geothermal gradient and the thickness of the subsurface on several elements of the model: depth and areal extent of permafrost, the soil carbon pool, the vegetation, and the production of methane. These effects are analyzed at two spatial scales: at the local scale of the land cells defined by the spatial discretization of the numerical model, and at the regional scale of the Northern Hemisphere permafrost region.

Finally, the third chapter of this thesis corresponds to one article we developed to make use of a thermal profile measured from the ice core at the EPICA Dome C site in East Antarctica in 2004 (Augustin et al., 2004). In this chapter, we developed a numerical method to introduce constraints on several key parameters of glacier flow, using the present thermal profile of the glacier and geodetic data. This article was submitted to the scientific journal *Climate of the Past*, but was withdrawn due to a request by Catherine Ritz (personal communication, Decem-

ber 12, 2016), who collected and provided us the data used in the article. An unfortunate miscommunication caused us to believe that we had permission to use this data, which was not the case. Catherine Ritz agreed to the inclusion of this paper in this thesis.

The analysis of ice cores provide reliable records of past climate, going back hundreds of thousands of years into the past (Parrenin et al., 2007a; Jouzel et al., 2007). The analysis of the air bubbles trapped in the ice allows the reconstruction of the past concentrations of atmospheric gases such as  $\text{CO}_2$ ,  $\text{CH}_4$  and  $\text{N}_2\text{O}$  (Barnola et al., 1987; Spahni et al., 2005). The ice cores also allow to reconstruct the history of past atmospheric temperatures and past accumulation rates, from the analysis of stable oxygen isotope ratios and deuterium in the ice core (Jouzel et al., 2007; Pol et al., 2010). The ice core at Dome C, drilled by the European Project for Ice Coring in Antarctica (EPICA), provides these records for the past 800 kyr, which makes it one of the longest records currently available (Augustin et al., 2004).

In addition to past atmospheric composition, atmospheric temperature and snow accumulation, the measurement of the ice temperature in the ice core provides a high resolution temperature-depth profile of the ice sheet. These thermal profiles are used to calculate the conductive heat flux, which allows the estimate the crustal heat flux at the measurement site (Fisher et al., 2015). However, this estimate is a first order approximation, because there are more factors affecting the thermal profile other than the crustal heat flux. First, the thermal profile is affected by the past history of atmospheric temperatures at the top of the glacier, as this thermal signal propagate downwards. Second, the deformation of the ice produces internal heating, rising temperature inside the glacier. To determine the real value of the crustal heat flux, these factors have to be taken into account.

In land, the relationship between the history of past ground surface temperatures and the present temperature-depth profiles is the base of borehole paleoclimatology (Mareschal & Beltrami, 1992). Because the thermal regime of the continental deep subsurface is purely conductive, inverse methods can be applied to reconstruct past ground surface temperatures from the temperature-depth profile (Jaupart & Mareschal, 2010). However, these analytical methods can not be applied to isolate the contributions of the surface temperature history and the crustal heat flux in glaciers, because the thermal regime of the glacier is not conductive due to the flow of the ice. Instead, we used a numerical model to simulate the flow of ice and the thermal dynamics of the glacier at Dome C.

We developed a one-dimensional numerical model to simulate the glacier at Dome C, which includes the flow of ice and the generation and conduction of heat. This model simulates the past 800 kyr using as boundary conditions the reconstructed histories of past atmospheric surface temperatures, snow accumulation and glacier height at Dome C, obtained from the analysis of Deuterium content in the ice core and from a 1-D ice flow model at Dome C (Jouzel, 2007; Parrenin et al., 2007b).

In Dome C, in addition the crustal heat flux, we find several parameters of ice flow that are undetermined. We use a Monte-Carlo method to determine the unknown parameters at Dome C, by randomly sampling their values. The numerical model yields a thermal profile at present, which is determined by the values of these parameters. By comparing the calculated thermal profile to that measured at Dome C, we obtain a 'goodness of fit' measurement (how close the profiles are) for a specific location in the parameter space. In this way, we are able to determine a probability distribution for the unknown parameters, their most likely values and the range of acceptable values.

The three scientific articles that form the body of this thesis are all original studies.

My contribution to these articles constitutes the principal part of each article. In the first and second chapters, I modified the CLM4.5, tested and performed simulations, and analyzed and interpreted the results. In the third chapter, I developed and tested the numerical model and analyzed the results. My thesis director, Dr. Hugo Beltrami, and my thesis codirector, Dr. Jean-Claude Mareschal, developed the theoretical framework for the first and second chapters, provided the ideas for the third chapter, and helped with the editing of the three manuscripts. Dr. Mareschal also participated in the development of the theoretical development needed for the third chapter. The first and second articles are cosigned by Dr. Andrew H. MacDougall, who provided his expertise for the analysis of the results, and made many useful comments while writing the papers.

## CHAPTER I

### LOWER BOUNDARY CONDITIONS IN LAND SURFACE MODELS. PART 1: HEAT STORAGE AND TEMPERATURE-DEPTH PROFILES.

#### 1.1 Abstract

Earth System Models (ESMs) use bottom boundaries for their land surface model components which are shallower than the depth reached by surface temperature changes in the centennial time scale associated with recent climate change. Shallow bottom boundaries reflect energy to the surface, which along with the lack of geothermal heat flux in current land surface models, alter the surface energy balance and therefore affect some feedback processes between the ground surface and the atmosphere, such as permafrost and soil carbon stability. To estimate these impacts, we modified the subsurface model in the Community Land Model version 4.5 (CLM4.5) by setting a non-zero crustal heat flux bottom boundary condition and by increasing the depth of the lower boundary from 42.1 m to 342.1 m. The modified and original land models were run during the period 1901-2005 under the historical forcing and between 2005-2300 under two future scenarios of moderate (RCP 4.5) and high (RCP 8.5) emissions. Increasing the thickness of the subsurface by 300 m increases the heat stored in the subsurface by 72 ZJ (1 ZJ =  $10^{21}$  J) by year 2300 for the RCP 4.5 scenario and 201 ZJ for the RCP 8.5 scenario (respective increases of 260% and 217% relative to the shallow model), while the heat absorbed by the upper soil layer (3.8 m thick) decreases. Using

the mean continental heat flux  $0.06 \text{ W m}^{-2}$  at the bottom of the model rises the temperature at 3.8 m (the soil-bedrock interface) by  $0.12 \pm 0.03 \text{ K}$  and the bottom bedrock layer by  $0.8 \pm 0.04 \text{ K}$ , independently of the scenario. We determine the optimal subsurface thickness to be 100 m for a 100 yr simulation and 200 m for a simulation of 400 yr.

## 1.2 Introduction

In the current context of anthropogenic climate change, there is a need to forecast future impacts of climate change as accurately and reliably as possible. Future climate change projections are based on simulations from ensembles of Earth System Models (ESMs), numerical models of oceans, atmosphere, land, ice, and biosphere subsystems coupled together (Stocker et al., 2013). Modeling of the land system has mainly focused on the interactions between the land surface and the atmosphere (Pitman, 2003), including biogeochemical cycles taking place in the shallow subsurface or soil, such as carbon dynamics (Ramanathan & Carmichael, 2008), soil moisture (Seneviratne et al., 2010), vegetation cover and land use (Bonan, 2008), and surface processes such as albedo and snow cover (Hansen & Nazarenko, 2004). The bedrock layer present below soil is impermeable, and when explicitly modeled, the only process taking place in bedrock is thermal diffusion.

Thermal diffusion in the subsurface allows the land system to act like a heat reservoir, contributing to the thermal inertia of Earth's climate. However, this contribution is relatively small as the capacity of the oceans to absorb energy is orders of magnitude above that of the continents (Stocker et al., 2013). Estimates of the energy accumulation during the second half of the 20th century in the land system show that the heat stored in continents ( $9 \pm 1 \text{ ZJ}$ , where  $1 \text{ ZJ} = (10^{21} \text{ J})$ ) is less than the uncertainty on the heat stored in oceans during the same period ( $240 \pm 19 \text{ ZJ}$  (Beltrami et al., 2002; Levitus et al., 2012; Rhein et al., 2013)).

This allows many ESMs to only consider the land subsurface to the shallow depth (3 – 4 m) needed for soil modeling (Schmidt et al., 2014; Wu et al., 2014) and neglect the bedrock entirely. Still, the thermal regime of the subsurface affects the energy balance at the surface, which in turn influences the surface and soil processes with a feedback on the climate system. Energy variations at the land surface propagate underground, and the use of a too shallow subsurface in land models implies that these signals are reflected towards the surface, altering its energy balance (Smerdon & Stieglitz, 2006; Stevens et al., 2007).

Several works (MacDougall et al., 2008, 2010) have pointed out that, for the long time scales of climate change, the temperature variations at the land surface propagate much deeper than the depths considered in current land models, which range between  $\sim 3.5$  m (Schmidt et al., 2014; Wu et al., 2014) and 42 m (Oleson et al., 2013). Theoretical estimates (MacDougall et al., 2008) of heat stored by the subsurface show a difference of one order of magnitude between models using subsurface thicknesses of 10 m and 600 m. This suggests that the reflected energy in shallow land models affects the surface energy balance in the simulations, and current ESMs should use land models sufficiently deep for the length of the simulations, to avoid bottom boundary effects on the thermal profiles.

Most of the current land models use a zero heat flux as thermal boundary condition at their base, as the geothermal gradient is small ( $\sim 0.02$  K/m) and does not affect temperature much at shallow depth (Jaupart & Mareschal, 2010). Subsurface models that increase the depth of the bottom boundary to hundreds of meters have to consider the geothermal gradient to properly represent the thermal regime of the subsurface. This can be easily implemented by using the Earth's crustal heat flux as bottom boundary condition of the land model, as a few models already do (Avis et al., 2011).

Soils in permafrost regions act as a long-term carbon sink that stores an estimate of 1100-1500 GtC of organic carbon, twice the carbon content of the pre-industrial atmosphere (MacDougall & Beltrami, 2017; Hugelius et al., 2014). The feedback between climate and permafrost thawing and associated carbon emissions is expected to accelerate global warming (Schuur et al., 2015). Rising temperatures at high latitudes induce the thawing of permafrost, leading to the decay of frozen organic matter and the release of CO<sub>2</sub> and CH<sub>4</sub> into the atmosphere. We expect that, both the thickness of the subsurface and setting a realistic non-zero value of heat flux as bottom boundary condition will affect the evolution of permafrost in a warming scenario, and therefore the release of permafrost carbon.

It is possible to use analytical methods to estimate the effect that the depth of the bottom boundary and the use of a non zero basal heat flux as bottom boundary condition have on the thermal profile of the ground (Stevens et al., 2007). Because of the complexity of the biogeochemical processes in the soil, only numerical simulations can estimate how these processes are affected by the changes in the thermal profiles. In this paper, we study the effect of the increase of the lower boundary depth and the addition of a geothermal heat flux at the base of the Community Land Model version 4.5 (CLM4.5) (Oleson et al., 2013), which is the deepest (42.1 m) of the current land models used in the Climate Model Intercomparison Project phase 5 (CMIP5) (Stocker et al., 2013). We carried out simulations between 1901 CE and 2300 CE, using historical climate reconstruction between 1901 and 2005 (Viovy, 2018) and explored two alternative scenarios of moderate and high radiative forcings between 2006 and 2300 (Thomson et al., 2011; Riahi et al., 2011).

### 1.3 Theoretical analysis

The Earth's continental lithosphere ( $> 100$  km) can be considered as a semi-infinite solid for the centennial and millennial time scales considered in the future projection of climate. For a purely-conductive thermal regime of the subsurface, the propagation of a temperature signal at the surface into the ground is governed by the heat diffusion equation in one dimension (Carslaw & Jaeger, 1959):

$$\frac{\partial T}{\partial t} = \kappa \frac{\partial^2 T}{\partial z^2}, \quad (1.1)$$

where  $\kappa$  is thermal diffusivity. The solution of Eq. (1.1) for a step change  $T_0$  in surface temperature at  $t = 0$  yields the temperature anomaly at depth  $z$  and at time  $t$ :

$$T(z, t) = T_0 \operatorname{erfc} \left( \frac{z}{2\sqrt{\kappa t}} \right). \quad (1.2)$$

The general solution for any surface temperature perturbation  $T_0(t)$  starting at  $t = 0$  can be obtained as the convolution in time of  $T_0(t)$  and the Green function associated to Eq. (1.1) and the boundary conditions. As the Green function is the solution to a Dirac's delta, it is obtained as the general solution is the time derivative of the solution to the step function in Eq. (1.2). Therefore, the general solution is:

$$T(z, t) = \frac{z}{2\sqrt{\pi\kappa}} \int_0^t T_0(\xi) (t - \xi)^{-3/2} \exp \left( -\frac{z^2}{4\kappa(t - \xi)} \right) d\xi. \quad (1.3)$$

Future scenarios (Van Vuuren et al., 2011) predict rising atmospheric temperatures during the present century (Cubasch et al., 2013) with a wide margin of variability and uncertainty. We can represent this future rise of temperatures by a linearly increasing surface temperature  $T_0(t) = mt$ , with  $m$  being the rate of temperature increase. For such surface temperature function, the solution to Eq. (1.1) is:

$$T(z, t) = mt \left[ \left( 1 + \frac{z^2}{2\kappa t} \right) \operatorname{erfc} \left( \frac{z}{2\sqrt{\kappa t}} \right) - \frac{z}{\sqrt{\pi\kappa t}} \exp \left( \frac{-z^2}{4\kappa t} \right) \right]. \quad (1.4)$$

Numerical models, however, cannot simulate the subsurface as a semi-infinite solid, also known as half space model, but instead limit the subsurface to a given depth, that varies between models. Many land models include only the upper 3 – 4 m of the subsurface, which they consider as soil, to model the most basic hydrological processes such as infiltration and runoff in a first-order approximation. Other models further extend the subsurface to include the bedrock below, the deepest currently being the CLM4.5 with a total depth of 42.1 m. We can simplify these models by considering conduction only and modeling the land subsurface as a solid bounded by two parallel planes. Assuming a lower boundary condition of no heat flux (as most current models do) and a temperature increasing linearly with time  $T_0(t) = mt$  as surface boundary condition, we obtain the following solution to Equation (1.1) (Carslaw & Jaeger, 1959):

$$\begin{aligned}
T(z, t) = m \sum_{n=0}^{\infty} (-1)^n \left\{ \left( t + \frac{(2nd + z)^2}{2\kappa} \right) \operatorname{erfc} \left( \frac{2nd + z}{2\sqrt{\kappa t}} \right) - \right. \\
- (2nd + z) \left( \frac{t}{\pi\kappa} \right)^2 \exp \left( -\frac{(2nd + z)^2}{4\kappa t} \right) + \\
+ \left( t + \frac{(2(n+1)d - z)^2}{2\kappa} \right) \operatorname{erfc} \left( \frac{(2(n+1)d - z)}{2\sqrt{\kappa t}} \right) - \\
\left. - (2(n+1)d - z) \left( \frac{t}{\pi\kappa} \right)^2 \exp \left( -\frac{(2(n+1)d - z)^2}{4\kappa t} \right) \right\}, \quad (1.5)
\end{aligned}$$

where  $d$  is the depth of the bottom boundary. Neglecting near-surface processes such as hydrology or snow isolation, the temperature of the subsurface is described by Eq. (1.5).

Using Eqs. (1.4) and (1.5), we can estimate the effect of the thickness of the model. We have calculated the profiles of temperature perturbation for a rate of surface temperature increase of  $0.01 \text{ K yr}^{-1}$ , assuming a thermal diffusivity of  $\kappa = 1.5 \times 10^{-6} \text{ m}^2 \text{ s}^{-1}$  (used for bedrock in the CLM4.5 (Oleson et al., 2013)). This temperature increase is within the range of global temperature projections for the 21st century (Collins et al., 2013).

We calculated the temperature anomalies for the half space model and the layers of thickness 42.1 m and 342.1 m, after 100 yr and 400 yr. After 100 yr the temperature anomaly for the thinnest (42.1m) model has departed from that of the half space model (Fig. 1.01a), while the thickest (342.1 m) model cannot be distinguished from the half space solution after 100 yr. After 400 yr the thickest model only has small departure near the base (Fig. 1.01b). The response of a model of finite thickness approaches that of the half space model, as long as the bottom boundary is deep enough for the difference between Eqs. (1.4) and (1.5) to be negligible.

The maximum time before the shallow bottom boundary affects the thermal behavior of the model is better appreciated in terms of heat absorption by the subsurface. The heat stored in the subsurface can be calculated from the temperature change in Eq. (1.5) by assuming a uniform volumetric heat capacity  $c = 2 \times 10^6 \text{ J m}^{-3} \text{ K}^{-1}$  (value used for bedrock in the CLM4.5).

The heat absorbed per unit of area for the 42.1 m model is slightly smaller than that of the half space model after 100 yr and less than half after 400 yr, while for the 342.1 m model no difference can be observed (Fig. 1.02a). The heat absorbed after 100 yr or 400 yr increases with the thickness of the model, but reaches a plateau where further increase in thickness does not affect heat storage (Fig. 1.02b). A bottom boundary depth of 342.1 m is enough for a simulation lasting 400 yr, but a bottom boundary depth of 42.1 m is not adequate for a simulation of 100 yr. A bottom boundary depth  $d = 100 \text{ m}$  is enough for a simulation of 100 yr, as the heat absorbed by the land column does not increase much with further increasing  $d$ . A simulation of 400 yr, 4 times longer, needs a bottom boundary depth of  $d = 200 \text{ m}$ , only twice as much (Fig. 1.02b).

The heat equation (1.1) shows a scaling relationship between bottom boundary

depth  $d$  and time  $t$ ,  $d \propto \sqrt{\kappa t}$ . This relation can be used as a first order estimate of the depth where the lower boundary does not affect the thermal profiles for a given duration of the simulation and a value of diffusivity  $\kappa$ .

### 1.3.1 Geothermal gradient

In the conductive regime described by Eq. (1.1), the subsurface temperature at a depth  $z$  is given as a combination of the geothermal temperature gradient and the temperature perturbation  $T_t$  induced by a time-varying temperature signal at the surface:

$$T(z, t) = T_0 + q_0 \frac{z}{\lambda} + T_t(z, t), \quad (1.6)$$

where  $T_0$  is the the mean surface temperature,  $q_0$  is the geothermal heat flux and  $z/\lambda$  is the thermal depth and  $\lambda$  is the thermal conductivity of the subsurface.

The propagation into the subsurface of an harmonic temperature signal such as the annual air temperature cycle is characterized by exponential amplitude attenuation  $\exp(-\sqrt{\frac{\omega}{2\kappa}}z)$  (Carslaw & Jaeger, 1959), where  $\omega$  is the frequency of the signal and  $\kappa$  is the thermal diffusivity. At depths of 3 – 4 m, the amplitude of the annual signal is several degrees. Given the small values ( $\approx 0.02 \text{ K m}^{-1}$ ) of the geothermal temperature gradient in the continents (Jaupart & Mareschal, 2010), the temperature near the surface is dominated by the surface signal  $T_t$ . Therefore it may seem reasonable to neglect the geothermal gradient for a thin subsurface layer used in land models (Schmidt et al., 2014; Wu et al., 2014). However, the geothermal temperature gradient can still be influential, even at shallow depths, for temperature-sensitive regimes of subsurface such as permafrost, and it is necessary to determine the lower limit of permafrost. In the case of the CLM4.5 with a subsurface thickness of 42.1 m, the temperature at the bottom of the model is increased by  $\approx 0.8 \text{ K}$  by a geothermal gradient of  $0.02 \text{ K m}^{-1}$ . If we were to further increase the thickness of the subsurface, the temperature at the bottom

of the model would increase proportionally.

## 1.4 Methodology

### 1.4.1 Original Land Model

The Community Earth System Model version 1.2 (CESM1.2) is a coupled ESM, consisting of components representing the atmosphere, land, ocean, sea-ice and land-ice. Individual components can be run separately, taking the necessary inputs from prescribed datasets. Because running the coupled model is computationally expensive, we have run only the land model CLM4.5 (Oleson et al., 2013), forced with prescribed atmospheric inputs (Viovy (2018); Thomson et al. (2011); Riahi et al. (2011), see section 1.4.3). These inputs are precipitation, solar radiation, wind speed, surface pressure, surface specific humidity, Surface Air Temperature (SAT) and atmospheric concentrations of aerosols and CO<sub>2</sub>.

Carbon and nitrogen cycles are included in the CLM4.5 through the BioGeoChemistry (BGC) module, which includes a methane module (Riley et al., 2011). CLM4.5-BGC can be run at several spatial resolutions. We have used the intermediate resolution 1.89°lat × 2.5°lon that allows us to compromise between grid fineness and computational requirements. We used the default timestep of 30 minutes (Kluzek, 2013).

The subsurface is discretized in 15 horizontal layers with exponentially increasing node depths:

$$z_i = f_S \{ \exp[0.5(i - 0.5)] - 1 \} , \quad (1.7)$$

where  $f_S = 0.025$  m is the scaling factor. Layer thickness  $\Delta z_i$  is:

$$\Delta z_i = \begin{cases} 0.5(z_1 + z_2) & i = 1 \\ 0.5(z_{i+1} - z_{i-1}) & i = 2 \dots 14 \\ z_{15} - z_{14} & i = 15 \end{cases} \quad (1.8)$$

The total thickness of the model is 42.1 m. The upper 10 layers, to a depth of 3.8 m, are soil layers where biogeochemistry and hydraulic processes take place. The lower 5 layers are the bedrock, where the only process is thermal diffusion. The soil in each land column has a vertically-uniform clay/sand/silt composition and a vertically-variable carbon density (where most of the carbon is concentrated in the upper layers and its concentration decreases with depth), which determines its hydraulic properties and, along with its time-varying water content, its thermal properties. Bedrock layers, assumed to be made of saturated granite (without pores or interstices that could absorb water), are uniform both horizontal and vertically. The thermal properties for bedrock in CLM4.5 are a thermal conductivity  $\lambda = 3 \text{ W m}^{-1} \text{ K}^{-1}$  and a volumetric heat capacity  $c = 2 \times 10^6 \text{ J m}^{-3} \text{ K}^{-1}$ , which give a thermal diffusivity  $\kappa = \lambda/c = 1.5 \times 10^{-6} \text{ m}^2 \text{ s}^{-1}$  (Oleson et al., 2013).

As the horizontal dimensions of the grid are much larger than the thickness of the subsurface, horizontal heat conduction is considered negligible and thermal diffusion is considered only in the vertical direction as described in Eq. (1.1). The land subsurface is thermally forced at the surface by its interaction with the atmosphere through latent and sensible heat fluxes, and short and longwave radiation. At the bottom, the model assumes no heat flux.

The hydrology model in CLM4.5 parameterizes interception, throughfall, canopy drip, snow accumulation and melt, water transfer between snow layers, infiltration, evaporation, surface runoff, subsurface drainage, redistribution within the soil column, and groundwater discharge and recharge. The vertical movement of water

in the soil is determined by hydrological properties of the soil layers, which can be altered by their ice content as this reduces the effective porosity of the soil. The model also implements an artificial aquifer with a capacity of 5000 mm at the bottom of the soil column, from where discharge is calculated.

The parametrization of snow in CLM4.5 is based on Anderson (1976), Jordan (1991a) and Yongjiu & Qingcun (1997). The snow consists of up to 5 layers, whose number and thickness increase with the thickness of the snowpile. Thermal conduction in these layers works like in soil layers, with the thermal properties of ice and water. The model includes fractional snow cover following the method of Swenson et al. (2012), and phase transitions between the ice and water in the soil and snow layers.

#### 1.4.2 Modifications of the original model

We made two main modifications to the land model. First, we increased the thickness of the bedrock and the depth of the lower boundary. Second, we assumed uniform and constant heat flux as bottom boundary condition. Increasing the thickness of the land model is necessary to reduce the effect of the lower boundary on the temperature profile. The non-zero heat flux adds the geothermal gradient to the temperature profiles of the subsurface, which allows to determine the lower limit of permafrost in the land column.

We increased the thickness  $d$  of the subsurface by progressively adding new layers of constant thickness at the bottom of the land column, to obtain a set of model versions with increasing values of  $d$ . The thickness of the added layers must be small to fine tune the depth of the bottom boundary. However, the size of the set is limited by our computational resources, as we aim to increase the depth of the bottom boundary by several hundred meters. As a compromise, we used 12.5 m as the thickness of these new layers. The lowest value of  $d$  is 42.1 m (no additional

layers, corresponding to the original model) and its highest value is 342.1 m (24 additional layers, with a total thickness of 300 m).

The bottom boundary condition of the land model is changed to a worldwide uniform value of heat flux. While the continental heat flux is spatially variable, we lack heat flux measurements in wide areas of the world such as South America, Asia and Africa and the Northern Hemisphere permafrost region where heat flux is most important. We use several values of heat flux 0, 0.02, 0.04, 0.06 and 0.08 W m<sup>-2</sup> to cover the range of heat flow values observed in stable continents (Jaupart & Mareschal, 2010).

### 1.4.3 Simulations

We follow the standard spinup procedure (Kluzek, 2013), where the model is initialized with arbitrary pre-initial conditions (no vegetation and uniform subsurface temperature) and driven by a spinup simulation to a steady state (vegetated world adapted to the atmospheric forcings), which can be used as initial condition for the simulation. The spinup period required for the initialization of the model depends on the carbon component used by the land model. In the case of the CLM4.5-BGC, the spinup runs 1000 yr with accelerated decomposition rates (which reduces computational costs and performs consistently well (Thornton & Rosenbloom, 2005)) followed by at least 200 yr with normal decomposition rates. During the spinup phase, we use atmospheric forcings (described below) that correspond to those of the initial years of the simulation, 1901 to 1910.

Increasing the depth  $d$  of the bottom boundary introduces an additional difficulty to the spinup of the model. In the standard spinup procedure, every soil layer is initialized with a temperature of 274 K independent of the grid cell location, then adapts to the steady state determined by the local surface boundary conditions during the spinup. For a subsurface thickness of  $d = 42.1$  m, 1200 yr of spinup

are enough for the subsurface to adapt to the steady state. However, the time needed for the subsurface to reach the steady state is proportional to  $d^2$ , and 1200 yr is insufficient for the thickest subsurface models. Lengthening the spinup time for each model of thickness  $d$  would make computational costs prohibitive. To avoid this problem, we only use the standard spinup procedure for the model with the original bottom boundary depth,  $d = 42.1$  m. The initial conditions for the models with  $d > 42.1$  m are obtained by extrapolating downwards the temperature of the 15th layer with the geothermal gradient of the subsurface. This approach is possible because there are no other variables than temperature in bedrock layers, such as in water or carbon content. In addition, as these models depart from a common initial state, we can determine any difference in the final state as due to the parameter  $d$  exclusively, without influence of the initial state.

The models with different basal heat flux  $F_B$  at the original bottom boundary depth, are individually initialized with the standard spinup procedure. It is not possible to use a common initial condition for these models, because the thermal steady state is dependent on  $F_B$ .

Each land model is run offline between 1901 CE and 2300 CE, taking prescribed atmospheric variables from external sources as input to force the model. These simulations include two phases depending on the input used, (1) between 1901-2005, from reanalysis of historical data, and (2) between 2006-2300, from the IPCC climate projection under two warming scenarios (Thomson et al., 2011; Riahi et al., 2011).

The first phase is a historical 20th century simulation between 1901-2005. The forcing data are taken from the CRUNCEP dataset (Viovy, 2018), combination of the Climate Research Unit Time-Series (CRU-TS) monthly climatology (Harris et al., 2014) and the National Centers for Environmental Prediction (NCEP)

reanalysis (Kalnay et al., 1996) between the years 1901 and 2005.

The second phase continues the first phase between 2006-2300, forcing the land model with the atmospheric output from a simulation for a specific trajectory of greenhouse gas concentration. These trajectories, called Representative Concentration Pathways (RCPs), are based on scenarios of future human emissions and provide a basis to the climate research community for modeling experiments in the long and short terms (Van Vuuren et al., 2011).

We use two scenarios, RCP 4.5 and RCP 8.5, which divide our simulations after 2005. RCP 4.5 is an mitigation scenario of anthropogenic emissions where radiative forcing reaches  $4.5 \text{ W m}^{-2}$  in 2100 (Thomson et al., 2011). In comparison, RCP 8.5 is a high emissions scenario of considerable increase of greenhouse gas emissions and concentrations, leading to a radiative forcing of  $8.5 \text{ W m}^{-2}$  at the end of the 21st century (Riahi et al., 2011).

Forcing datasets of monthly averages are provided by the Earth System Grid (Stern, 2013) for both scenarios. To produce 6h-resolution datasets suitable for CLM4.5, we calculated the 6h-anomalies to monthly average for temperature and precipitation in the years 1996-2005 of the CRUNCEP dataset, and added this 10 yr series of anomalies to the monthly datasets cyclically, starting in 2006. The 6h-resolution datasets produced this way were then used to force the land system between 2006-2300 for the two scenarios. The mean SAT over the land area for the duration of our simulation time is shown in Fig. 1.03. The mean SAT in the last decade 2290-2300 is  $\approx 2 \text{ K}$  higher than in the decade 2000-2010 for the RCP 4.5 scenario, while in the RCP 8.5 scenario temperature rises  $\approx 9.5 \text{ K}$  for the same period.

## 1.5 Results

### 1.5.1 Effect of the depth of the bottom boundary

The results summarized in Table 1.1 confirm the theoretical expectations for the absorption of heat by the subsurface discussed in section 1.3. The heat absorbed by the subsurface varies with time between models of different subsurface thickness  $d$  (Fig. 1.04). If the bottom boundary is too shallow, the thermal signal from the surface reaches the bottom boundary and further absorption of heat is hindered. For the original depth of the CLM4.5,  $d = 42.1$  m, after 100 yr its subsurface absorbs considerably less heat than for the deeper models. As we progressively increase the thickness of the subsurface, this effect is reduced and delayed. By the end of the simulation, the thickest model ( $d = 342.1$  m) has absorbed 72 ZJ ( $72 \times 10^{21}$  J) in the RCP 4.5 scenario and 201 ZJ in the RCP 8.5 scenario, which are respectively 260% and 217% of the heat stored by the thinnest model in these scenarios.

At a given time, the heat absorbed by the subsurface increases with the depth of the bottom boundary  $d$  of the model (Fig. 1.05). The amount of heat is not proportional to  $d$  and levels off when  $d$  increases past a specific threshold. This value is the thickness required by the model to keep the heat absorbed close to the maximum absorbed by the half space. If we define this threshold as 95%, this depth would be  $\approx 90$  m if the simulation runs for 100 yr (until 2000 CE). If we look at the heat absorbed after 400 yr, this threshold depth is  $\approx 200$  m in the RCP 4.5 scenario (Fig. 1.05a), and  $\approx 180$  m in the RCP 8.5 scenario (Fig. 1.05b), which confirms the theoretical estimation. This difference shows that the SAT forcing, dependent on the scenario, has only a small influence on the threshold. It is determined by the heat conduction time across a layer of thickness  $d$ , that is the relationship  $d \propto \sqrt{\kappa t}$  deduced from Eq. (1.5) for the perturbation to the

thermal profile.

Deepening the bottom boundary below 42.1 m also affects the storage of heat within the layers above (Fig. 1.06). The thermal signal is reflected by the bottom boundary, further heating the region above, but as we increase  $d$ , this additional heat decreases. For the thickest model ( $d = 342.1$  m), the upper 42.1 m of the subsurface gain 2.5 ZJ less than the thinnest model in the RCP4.5 scenario (Fig. 1.06a) and 10.7 ZJ in the RCP8.5 scenario (Fig. 1.06b), which correspond respectively to a decrease of 9% and of 11.6%.

Most of the subsurface is considered as bedrock, where the only heat transport process is thermal diffusion. The region of most interest is the soil, (upper 3.8m) where biogeochemical processes, sensitive to temperature, take place. The heat absorbed by the soil has been summarized in Table 1.2. The heat absorbed by the soil is overestimated for the shallow bottom boundary variants of the model in the same manner as it was for the upper 42.1 m, but this effect is much smaller (Fig. 1.07).

The quantitative differences in Fig. 1.07 are small and better analyzed as the heat gained by the soil in each model as relative to the heat gained by the thinnest model (42.1 m thick) (Fig. 1.08). Compared to the thinnest model, the heat stored in the deepest models is  $\approx 1\%$  less after 100 years of simulation, and  $\approx 1.33\%$  at the end of the RCP 4.5 scenario (Fig. 1.08a) and  $\approx 1.92\%$  at the end of the RCP 8.5 scenario (Fig. 1.08b). It can be noted that the relative decrease of heat gained by the soil in the deepest models is larger at 2100 CE than at either 2000 CE or 2300 CE. This, as well as for the differences between Figs. 1.08a and 1.08b, is caused by the yearly changes of SAT forcing (Fig. 1.03), which increases at the fastest rate during the 21st century in both RCP scenarios.

### 1.5.2 Effect of the bottom heat flux

In a purely conductive thermal regime of the subsurface, the value of the heat flux used as bottom boundary condition does not affect heat diffusion. This is not the case for the soil, because in CLM4.5 the thermal properties of the soil depend on temperature through the water/ice content. However, because of the shallowness of the soil, the geothermal gradient does not raise soil temperature sufficiently to affect heat propagation. Therefore, while the heat content of the subsurface increases with the lower boundary heat flux, it should not affect its time evolution.

The bottom heat flux increases the heat content, adding  $2.058 \pm 0.006$  ZJ for each  $0.02 \text{ W m}^{-2}$  (Fig. 1.09). This offset is independent of the forcing scenario and constant in time.

If we look at the heat content within soil (upper 3.8 m) we see the same behavior as for the upper 42.1 m but with smaller amplitude (Fig. 1.10). Heat content is offset by  $0.043 \pm 0.004$  ZJ for every  $0.02 \text{ W m}^{-2}$  increase, regardless of the scenario.

This increase of soil heat content due to the bottom heat flux does not translate into a uniform increase of soil temperature across individual cells, because soil composition and thermal properties vary. Each  $0.02 \text{ W m}^{-2}$  increase of bottom heat flux increases the temperature of the deepest soil layer (node at depth 2.86 m) by  $0.04 \pm 0.01$  K. Using the mean continental heat flux value of  $0.06 \text{ W m}^{-2}$  as bottom boundary condition increases the temperature of the bottom soil layer by  $0.12 \pm 0.03$  K and that of the bottom bedrock layer (node depth at 35.1 m) by  $0.8 \pm 0.04$  K.

## 1.6 Discussion and conclusions

Our results show that deepening the bottom boundary by 300 m increases the heat stored in the subsurface by 72 ZJ and 201 ZJ at the end of the simulations at 2300 CE for the scenarios RCP 4.5 and RCP 8.5 respectively, which correspond to 260% and 217% of the heat stored by the original shallow model. Heat absorption within the soil (upper 3.8 m) is reduced by 1-3% depending on the scenario and the length of the simulation. Increasing the bottom heat flux by  $0.02 \text{ W m}^{-2}$  raises the temperature at the bottom of the soil (3.8 m deep) by  $0.04 \pm 0.01 \text{ K}$ , with some differences between cells due to the variable thermal properties of soil. Using the mean continental heat flux value of  $0.06 \text{ W m}^{-2}$  (Jaupart & Mareschal, 2010) increases the bottom soil temperature by  $0.12 \pm 0.03 \text{ K}$ , and the temperature at the base of the model (42.1 m deep) by  $0.8 \pm 0.04$ .

The depth of the bottom boundary has a considerable effect on the heat absorbed by the subsurface. We have shown that, in a simulation spanning 400 years, the land model requires a thickness of at least 200 m to correctly estimate the temperature profile, while for 100 yr of simulation the optimal thickness is 100 m. The thickness  $d$  needed increases with the length  $t$  of the simulation, but this is not prohibitive for simulations running on much longer timescales, because the depth of the bottom boundary follows a square-root relation  $d \propto \sqrt{\kappa t}$ . This result matches the estimation obtained from the theoretical analysis, which indicates that we can confidently use the theoretical approach to estimate the optimal depth, despite the differences between the theoretical approximation and the numerical model, i.e. the thermal properties of the upper 3.8 m and the thermal signal from the surface. Longer simulations such as the 1000 yr long simulations of the last millennium ensemble (Stocker et al., 2013), require subsurface thicknesses of  $\sim 300 - 350 \text{ m}$ . The computational costs associated to each additional layer

are almost negligible when compared to the whole land model, because the only process taking place in bedrock is thermal diffusion. In addition, we could reduce the number of additional layers needed to obtain a deep enough bottom boundary by increasing their thickness.

The value of the basal heat flux used does not affect heat diffusion within the subsurface in a significant way. However, it raises the temperature of the subsurface through the geothermal temperature gradient. This temperature increase is quantitatively small ( $< 1$  K) within the subsurface of CLM4.5, but it should not be neglected as it could be enough to trigger early permafrost thawing near the permafrost frontier.

While soil thickness in CLM4.5 has a uniform value of 3.8 m, in the natural world the soil thickness presents a high degree of variability, with an estimated global mean of  $\approx 13$  m and reaching depths of several hundred meters in some areas (Shangguan et al., 2017). The newer version Community Land Model version 5.0 (CLM5.0) attempts to address this issue and includes a spatially variable soil thickness within a range of 0.4 m to 8.5 m, which is still below the global average (Lawrence et al., 2018). The soil thickness is derived from survey data where typical values of soil thickness are between 7 m and 10 m (Pelletier et al., 2016), although the growing consensus is that regolith thickness varies between 10-40 m (Clair et al., 2015).

The thermal anomalies associated to insufficient depth of the bottom boundary and lack of basal heat flux are considerable throughout the subsurface. However, this alone is of little importance within the global heat budget model, as the heat absorbed by the continents is even less than the uncertainty of heat absorption by the oceans (Rhein et al., 2013). The most important consequences of these anomalies are associated to the soil, specially in how they affect near-surface

permafrost at northern latitudes, which can be expected to thaw considerably due to the increase of atmospheric temperatures during the simulations. If we consider the effect of the bottom boundary depth and the bottom heat flux condition within the soil, the thermal anomalies are much smaller but still significant.

Any land model, before a simulation starts, must be initialized with appropriate initial conditions, i.e. an initial state of the model that resembles the reality at the time. An appropriate initial condition for the temperature of the subsurface is the steady state determined by the surface temperatures at the start of the simulation. This state can be reached during the length of the spinup from arbitrary initial temperatures, if the depth of the bottom boundary is much shallower than the depth determined by the relation  $d \propto \sqrt{\kappa t}$ , being  $t$  the length of the spinup. However, if we increase  $d$  enough to prevent the bottom boundary from affecting the thermal diffusion during the length of the simulation, we may also prevent those arbitrary initial temperatures to reach a steady state during the length of the spinup. This problem can be avoided if the spinup does not depart from arbitrary initial subsurface temperatures, but instead from a temperature profile as close as possible to the steady state. As the steady state is determined by Eq. (1.6), it is possible to obtain an appropriate initial temperature profile by ignoring the time-varying perturbation  $T_t$  in this equation.

We have modified the CLM4.5 to increase the thickness of the subsurface and implement a non-zero value of the bottom heat flux. We have confirmed the theoretical estimation of the subsurface thickness necessary to avoid the reflection of the surface temperature signal for each simulation length, which we estimate to be  $\sim 200$  m for a simulation of 400 yr. As the SAT signals used in the two scenarios RCP 4.5 and RCP 8.5 SAT differs between and with the SAT signal used in the theoretical estimations, we have confirmed that the optimal thickness does not depend on the SAT signal at the surface. The use of a subsurface thickness of

42.1 m in CLM4.5 severely underestimates the heat absorbed by the land system during a 1900-2300 simulation, which using instead a subsurface thickness of 342.1 m (more than optimal depth) absorbs 72 ZJ (260%) more for the RCP4.5 scenario, or 201 ZJ (217%) more for the RCP8.5 scenario.

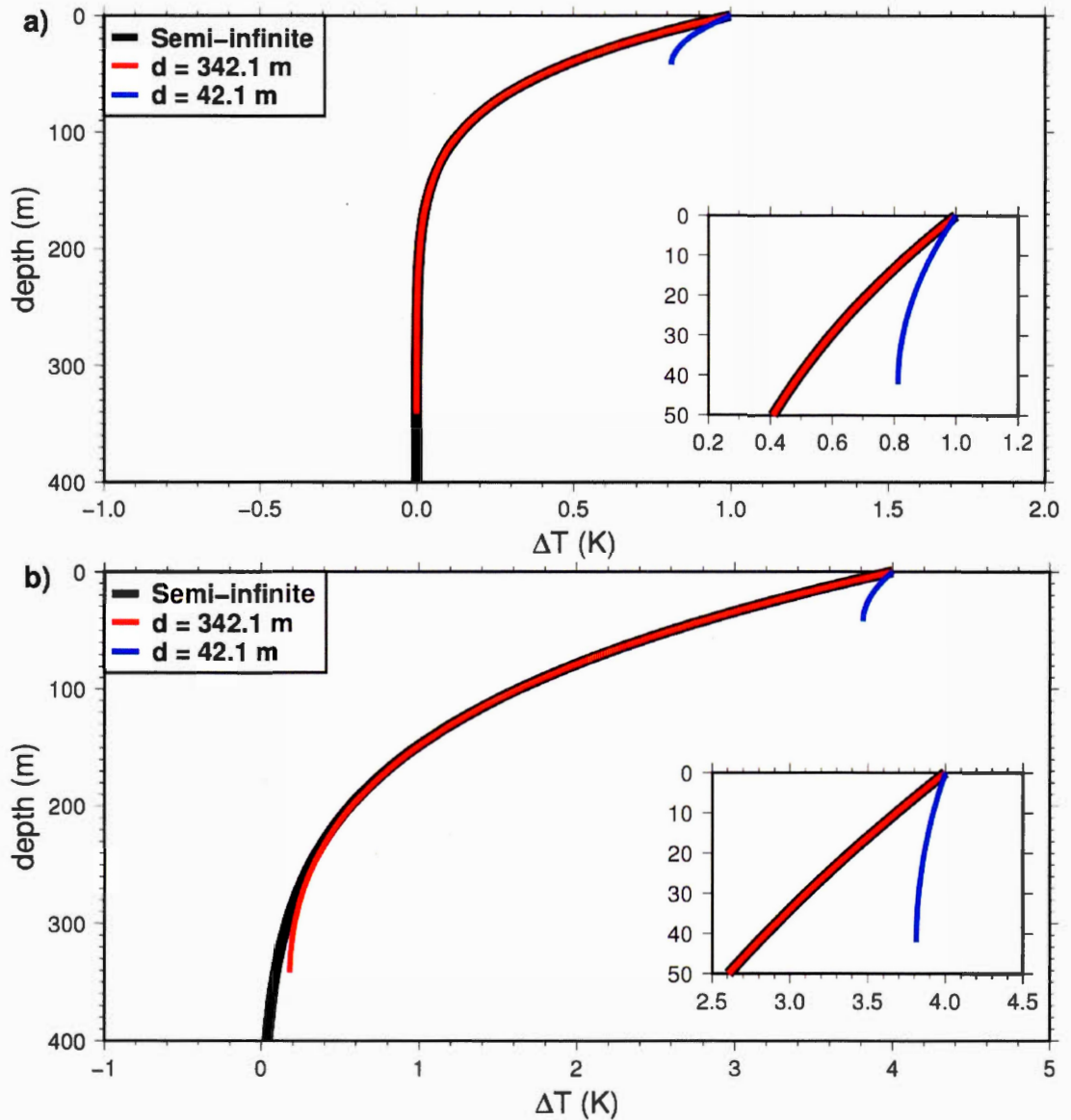


Figure 1.01: Departure from the initial temperature profile due to constant rate of surface temperature increase of  $0.01 \text{ K yr}^{-1}$ . Analytical solutions for the half space model (black), and for the finite thickness model with bottom boundary at 42.1 m (blue) and at 342.1 m (red). a) Temperature anomaly after 100 yr. b) Temperature anomaly after 400 yr.

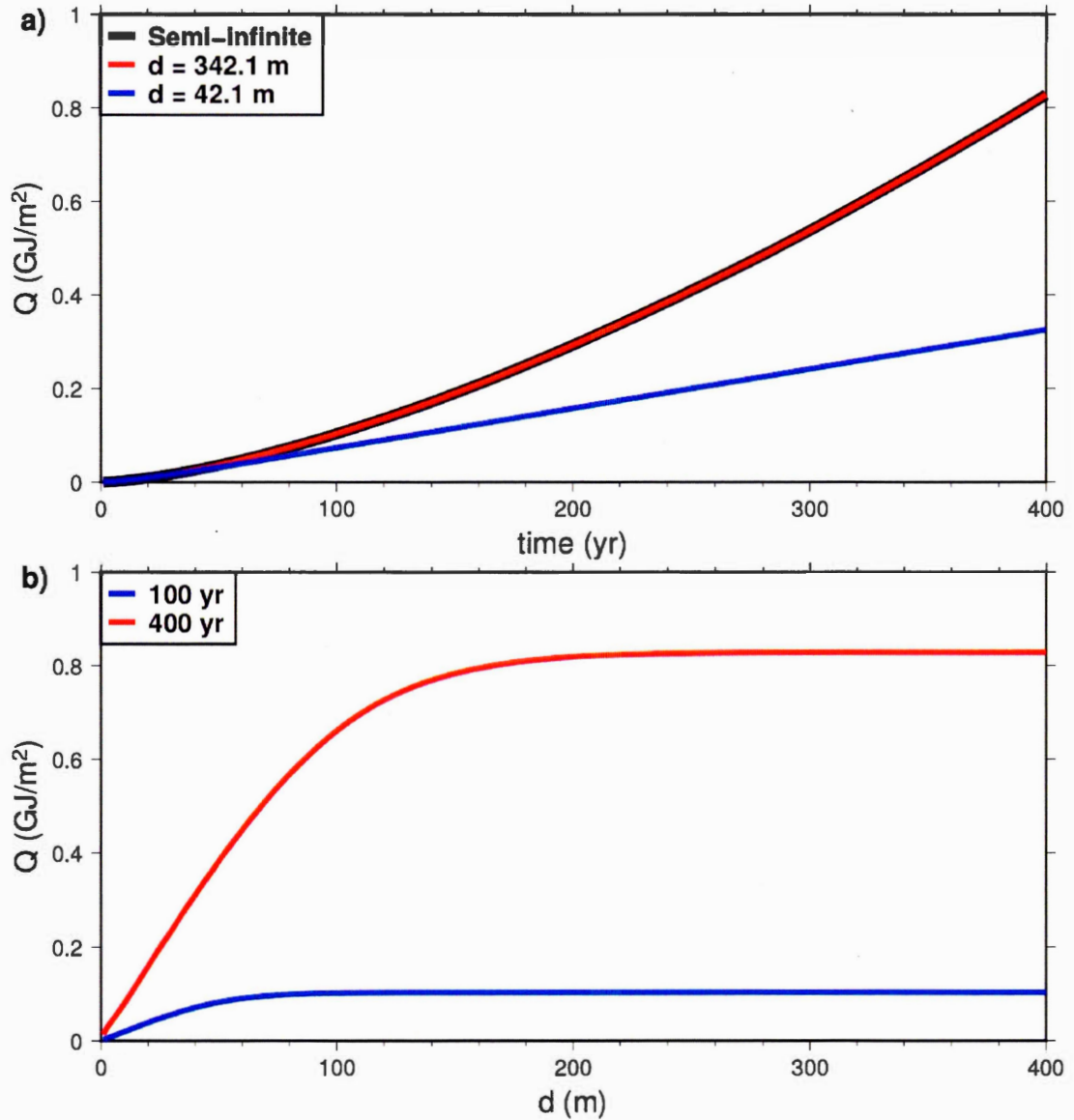


Figure 1.02: Heat absorbed by the land column per unit of area ( $Q$ ), following the start of a linear surface temperature increase of  $0.01 \text{ K yr}^{-1}$ . a):  $Q$  as a function of time for the half space model and two models of finite thicknesses 42.1 m and 342.1 m. b):  $Q$  as a function of the thickness  $d$  of the finite model, at 100 yr and 400 yr.

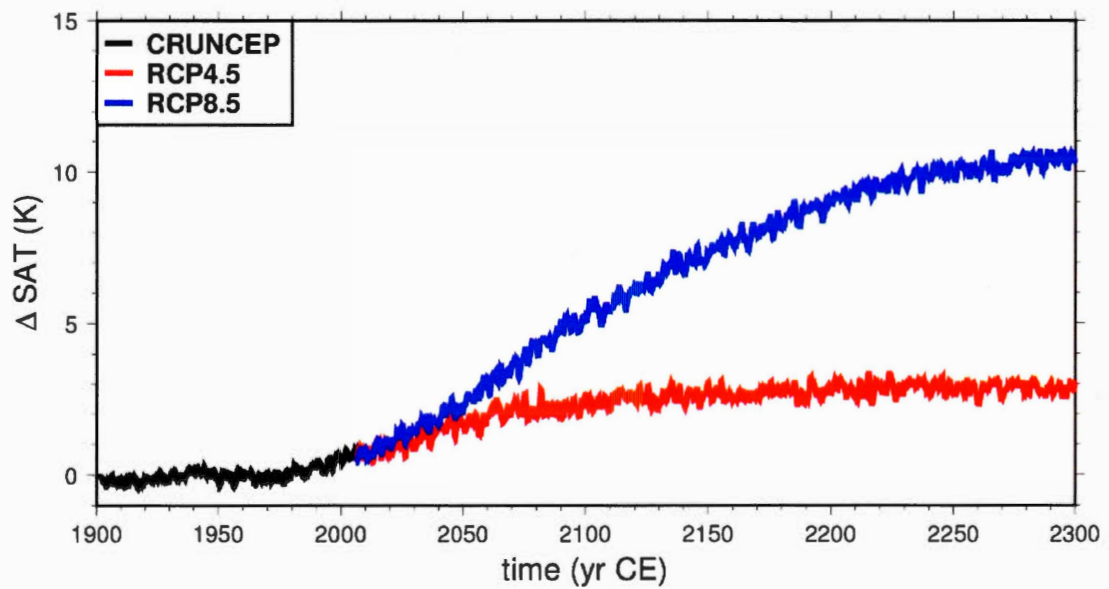


Figure 1.03: Mean Surface Air Temperature (SAT) over land relative to the 20th century mean, from the CRUNCEP dataset (black) and the RCP 4.5 (red) and RCP 8.5 (blue) scenarios. Data taken from Viovy (2018); Thomson et al. (2011); Riahi et al. (2011).

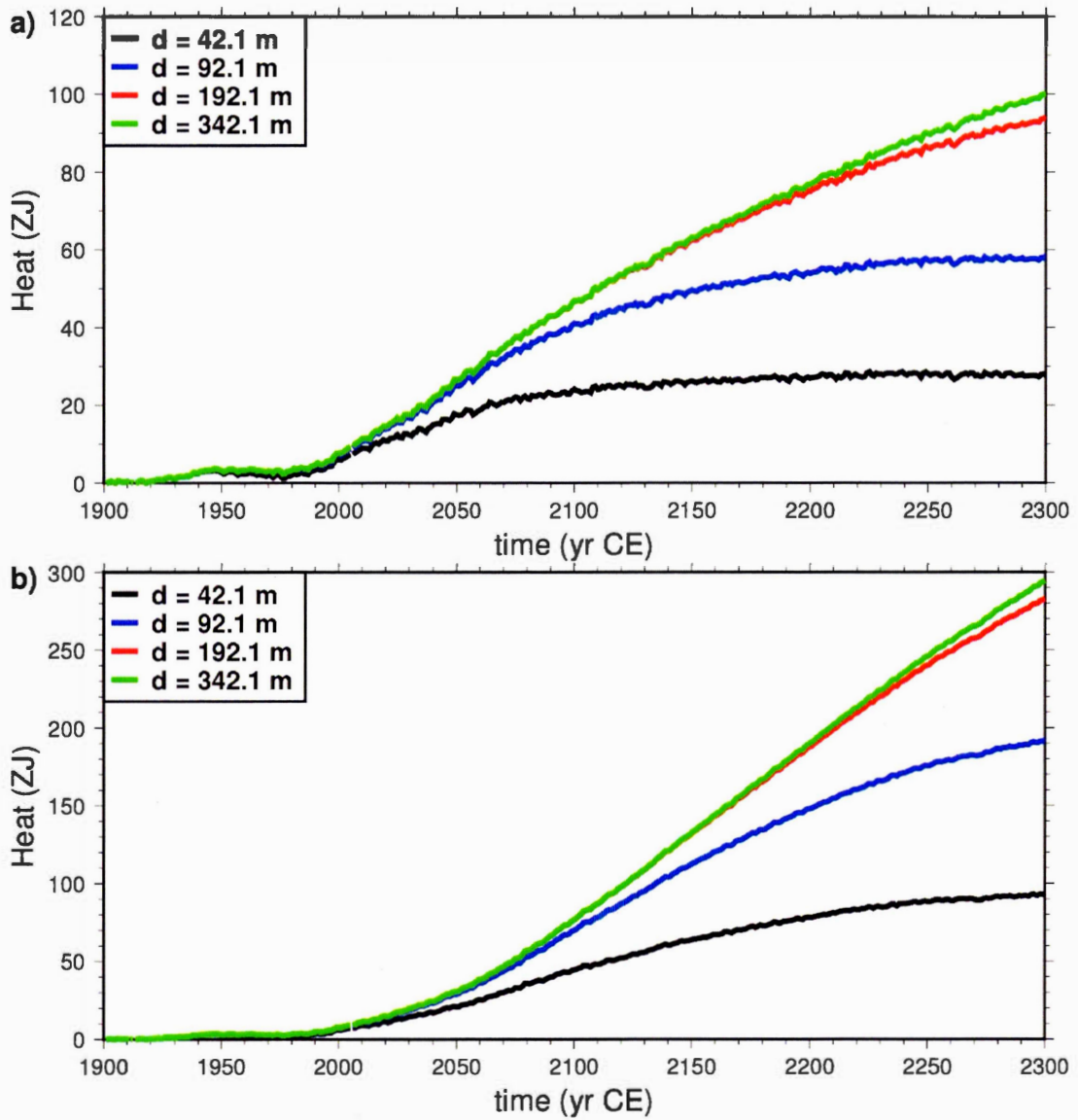


Figure 1.04: Heat stored in the subsurface as function of time, for models of subsurface thickness  $d$  of 42.1 m (black), 92.1 m (blue) 192.1 m (red) and 342.1 m (green). a) Simulations forced with CRUNCEP + RCP 4.5 data. b) Simulations forced with CRUNCEP + RCP 8.5 data. Note the scale difference between scenarios RCP 4.5 and RCP 8.5.

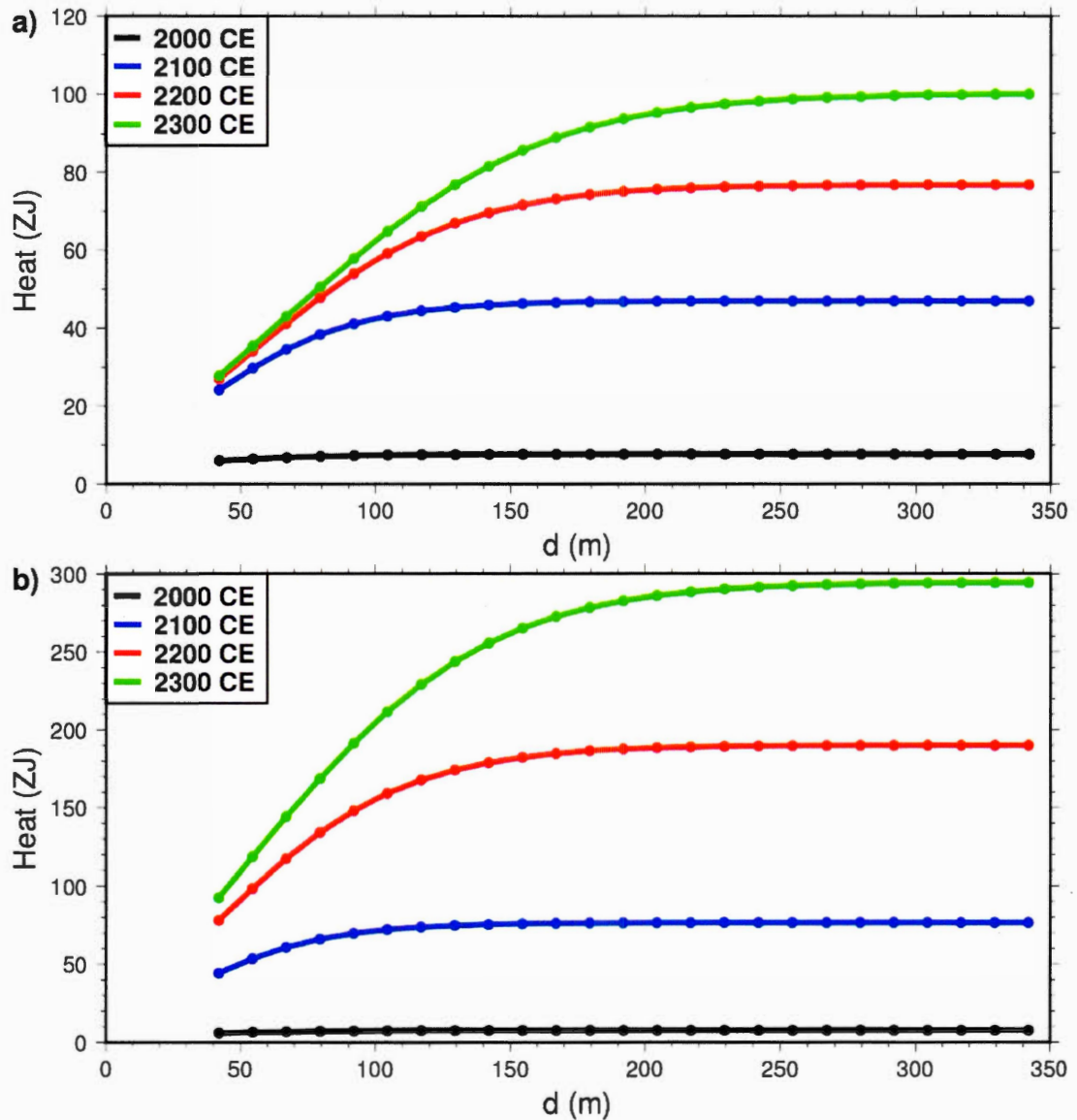


Figure 1.05: Heat stored in the subsurface as function of subsurface thickness, at the years 2000 (black), 2100 (blue), 2200 (red) and 2300 (green). a) Simulations forced with CRUNCEP + RCP 4.5 data. b) Simulations forced with CRUNCEP + RCP 8.5 data. Note the scale difference between scenarios RCP 4.5 and RCP 8.5.

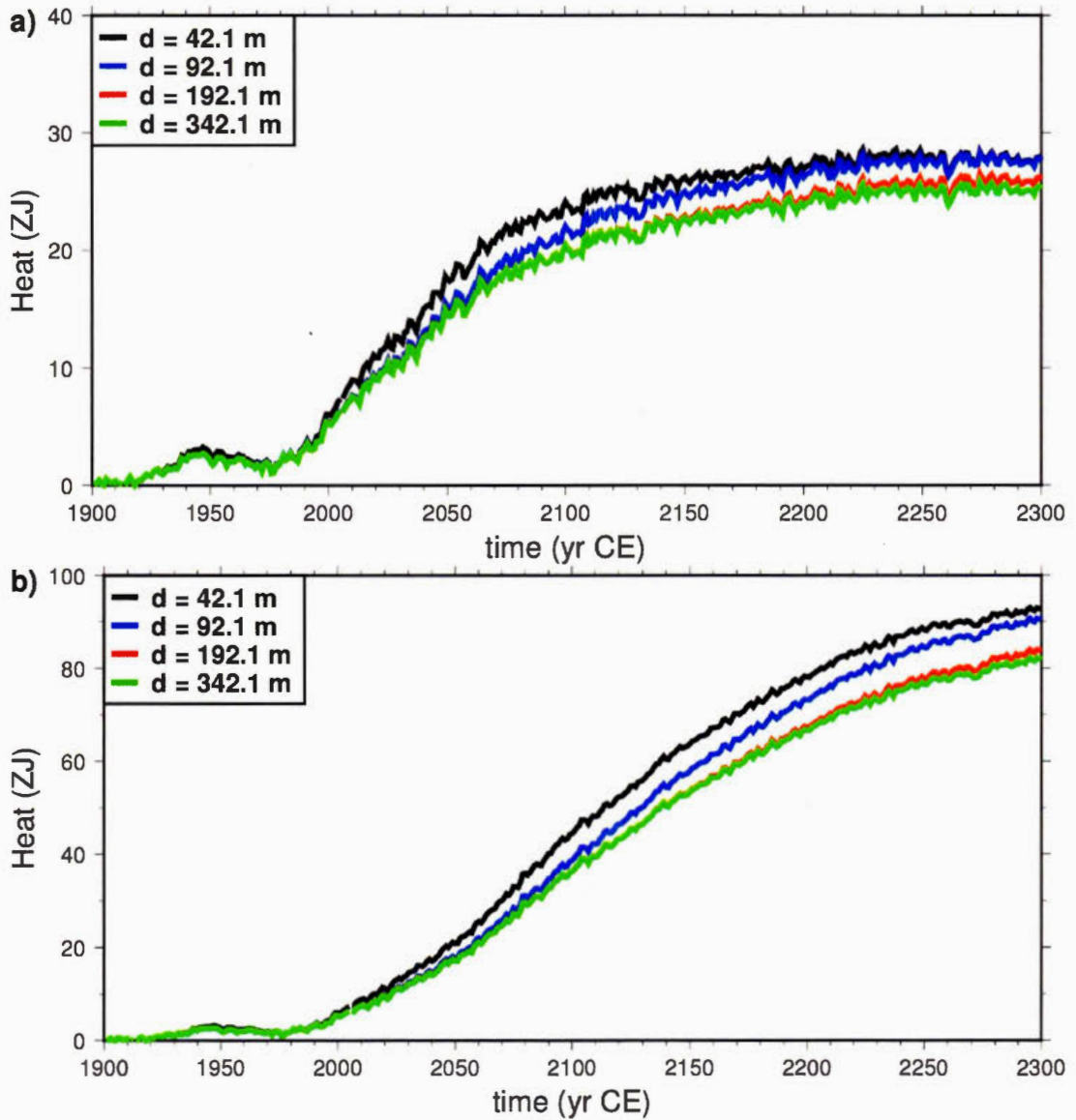


Figure 1.06: Heat stored in the upper 42.1 m as function of time, for models of subsurface thickness  $d$  of 42.1 m (black), 92.1 m (blue) 192.1 m (red) and 342.1 m (green). a) Simulations forced with CRUNCEP + RCP 4.5 data. b) Simulations forced with CRUNCEP + RCP 8.5 data. Note the scale difference between scenarios RCP 4.5 and RCP 8.5.

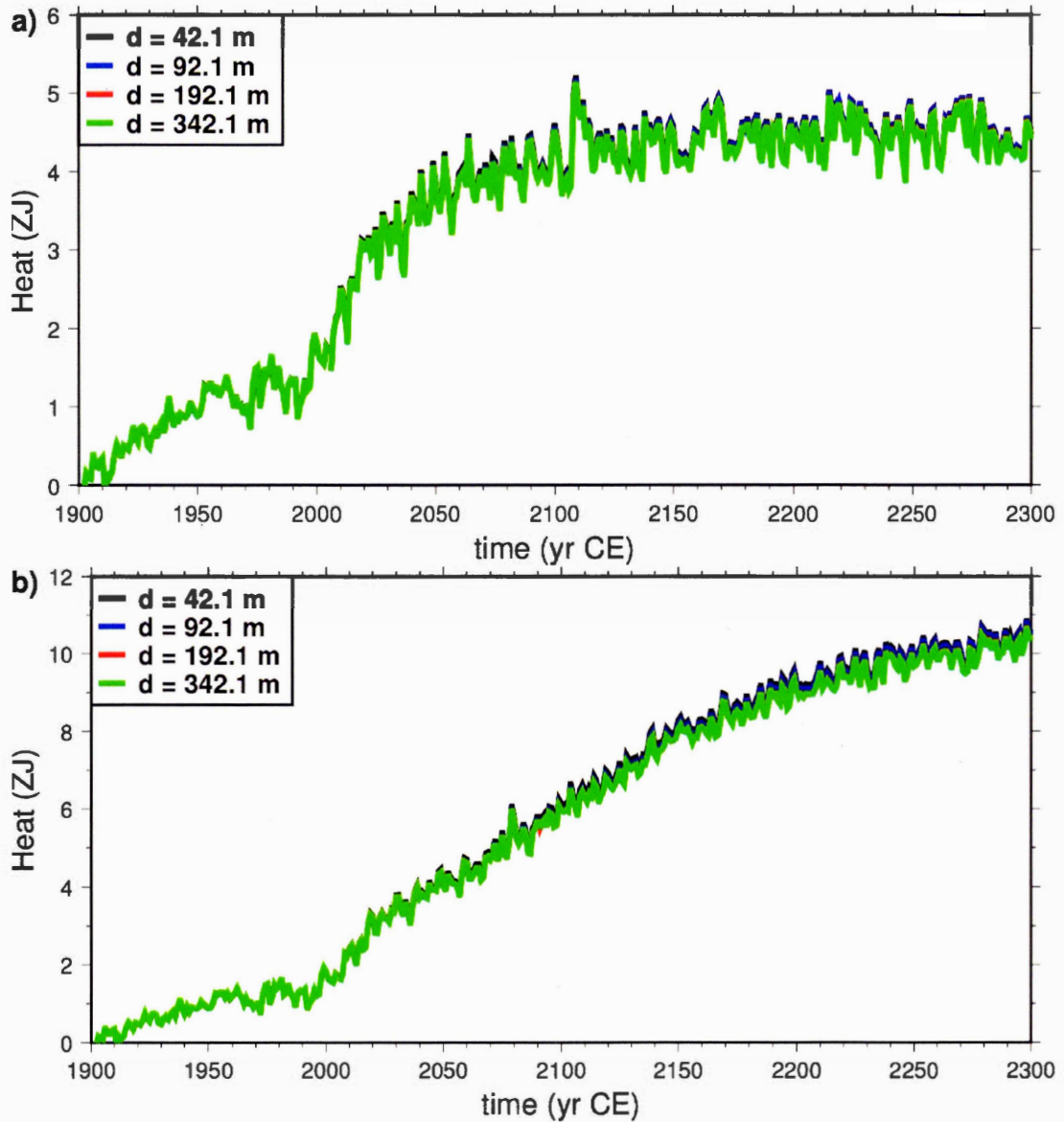


Figure 1.07: Heat stored in the soil (upper 3.8 m), for models of subsurface thickness  $d$  of 42.1 m (black), 92.1 m (blue) 192.1 m (red) and 342.1 m (green). a) Simulations forced with CRUNCEP + RCP 4.5 data. b) Simulations forced with CRUNCEP + RCP 8.5 data. Note the scale difference between scenarios RCP 4.5 and RCP 8.5.

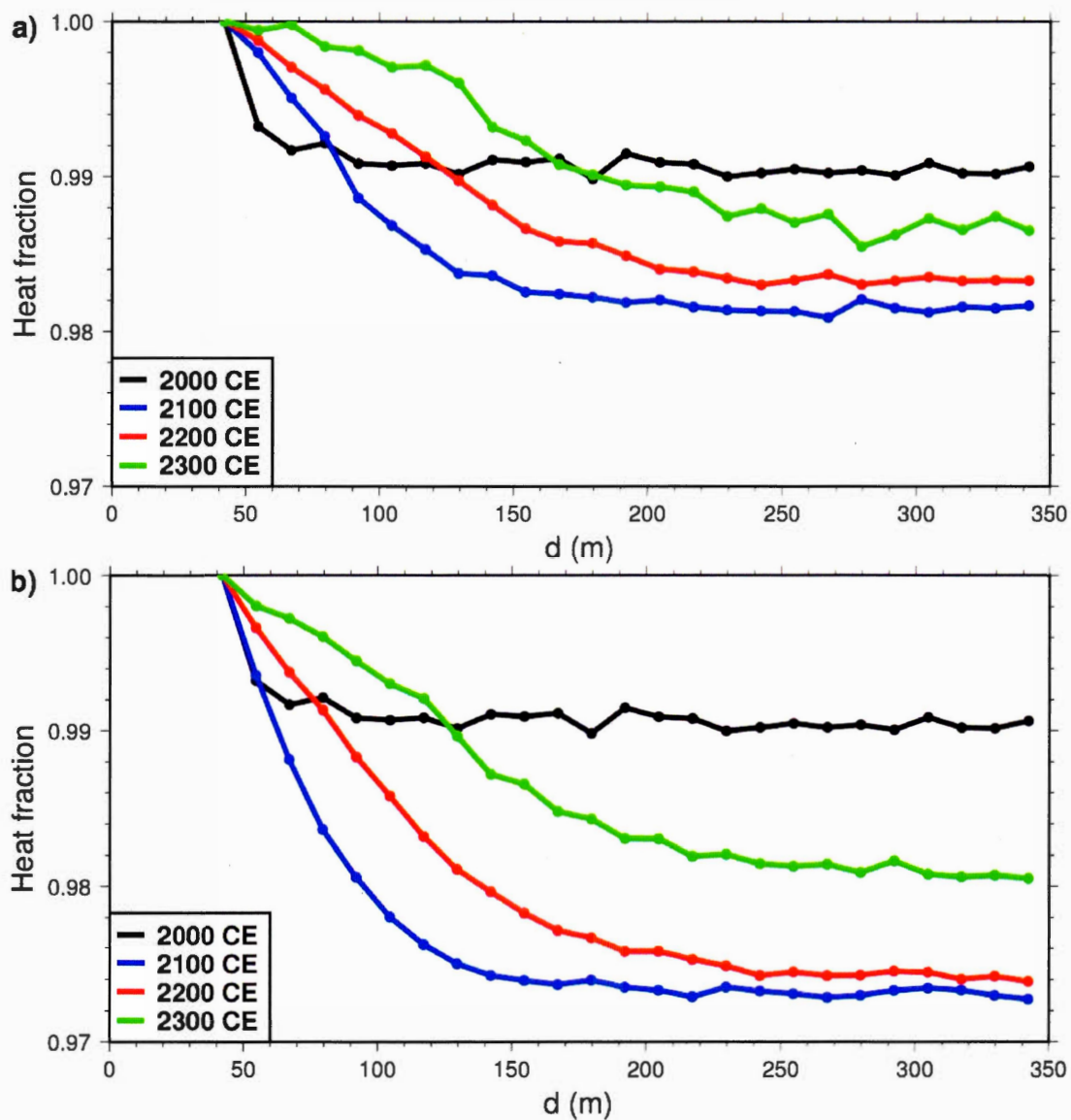


Figure 1.08: Heat stored in the soil as function of subsurface thickness, as fraction of that the thinnest model ( $d=42.1$  m). Years 2000 (black), 2100 (blue), 2200 (red) and 2300 (green). a) Simulations forced with CRUNCEP + RCP 4.5 data. b) Simulations forced with CRUNCEP + RCP 8.5 data.

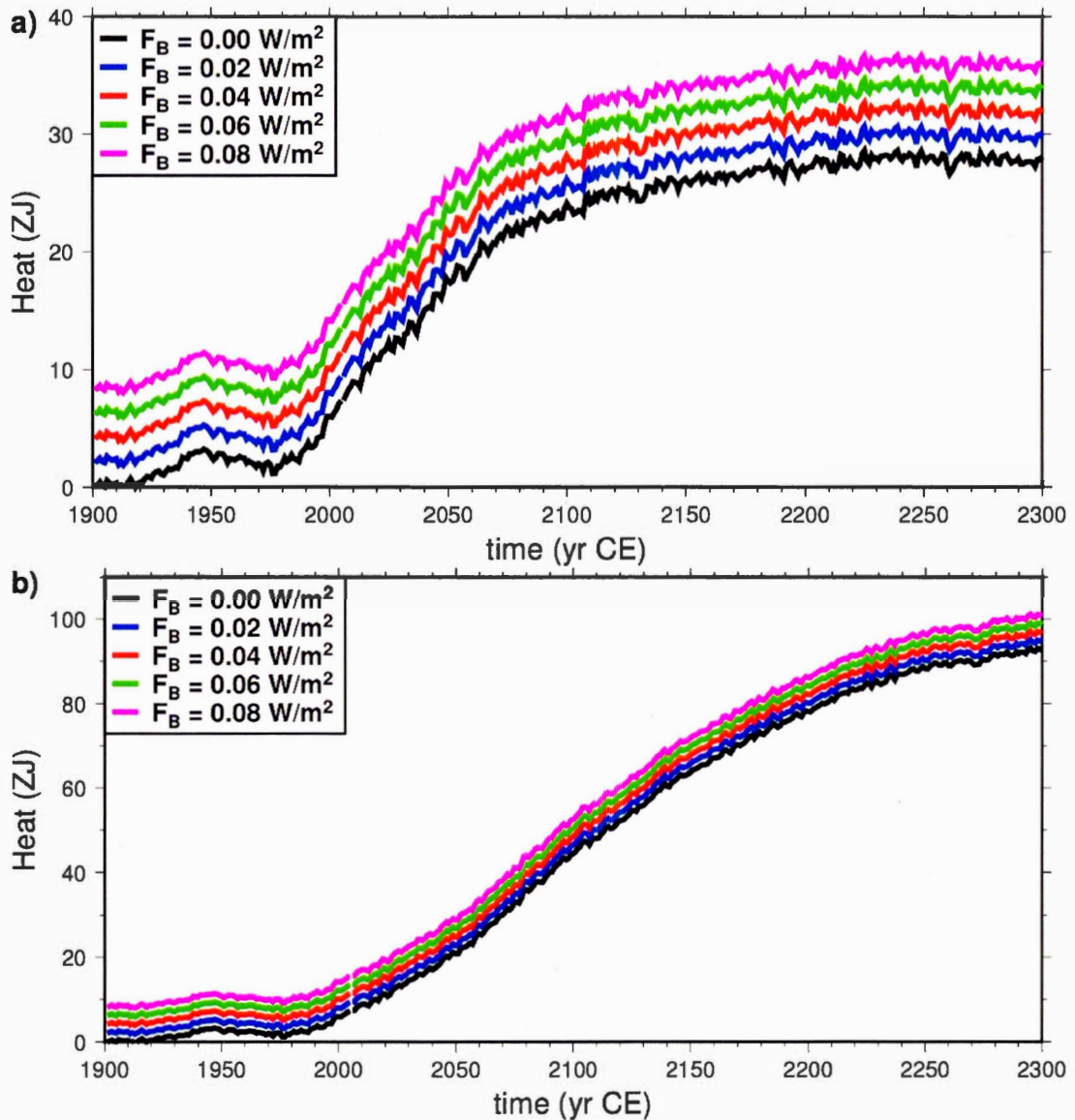


Figure 1.09: Heat stored in the upper 42.1 m (the thickness of all models is 42.1 m) as function of crustal heat flux, relative to the initial heat content of the original model ( $F_B = 0 \text{ W m}^{-2}$ ). The heat content in each model is a static shift from that of the original model. a) Simulations forced with CRUNCEP + RCP 4.5 data. b) Simulations forced with CRUNCEP + RCP 8.5 data. Note the scale difference between scenarios RCP 4.5 and RCP 8.5.

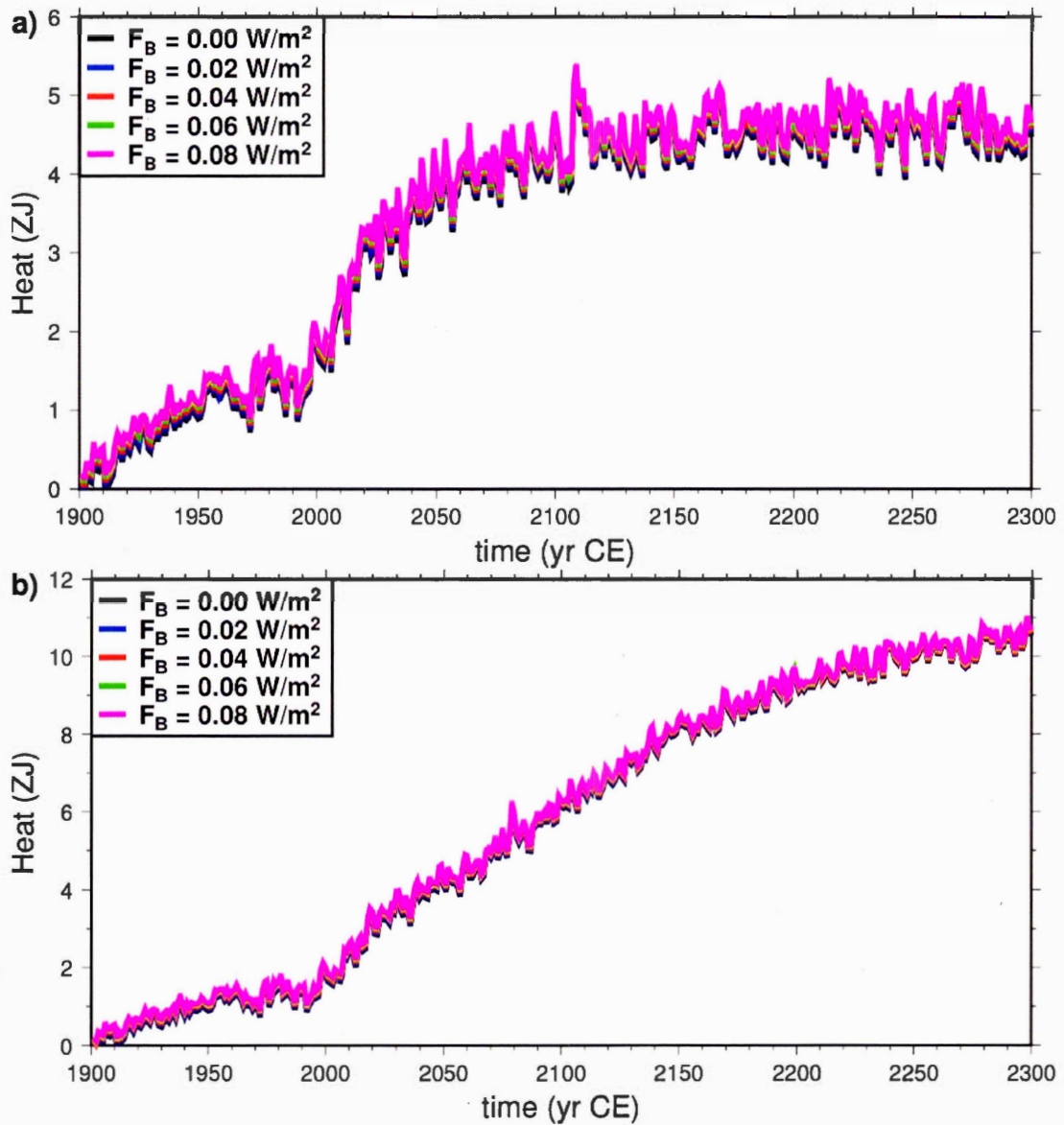


Figure 1.10: Heat stored in the soil (upper 3.8 m) as function of crustal heat flux, referenced to the initial heat content of the original model ( $F_B = 0 \text{ W m}^{-2}$ ). a) Simulations forced with CRUNCEP + RCP 4.5 data. b) Simulations forced with CRUNCEP + RCP 8.5 data. Note the scale difference between scenarios RCP 4.5 and RCP 8.5.

Table 1.1: Heat stored in the subsurface since 1901 CE in the year 2000, and predicted for years 2100, 2200 and 2300 CE for the RCP 4.5 and RCP 8.5 scenarios.

$d$ (m)	RCP 4.5				RCP 8.5			
	$\Delta H$ 1901-2000 (ZJ)	$\Delta H$ 1901-2100 (ZJ)	$\Delta H$ 1901-2200 (ZJ)	$\Delta H$ 1901-2300 (ZJ)	$\Delta H$ 1901-2100 (ZJ)	$\Delta H$ 1901-2200 (ZJ)	$\Delta H$ 1901-2300 (ZJ)	
42.1	6.03	24.14	26.91	27.74	44.41	78.13	92.64	
92.1	7.31	41.12	53.91	57.84	69.90	148.01	191.37	
142.1	7.63	45.96	69.59	81.52	75.65	178.98	255.66	
192.1	7.66	46.81	75.02	93.67	76.59	187.63	282.66	
242.1	7.66	46.94	76.35	98.15	76.73	189.52	291.36	
292.1	7.66	46.95	76.67	99.60	76.74	189.89	293.77	
342.1	7.66	46.96	76.75	100.00	76.72	189.92	294.31	

Table 1.2: Heat stored in the soil (upper 3.8 m) since 1901 CE in the year 2000 and predicted for the year 2300 CE for the RCP 4.5 and RCP 8.5 scenarios.

$d$ (m)	RCP 4.5				RCP 8.5			
	$\Delta H$ 1901-2000 (ZJ)	$\Delta H(d)/\Delta H(42.1)$ 1901-2000	$\Delta H$ 1901-2300 (ZJ)	$\Delta H(d)/\Delta H(42.1)$ 1901-2300	$\Delta H$ 1901-2000 (ZJ)	$\Delta H$ 1901-2300 (ZJ)	$\Delta H(d)/\Delta H(42.1)$ 1901-2300	$\Delta H(d)/\Delta H(42.1)$ 1901-2300
42.1	1.831	1	4.473	1	10.532	10.532	1	1
92.1	1.816	0.9917	4.465	0.9984	10.471	10.471	0.9942	0.9942
142.1	1.813	0.9904	4.441	0.9930	10.392	10.392	0.9867	0.9867
192.1	1.817	0.9926	4.427	0.9898	10.348	10.348	0.9826	0.9826
242.1	1.813	0.9904	4.419	0.9879	10.330	10.330	0.9809	0.9809
292.1	1.810	0.9885	4.412	0.9864	10.332	10.332	0.9810	0.9810
342.1	1.814	0.9908	4.411	0.9863	10.321	10.321	0.9800	0.9800

## CHAPTER II

### LOWER BOUNDARY CONDITIONS IN LAND SURFACE MODELS. PART 2: EFFECTS ON THE PERMAFROST AND CARBON POOLS.

#### 2.1 Abstract

The land subsurface component of Earth System Models (ESMs) use shallow bottom boundaries, much less than the depth reached by surface energy change in the centennial time-scale associated with recent climate change. Shallow boundaries reflect considerable energy to the surface, which along with the lack of a geothermal gradient in current land models, alter the surface energy balance and therefore affect permafrost in high latitudes and the stability of inert carbon in the permafrost. To estimate the real impact of these limitations, we modify the subsurface model in the Community Land Model version 4.5 (CLM4.5) by considering a (non-zero) crustal heat flux and increasing the thickness of the subsurface by 300 m. In Chapter I of this thesis, we demonstrated how these modifications change the thermal regime in the shallow subsurface. Here we find that increasing the thickness of the subsurface reduces the loss of near-surface permafrost between 1901 and 2300 by 1.6%-1.9%, and reduces the loss of soil carbon by 1.6%-3.6%. A crustal heat flux of  $0.08 \text{ W m}^{-2}$  has a small effect on permafrost extent in the Northern Hemisphere but is sufficient to produce local differences in the initial stable size of the soil carbon pool across the permafrost region, which reduces the loss of soil carbon by 4.4%-22.4% across the region. Methane production within

the Northern Hemisphere permafrost region is reduced by 1-1.6% by a crustal heat flux of  $0.08 \text{ W m}^{-2}$  and has variations smaller than 0.5% when increasing the thickness of the subsurface, but can variate as much as 50-80% in individual cells.

## 2.2 Introduction

Permafrost is defined as the ground that has remained below  $0^\circ\text{C}$  for at least two consecutive years (Harris et al., 1988). Permafrost covers 24% of the land of the northern hemisphere and it is widespread at high latitudes, where it dominates the biogeochemistry and the hydrology of the land, being an impermeable barrier for the movement of liquid water (Slater & Lawrence, 2013). Permafrost is also a large reservoir of inert organic carbon in the terrestrial system, storing an estimated 1100-1500 PgC ( $10^{15}\text{g}$  of C) of organic carbon, twice the carbon content of the pre-industrial atmosphere (Hugelius et al., 2014). Carbon in permafrost has a high potential to accelerate climate change and associated global warming, as rising temperatures at high latitudes destabilize permafrost and expose previously frozen carbon to microbial activity, releasing additional  $\text{CO}_2$  and  $\text{CH}_4$  into the atmosphere (Schuur et al., 2015). Because of the potential positive feedback of thawing permafrost on the climate system, the coupled models of ocean, atmosphere and land surface used for climate projections, known as Earth System Models (ESMs), endeavor to make robust assessments of future permafrost extent and retreat.

The current generation of ESMs use a variety of Land Surface Models (LSMs). These models were used in the Climate Model Intercomparison Project phase 5 (CMIP5), which show large disagreements in the simulation of present-day permafrost extent. The sensitivity of permafrost area to the increase of global temperatures shows a wide range of sensitivities across the different LSMs used in

CMIP5 ( $0.75 - 2.32 \times 10^6 \text{ km}^2 \text{ K}^{-1}$ ), which in terms of relative losses of permafrost area range between 6% to 29% per K of high-latitude warming (Slater & Lawrence, 2013; Koven et al., 2013).

These differences arise partly from biases in air temperature and snow depth in some models, but mostly from structural weaknesses of the land models that limit their skill to simulate subsurface processes in cold regions (Koven et al., 2013; Slater & Lawrence, 2013). Most of these land models rely on very shallow ( $\sim 3\text{-}42$  m) subsurface modules (Cuesta-Valero et al., 2016). Several works have pointed out that, in the centennial time scale of climate change, temperature variations at the land surface propagate to depths of hundreds of meters (MacDougall et al., 2008, 2010). Thus, the shallow depth of current land models hinders the propagation of surface heat signals into the subsurface. Under the current projections of climate change, the shallow bottom boundaries result in underestimating the heat absorbed by the land subsurface, and in overestimating the temperature increase in the shallow soil (Chapter I). These effects might contribute to the discrepancies among permafrost simulations in the CMIP5 models.

Another factor affecting the simulation of permafrost could be the use of a zero heat flux as thermal bottom boundary condition in most land models. This simplification has been assumed valid for thin (20-30 m) subsurfaces for time intervals less than a century (Nicolson et al., 2007). However, the geothermal gradient is necessary to capture the thermal dynamics of the subsurface when considering depths of hundreds of meters and time scales of several centuries.

Our aim is to estimate the impacts of the depth of the bottom boundary, and that of a non-zero heat flux bottom boundary condition, on permafrost dynamics and permafrost carbon content. We modify the thickness of the subsurface and the bottom boundary condition of the Community Land Model version 4.5 (CLM4.5)

(Oleson et al., 2013), the land model with the deepest (42.1 m) bottom boundary of those used in the CMIP5 (Stocker et al., 2013). To compare the original CLM4.5 and our modified versions, we run simulations between 1901 CE and 2300 CE, using a reconstruction of historical climate between 1901 and 2005 (Viovy, 2018), followed by two scenarios of moderate and high radiative forcings between 2005 and 2300 (Thomson et al., 2011; Riahi et al., 2011). Previously, we have determined the effect of these changes on the heat stored in the subsurface and the soil (Chapter I). Here, we study their effects on permafrost and the carbon pools.

## 2.3 Methodology

### 2.3.1 Community Land Model 4.5

The specifications of the land model are discussed in detail in Chapter I of this thesis and are briefly recapped below. The original land model has a thickness of  $d = 42.1$  m and zero heat flux  $F_B = 0$  W m<sup>-2</sup> as bottom boundary condition. We modify the land model by either increasing its thickness  $d$  to a maximum of  $d = 342.1$  m (by adding new bedrock layers) or by increasing the basal heat flux  $F_B$  used as bottom boundary condition in intervals of  $F_B = 0.02$  W m<sup>-2</sup>, to a maximum of  $F_B = 0.08$  W m<sup>-2</sup>.

### 2.3.2 Carbon model

The Community Land Model version 4.0 (CLM4.0) includes a representation of the carbon and nitrogen cycles (CLM4CN) largely based on the ecosystem process model Biome-BGC (Biome BioGeochemical Cycles) (Running & Hunt, 1993), which is an extension of the previous model Forest-BGC (Running & Gower, 1991). Forest-BGC simulates water, carbon, and nitrogen fluxes in forest ecosystems, which Biome-BGC expanded with more mechanistic descriptions of photo-

synthesis and by including more vegetation types in its parameterizations. Later versions of Biome-BGC (Thornton et al., 2002) developed the mechanistic calculations of carbon and nitrogen cycles in the soil, control of photosynthesis by nitrogen, differentiation of sunlit/shaded canopies, calculation of fire and harvest, and regrowth dynamics.

In CLM4.5 (Oleson et al., 2013), we work with the BioGeoChemistry (BGC) carbon model (Riley et al., 2011). The BGC model expands the Carbon-Nitrogen (CN) model by adding a submodel of production, oxidation and emission of methane. CLM4.5 also includes updates to photosynthesis, vegetation and hydrology from CLM4.0. This improves carbon treatment in CLM4.5-BGC significantly over CLM4.0CN.

As the schema in Fig. 2.01 shows, there are three main carbon pools in CLM4.5-BGC: the vegetation, the litter (and coarse wood debris), and the soil organic matter (or soil carbon). These pools are subdivided into several sub-pools. The vegetation has distinct pools to account for the different tissues of the plants: leafs, dead/live stems, live/dead coarse roots, fine roots, and a internal storage pool (from where the plants can take carbon when they can not photosynthesize). Litter and carbon are each defined in the same 10 vertical soil layers used for hydrology, and with 3 separate pools each (corresponding to increasingly recalcitrant forms of carbon) arranged as a converging cascade from coarse wood to litter to soil, a structure known as the Century Soil Carbon pool structure (Oleson et al., 2013).

The methane model (Fig. 2.01) produces  $\text{CH}_4$  in the anaerobic fraction of the soil in a land cell (which can be fractionally inundated in CLM4.5), that consists of the entire soil in the inundated portion of the land cell, and the fraction of soil bellow the water table in the non-inundated portion. The  $\text{CH}_4$  stays in the

inundated soil where is produced for a short time, until it rises to the atmosphere by ebullition (Wania et al., 2010). Thus, the production of methane is closely correlated with the hydrology model. In the CLM4.5 hydrology model, the land can store water within the soil (with a thickness of 3.8 m globally, but variable hydrological properties due to its composition) and in an unconfined aquifer with a capacity of 5000 mm globally, implemented as a virtual layer (which does not interact with the subsurface other than to store water) beneath the soil (Oleson et al., 2013). In reality, soil thickness is highly variable worldwide, reaching depths of hundreds of meters in some areas, while the global mean is estimated at  $\approx 13$  m (Shangguan et al., 2017).

### 2.3.3 Permafrost treatment

We define a subsurface layer as permafrost if it remains 2 consecutive years below 0 °C. This definition does not account for the water/ice content of a layer, as we want to also define permafrost as well for bedrock layers where no water is present. As the ice content in the soil hinders the movement of liquid water within it, permafrost is closely linked with the hydrology model.

Near surface permafrost is commonly defined as the permafrost present within the upper 3 m of the soil (Nicolsky et al., 2007; Koven et al., 2011; Schuur et al., 2015), but this depth can be different for some land models where the soil depth is larger than 3 m (Lawrence & Slater, 2005). As in CLM4.5 the soil layers make the upper 3.8 m of the land column, we define near-surface permafrost as the permafrost present above this depth.

Because natural soils can reach deeper than the 3.8 m used in CLM4.5, we aim at gaining some insight on how bottom heat flux and model thickness affect permafrost deeper than 3.8 m. However, it is outside the scope of this study to implement a realistic soil thickness in CLM4.5. For this reason we will also study

the permafrost present between the surface and a depth of 42.1 m, the thickness of the thinnest of our model versions, which we define as intermediate-depth permafrost.

While near-surface permafrost and intermediate-depth permafrost define permafrost within a depth range, to study the maximum depth of permafrost we use the concept of Active Layer Thickness (ALT). In environments containing permafrost, the active layer is the upper layer of soil that thaws during summer. The ALT is the maximum depth at which annual temperature variations at the surface are able to thaw the soil, which coincides with the upper limit of permafrost. ALT provides a more complete information on permafrost than the areal extent of soil permafrost, as variations in the thermal regime of the subsurface can displace the upper limit of permafrost in the soil and therefore the ALT, but be too small to completely thaw the permafrost within the soil.

We are interested in how the modifications to the bottom boundary produce changes in the carbon pools of the permafrost region, and the areal extent of the permafrost region evolves in time. To avoid ambiguities, we define a constant region of study, as the region of the Northern Hemisphere where near-surface permafrost is present at the initial time of the simulations in 1901 CE (see Fig. 2.02). This region covers parts of Northern Canada, Alaska, Siberia, Tibet, Inner Scandinavia, and the coast of Greenland. The interior of Greenland, covered by glaciers, is not included in CLM4.5 but it is part of the land-ice model of Community Earth System Model version 1.2 (CESM1.2).

#### 2.3.4 Simulation of the 1901-2300 period

As we described in Chapter I of this thesis, we compare the results of different versions of the CLM4.5 obtained by changing the depth  $d$  of the bottom boundary or the crustal heat flux  $F_B$  at the lower boundary, for the period 1901-2300. The

land model uses forcings of humidity, temperature, aerosol and CO<sub>2</sub> concentrations and longwave/shortwave radiation from the lower level of the atmosphere. These forcings are the same for every model version, because we run the land model uncoupled. The forcing data are taken from two datasets, which divide the simulation period in two phases between 1901-2005 and 2006-2300.

In the first phase of the simulation we use the CRUNCEP dataset (Viovy, 2018), a historical reconstruction of global climatological data of the 20th century, to force the land model between 1901 and 2005. CRUNCEP is a combination of the Climate Research Unit Time-Series (CRU-TS) monthly climatology (Harris et al., 2014) and the National Centers for Environmental Prediction (NCEP) reanalysis (Kalnay et al., 1996).

In the second phase, we force the land model between 2006 and 2300 using the atmospheric output from a simulation of a specific Representative Concentration Pathway (RCP) (Van Vuuren et al., 2011). We divide our simulation after 2005 following two different pathways, RCP 4.5 and RCP 8.5. RCP 4.5 is a scenario of mitigation of anthropogenic greenhouse gas emissions under which radiative forcing is 4.5 W m<sup>-2</sup> by year 2100 (Thomson et al., 2011). RCP 8.5 is a scenario of increased greenhouse gas emissions that leads to a radiative forcing of 8.5 W m<sup>-2</sup> by year 2100 (Riahi et al., 2011). A forcing dataset of monthly atmospheric values for both RCP scenarios was obtained from the Earth System Grid (Stern, 2013). To produce a 6h-resolution dataset for use in the CLM4.5 from these monthly datasets, we took the 6h-anomalies to monthly average for temperature and precipitation in the years 1996-2005 from the CRUNCEP dataset. We then combined these 10 years of anomalies with the monthly dataset (in cycles of 10 years) to produce a 6h-resolution dataset.

As the CLM4.5 requires data at a resolution of 6 hours, we retrieved the 6-hour

anomalies from the monthly mean data for temperature and precipitation for the time interval from 1996 to 2005 retrieved from the CRUNCEP dataset. We then combined these 10 years of anomalies cyclically with the dataset of monthly atmospheric values from the Earth System Grid, to produce a 6h-resolution dataset.

Over the Northern Hemisphere permafrost region, the mean Surface Air Temperature (SAT) between 2290-2300 is  $\approx 3$  K higher than between 2000-2010 for the RCP 4.5 scenario, while it increases by  $\approx 14$  K for the RCP 8.5 scenario (Fig. 2.03).

## 2.4 Results: Permafrost

### 2.4.1 Intermediate-depth Permafrost

Given the increasing SAT anomalies used to force the model (Fig. 1.03), we expect to observe a continuous decrease in the area extent of permafrost during the simulation period. The SAT warming signal is expected to propagate downward and, for a shallow bottom boundary, to be reflected back to the surface, thus overheating the subsurface. A deeper bottom boundary attenuates this effect and therefore decreases the rate of permafrost thawing. Because a shallow lower boundary heats the subsurface from the bottom, this overheating is highest at depth, and the effect on the soil is less noticeable.

In our simulations, the area with intermediate-depth permafrost in the Northern Hemisphere (Fig. 2.04) has an initial areal extent of  $20.4 \times 10^6$  km<sup>2</sup> in 1901. At the end of the RCP 4.5 scenario, this area has been reduced by  $4.94 \times 10^6$  km<sup>2</sup> (24.1%) for the thinnest model and by  $1.59 \times 10^6$  km<sup>2</sup> (7.8%) for the thickest model. For the RCP 8.5 scenario, the area losses of intermediate-depth permafrost are  $14.85 \times 10^6$  km<sup>2</sup> (72.7%) for the thinnest model and  $2.74 \times 10^6$  km<sup>2</sup> (13.4%) for the thickest model.

For both scenarios, the decrease of intermediate-depth permafrost area becomes smaller as we increase the depth of the bottom boundary (Fig. 2.05). Each increase of the thickness of the subsurface produces diminishing returns, reaching a plateau where the permafrost area is not affected by a further increase of the bottom boundary depth. The depth at which this plateau is reached increases with the length of the simulation, and by the end of the simulations at 2300, it exceeds the largest bottom boundary depth (342.1 m) used in our versions of the model. Table 2.1 summarizes the evolution of intermediate-depth permafrost for the original CLM4.5 and the modified versions of  $d = 342.1$  m and  $F_B = 0.08$  W m<sup>-2</sup>.

The addition of a non-zero heat flux boundary condition at the LSM's bottom boundary has a small effect on intermediate-depth permafrost area (Fig. 2.06). The initial extent of intermediate-depth permafrost is reduced by  $0.15 \pm 0.07 \times 10^6$  km<sup>2</sup> (0.7%) for every increase of 0.02 W m<sup>-2</sup> in  $F_B$ . This difference does not remain constant during the simulation, each increase 0.02 W m<sup>-2</sup> of  $F_B$  reduces the intermediate-depth permafrost area at the end of the simulation by  $0.19 \pm 0.14 \times 10^6$  km<sup>2</sup> in the RCP 4.5 scenario (Fig. 2.06a) and by  $0.12 \pm 0.05 \times 10^6$  km<sup>2</sup> in the RCP 8.5 scenario, a decrease relative to the initial permafrost extent of 2.1% and 1.2% respectively (Fig. 2.06b).

#### 2.4.2 Near-surface permafrost

The near-surface permafrost (within the upper 3.8 m) area in the Northern Hemisphere is much less affected by the thickness of the model than the intermediate-depth permafrost (Fig. 2.07). The initial extent of near-surface permafrost is  $18.45 \times 10^6$  km<sup>2</sup>, and by 2300 under the RCP 4.5, this area has been reduced by  $4.27 \times 10^6$  km<sup>2</sup> (23.1%) for the thinnest model and  $4.20 \times 10^6$  km<sup>2</sup> (22.7%) for the thickest model, a relative difference of 1.6%. In the RCP 8.5 case, the

permafrost area is reduced by  $13.37 \times 10^6 \text{ km}^2$  (72.5%) for the thinnest model and  $13.11 \times 10^6 \text{ km}^2$  (71.1%) for the thickest model, an area decrease 1.9% smaller.

The effect of the bottom heat flux  $F_B$  on near-surface permafrost area is similar to that on intermediate-depth permafrost, but quantitatively smaller (Fig. 2.08). Each  $0.02 \text{ W m}^{-2}$  increase reduces the initial near-surface permafrost extent by  $0.05 \pm 0.04 \times 10^6 \text{ km}^2$  (0.3%). At 2300, this increase in bottom heat flux reduces the final permafrost extent by  $0.09 \pm 0.08 \times 10^6 \text{ km}^2$  (0.6%) for the RCP 4.5 scenario and by  $0.04 \pm 0.01 \times 10^6 \text{ km}^2$  (0.8%) for the RCP 8.5 scenario (Fig. 2.08b). The results for the original CLM4.5 and the modified versions of  $d = 342.1 \text{ m}$  and  $F_B = 0.08 \text{ W m}^{-2}$  are summarized in Table 2.2.

The initial state of the subsurface in 1901 is identical for model versions with different subsurface thickness, provided they use the same bottom heat flux. The temperature of the upper subsurface increases at a slower rate for a deeper bottom boundary, thus the ALT increases at a slower rate for model versions with deeper subsurface. At the end of the simulations in 2300, the ALT is visibly larger for the original model (42.1 m) than for the model with thickness increased to 342.1 m, for both scenarios (Fig. 2.09).

The bottom heat flux increases temperature proportionally to the flux and the depth. Therefore, bottom heat flux does not alter ALT if permafrost is shallow. Where ALT is large, the higher temperature due to the bottom heat flux is enough to induce thawing and lower the upper limit of permafrost (Fig. 2.09).

## 2.5 Results: Carbon

### 2.5.1 Soil Carbon

The size of the soil carbon pool increases during the first  $\approx 150$  yr of simulation and thereafter begins decreasing. Increasing the depth of the bottom boundary

reduces the loss of soil carbon, as expected because it slows the rate of permafrost thawing. The loss of soil carbon for the thickest subsurface (342.1 m) is 0.15 PgC (3.6%) less than for the thinnest subsurface model (42.1 m) in the RCP 4.5 scenario, and 0.56 PgC (1.3%) less in the RCP 8.5 scenario (Fig. 2.10).

Increasing the bottom heat flux  $F_B$  slows down the rate at which soil carbon in the permafrost region decreases during the simulation. An increase of  $0.02 \text{ W m}^{-2}$  reduces the loss of soil carbon between 1901 and 2300 by  $0.3 \pm 0.1 \text{ PgC}$  (5.6% of the decrease of soil carbon in this period for the original CLM4.5) in the RCP 4.5 scenario and  $0.45 \pm 0.2 \text{ PgC}$  (1.1%) in the RCP 8.5 scenario (Fig. 2.11).

Because the changes in soil carbon due to the modification of model thickness and bottom heat flux are very small relative to the size of the pool, we have calculated the difference in soil carbon between the original model and the modified models with increased thickness  $d = 342.1 \text{ m}$  and with bottom heat flux  $F_B = 0.08 \text{ W m}^{-2}$ . For the original model, the biggest concentrations of soil carbon are located in the permafrost regions of the northern hemisphere, mainly in Alaska and Eastern Siberia (Fig. 2.12). While model versions of different thickness share a common initial state, a thicker model increases soil carbon concentration across the region.

Models with different bottom heat flux  $F_B$  depart from different initial conditions (since the bottom heat flux determines the thermal steady state of the subsurface). A higher  $F_B$  decreases the initial concentration of soil carbon in some areas but increases it in others. These differences can be of the same order of magnitude as the carbon concentration in the original model in token gridcells. Some cells have quantities of soil carbon in the  $F_B = 0.08 \text{ W m}^{-2}$  model half of that of the original model, while other have 10 times as much (Fig. 2.12).

As the local differences on the soil carbon pool due to the bottom heat flux have

different signs, the effect on the whole region is proportionally much smaller (Fig. 2.13). The absence of a consistent trend in the size of the soil carbon pool as we increase the bottom heat flux is due to the regional variability seen in Fig. 2.12, since the soil carbon in each gridcell can either increase or decrease due to the basal heat flux.

### 2.5.2 Vegetation Carbon

The vegetation carbon in the Northern hemisphere is also affected by the depth of the bottom boundary. Because rising temperatures allow plants to colonize higher latitudes, the vegetation increases for both RCP scenarios, reaching a stable level between 2100-2300 (Fig. 2.14). While the models with different depth of the bottom boundary  $d$  depart from the same initial state at 1901, increasing the thickness of the model leads to slightly smaller masses of vegetation carbon. For the thickest model (342.1 m), the pool of vegetation carbon is  $0.17 \pm 0.01$  PgC smaller during the last two centuries of simulation than it is for the thinnest model (42.1 m) for the RCP 4.5 scenario, and  $0.11 \pm 0.08$  PgC smaller for the RCP 8.5 scenario.

The bottom heat flux also has a small effect in the evolution of vegetation carbon in the Northern Hemisphere for both RCP scenarios (Fig. 2.15). The average vegetation carbon between 2100-2300 for the model with  $F_B = 0.08 \text{ W m}^{-2}$  is  $0.35 \pm 0.03$  PgC less for the RCP 4.5 scenario and  $0.54 \pm 0.05$  PgC less for the RCP 8.5 scenario than for the model with zero basal heat flux, a relative decrease of  $0.8 \pm 0.08\%$  and  $1.2 \pm 1\%$  respectively.

Increasing  $d$  and  $F_B$  results in a larger amount of vegetation carbon in some areas and a smaller quantity in others (Fig. 2.16). At the end of the simulation, the effect is a net decrease of vegetation carbon in the Northern Hemisphere for both RCP scenarios and for both increased thickness and increased bottom heat flux.

The bottom heat flux changes the initial stable size of the vegetation carbon pool in individual cells, that results in a positive change over the North Hemisphere permafrost region (Fig. 2.17). There is a consistent linear increase of  $0.066 \pm 0.02$  PgC of the initial vegetation for each  $0.02 \text{ W m}^{-2}$  increase of the bottom heat flux.

### 2.5.3 Methane

Methane is produced by methanogenic microbes in the anaerobic fraction of soil. Therefore, it concentrates in areas where the water table rises high enough to reach the carbon-rich soil near the surface, or in inundated areas. The production of methane in natural wetlands is mainly located in the tropical areas, responsible for 64%-88% of the global wetland production (O'Connor et al., 2010).

In our CLM4.5-BGC simulations, most of the methane production is concentrated in the Northern Hemisphere cold regions, including not only the permafrost region but the areas of seasonal soil freezing as well (Fig. 2.18). In contrast, the tropical areas produce almost no methane. The reason lies in the unconfined aquifer present below the soil in the hydrological model of the CLM4.5, which greatly increases the capacity of the subsurface to absorb water before the water table can rise to the upper soil layers, where most of the soil carbon is concentrated. In the simulations, the water table rarely rises above a depth of 3.8 m during the monsoon season. High-latitude areas have low water tables as well, but get partially inundated during the year because the soil is frozen (impeding the filtration of water), and can produce methane.

In the Northern Hemisphere there are significant differences in the production of methane due to the bottom heat flux and the depth of the bottom boundary. These differences occur in a few areas where the difference in methane production can be within 50-80% of that of the original model. However, as the sign of

these differences can be either positive or negative, the net effect over methane production is small.

The net effect of the subsurface thickness and the bottom heat flux on the global methane production is much smaller than for the localized areas displayed in Fig. 2.18 (Figs. 2.19 and 2.20). Increasing the thickness of the model from 42.1 m to 342.1 m can result in increases and decreases of global methane production during the simulation between 0.1 to 0.2 TgC yr<sup>-1</sup> (1 TgC = 10<sup>12</sup> g of C), only 0.3-0.5% of the methane production at 2300 for the scenarios RCP 4.5 and RCP 8.5, respectively. The bottom heat flux has a larger effect, as a bottom heat flux of  $F_B = 0.08 \text{ W m}^{-2}$  decreases methane production by 0.6 to 1.0 TgC yr<sup>-1</sup>, a relative decrease of 1-1.6% of the total production at 2300 for the scenarios RCP 4.5 and RCP 8.5, respectively.

## 2.6 Discussion and Conclusions

In Chapter I we established that the depth of the bottom boundary affects heat propagation over time, as a shallow subsurface hinders the propagation of the thermal signal downwards, leading to additional heating of the subsurface. On the other hand, the heat flux used as bottom boundary does not affect thermal propagation, but offsets the heat content of the subsurface. Both these effects are larger at depth than for the soil, close to the surface.

Permafrost is affected by the depth of the bottom boundary, in a degree that depends of the depth to which we consider permafrost, in the same manner as the heat absorption by the subsurface have been shown to be affected in Chapter I of this thesis. Permafrost near the surface is only slightly affected, but as we increase the depth to which we consider permafrost, the differences made by the thickness of the model became more and more significant. Increasing the thickness of the subsurface from 42.1 m to 342.1 m reduces the area loss of intermediate-depth

permafrost by a factor of 3 in the RCP 4.5 scenario and by a factor of 5.5 in the RCP 8.5 scenario (Fig. 2.04). The effect of the crustal heat flux in permafrost is proportional to the value of the heat flux and the depth of the permafrost, but even a bottom heat flux of  $F_B = 0.08 \text{ W m}^{-2}$  reduces intermediate-depth permafrost extent by only 1-2%.

Increasing the depth of the bottom boundary leads to less vegetation and more soil carbon in the Northern Hemisphere permafrost region at the end of the simulations, compared to the thinner models. This is to be expected, as the increasing the depth of the subsurface leads to reduced permafrost loss, which opens less area to vegetation and exposes less soil carbon to microbial activity. These effects are small, as the stable vegetation level reached between 2100-2300 in the thickest model is only reduced by 0.8-1.2% compared to the thinnest model, while soil carbon is reduced by 1.3-3.6%.

A higher basal heat flux has a regionally variable effect across the Northern Hemisphere, increasing soil carbon and vegetation where near-surface permafrost is present, but decreasing both outside of the permafrost region. The loss of soil carbon in the permafrost region is 4-22% smaller with  $F_B = 0.08 \text{ W m}^{-2}$  than with zero basal heat flux, while the initial quantities of carbon can range from half to 10 times as much in individual gridcells. This heat flux also reduces by 0.8-1.2% the stable vegetation level in this region during the last two centuries of the simulation. On the other hand, the bottom heat flux reduces methane production within areas where permafrost is present but increases it where soil only freezes seasonally.

In CLM4.5 subsurface biogeochemistry only takes place within the soil, the upper 3.8 m. For this reason, the small effect of the bottom boundary depth on near-surface permafrost translates into a small effect on the soil carbon and vegetation

pools and the methane production. While the same could be expected from the basal heat flux, it has a varied effect across the Northern Hemisphere, specially in the areas where seasonal freezing of the soil occurs, but no soil permafrost is present.

While in nature the bottom heat flux is not uniform, the use of uniform values allows us to establish a quantitative relationship between the magnitude of the bottom heat flow and the effects it has in permafrost and biogeochemistry. We also keep other simplifications made in CLM4.5, such as a global granitic bedrock and a constant regolith thickness of a few meters. Quantifying the effect of these simplifications would require important code modifications and more simulations, thus more time and computational resources. Also, while there exist maps of regolith thickness and bedrock composition as well as crustal heat flow (Clair et al., 2015; Jaupart & Mareschal, 2015), these maps are incomplete with many regions void of data.

While CLM4.5 uses as uniform soil thickness value of 3.8 m, natural soil thickness varies notably, with an estimated global mean of  $\approx 13$  m and reaching depths of several hundred meters in some areas (Shangguan et al., 2017). Soil affected by permafrost is therefore much deeper than in CLM4.5, and future models should use realistic maps of soil thickness, which makes the results obtained for intermediate-depth permafrost useful to understand the effects that the thickness of the subsurface and the bottom heat flux would have in a soil of realistic depth. The uniform soil thickness also affects the hydrology model in CLM4.5, which in addition to the use of an aquifer with a capacity of 5000 mm, uniform across the entire land system, makes the hydrology model unrealistic. The excessive capacity of this aquifer results in the water table rarely rising above 3.8 m depth, much lower than the natural levels of the water table, specially for the tropical wetlands (Fan et al., 2013). The newer version Community Land Model version 5.0 (CLM5.0)

attempts to address the main issues of the hydrology model in CLM4.5 by eliminating the aquifer and including a spatially variable soil thickness within a range of 0.4 m to 8.5 m, which is still below the global average (Lawrence et al., 2018). The soil thickness is derived from survey data where typical values of soil thickness are between 7 m and 10 m (Pelletier et al., 2016), although the growing consensus is that regolith thickness varies between 10-40 m (Clair et al., 2015).

The increased depth of soil in some areas imply that the effect of the basal heat flux and the bottom boundary depth would be bigger than our estimations, made for a soil depth of 3.8 m. While soil carbon pools in the permafrost region concentrate within the upper 3 m, additional reserves exist below 3 m which contain  $\sim 60\%$  as much carbon as the upper 3 m (Hugelius et al., 2014). If included in the model, these reserves would be more severely affected by the depth of the bottom boundary and the bottom heat flux than the shallow carbon deposits are.

The methane production in CLM4.5-BGC is dependent on the hydrology model used in CLM4.5, which keeps the water table too low in the tropical regions of the Earth where most (64%-88%) wetland methane is produced (O'Connor et al., 2010). The consequence is that no methane is produced in these regions, and all methane is produced in the Northern Hemisphere where frozen soil can be inundated. Compared to the original model, a bottom heat flux of  $F_B = 0.08 \text{ W m}^{-2}$  causes a reduction of 1-1.6% across the whole permafrost region, while deepening the bottom boundary to 342.1 m only induces variations smaller than 0.5%. However, there can be differences as high as 50-80% with respect to the original model, located in individual cells near the permafrost frontier. The lack of methane production in tropical regions associated to the hydrology should no longer occur in CLM5.0, which addresses the lack of realism of the hydrology model in CLM4.5.

The depth of the bottom boundary and the basal heat flux used at the bottom boundary have small but non-negligible effects on the carbon pools and fluxes in the North Hemisphere. These effects are not distributed homogeneously across the region, but located in small areas across the region. These areas are those where permafrost is the most affected by the bottom boundary depth and the basal heat flux, or that are located just outside the limit of the region where soil permafrost exists, which suggests that seasonal soil freezing also affects the carbon pools significantly. Methane production can vary by one order of magnitude due to the changes to model thickness and basal heat flux.

The local variability observed across the Northern Hemisphere could be explained as a result of the hydrological model. Permafrost acts as a barrier for the filtration of liquid water from the ground surface, which implies that the soil layers above frozen layers retain liquid water, necessary for vegetation root uptake and methane production. Increasing the heat content of the soil, for instance by increasing the crustal heat flux, increases the number of soil layers that can get inundated, thus increasing methane production and vegetation growth. However, if the last frozen soil layer thaws, the water is able to filter to the aquifer and methane production and vegetation growth decrease. The latter would happen in areas of seasonal soil freezing and in the periphery of the permafrost region, while the former would happen in colder areas where heating the soil is not enough to thaw the bottom soil layer. If methane production increases, the soil carbon pool would decrease due to the aggregated affect over time of the increased methane production. The contrary effect would happen when increasing the thickness of the subsurface, as it has the effect of decreasing the amount of heat within the soil. This explanation fits with most of the observations in Figs. 2.12, 2.16 and 2.18, except for some isolated cells.

In this paper we have researched the effects of two simplifications made by most

ESMs: not taking the geothermal gradient into account, and using an excessively thin subsurface. This paper follows previous estimations (MacDougall et al., 2008, 2010) and quantifies the effects of these simplifications, through the use of numerical simulations with two sets of modified versions of CLM4.5, one where we increase the thickness of the subsurface, and another where we impose a uniform heat flux at the bottom of the land model.

#### Code availability

The modified CLM4.5 software, as well as the instructions for its use in a functional CLM4.5 installation, are available in the Zenodo repository (<https://zenodo.org/record/1420497>) under the doi 10.5281/zenodo.1420497 (Hermoso de Mendoza, 2018).

#### Data availability

The dataset used to produce the initial conditions used in the simulations can be found in the Zenodo repository (<https://zenodo.org/record/1420497>) under the doi 10.5281/zenodo.1420497 (Hermoso de Mendoza, 2018). Implementation of these initial conditions requires modifications to the software, which can be found in the same package.

Three datasets are used as boundary conditions for the simulations (i.e. the atmospheric datasets used to force the land model). The CRUNCEP dataset used to force the model between 1901-2005 is available in the NCAR-UCAR Research Data Archive (Viovy, 2018). The two datasets used to force the model between 2006-2300, RCP 4.5 and RCP 8.5, are available in the Earth System Grid repository (Stern, 2013).

## 2.7 Acknowledgements

This work was supported by a Discovery grant from the Natural Sciences and Engineering Research Council of Canada (NSERC DG 140576948) and by the Canada Research Chair Program (CRC 230687) to H. Beltrami.

Computational facilities were provided by the Atlantic Computational Excellence Network (ACEnet-Compute Canada) with support from the Canadian Foundation for Innovation. H. Beltrami holds a Canada Research Chair in Climate Dynamics. Ignacio Hermoso was funded by graduate fellowships from a NSERC-CREATE Training Program in Climate Sciences based at St. Francis Xavier University and by further support from the faculty of sciences at UQAM.

Andrew H. MacDougall acknowledges support from the NSERC Discovery Grant program.

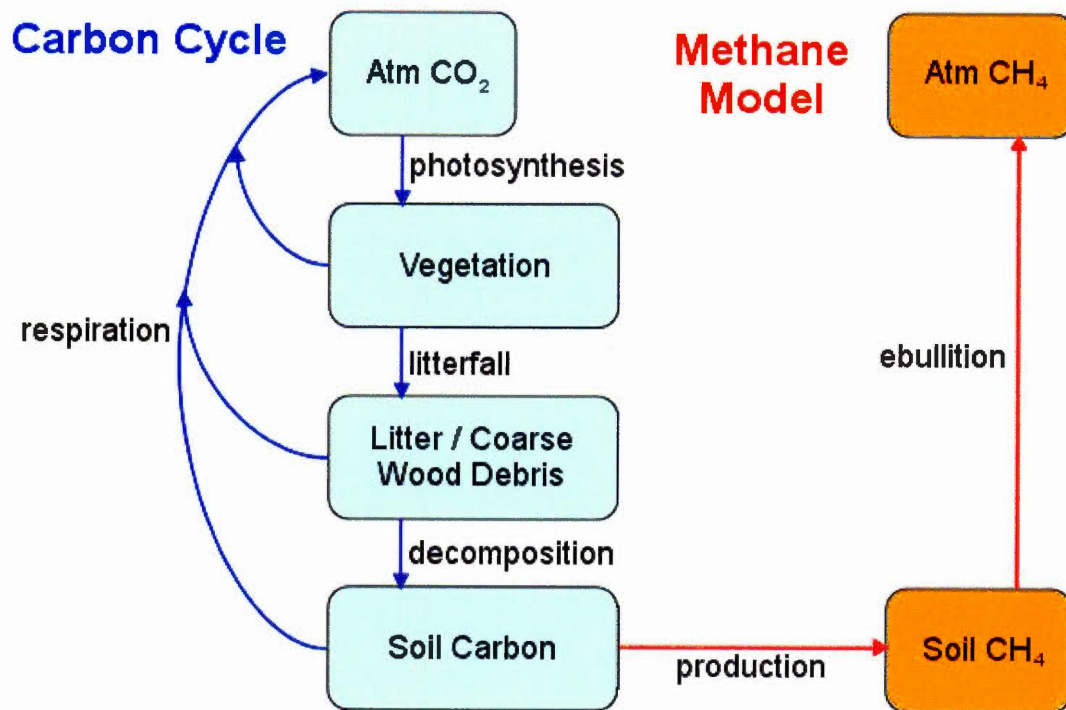


Figure 2.01: Schema of the carbon flux in CLM4.5-BGC. Figure redrawn from Oleson et al. (2013).

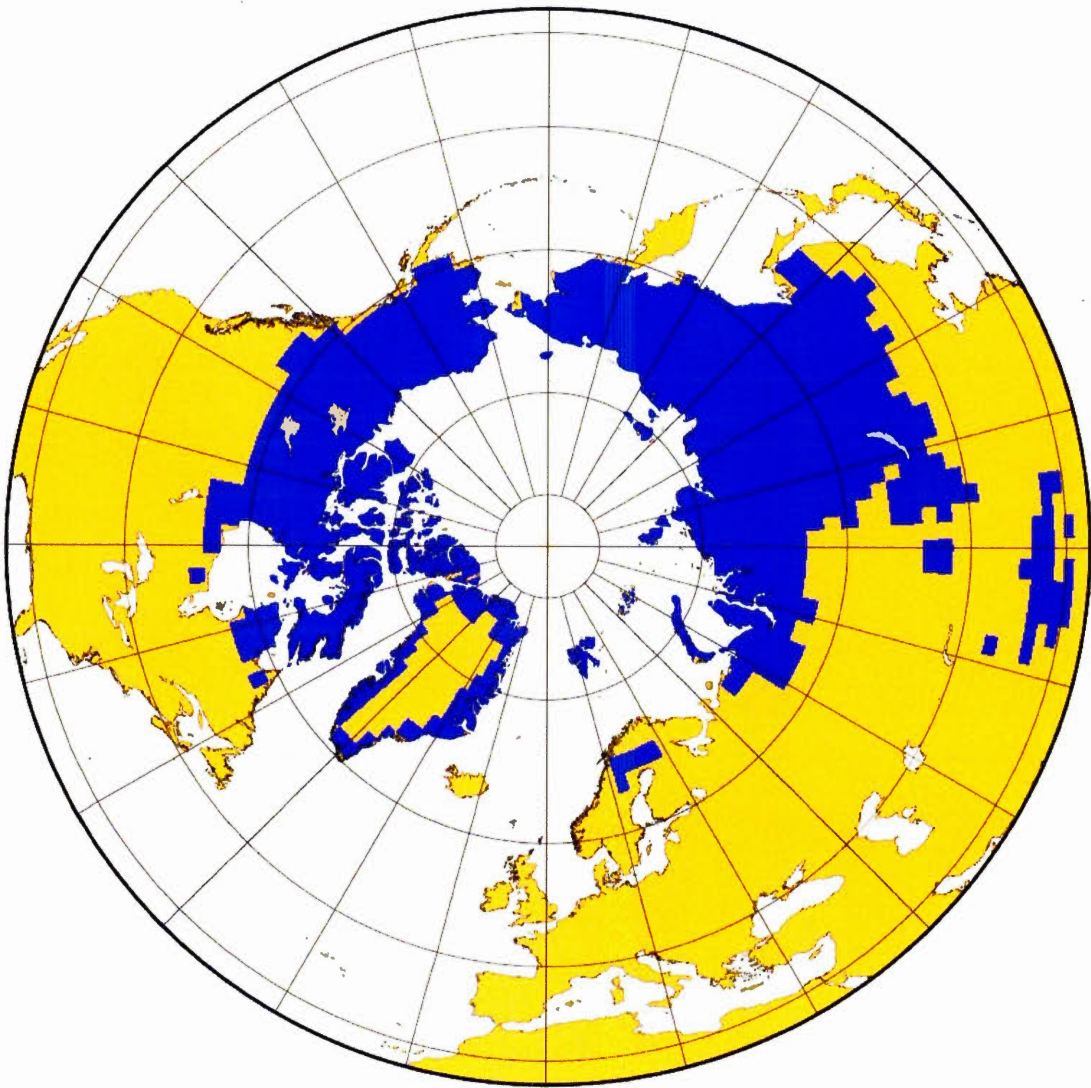


Figure 2.02: Region of study (blue), which corresponds to the extent of near-surface permafrost in the Northern Hemisphere in the year 1901, for the original CLM4.5 model.

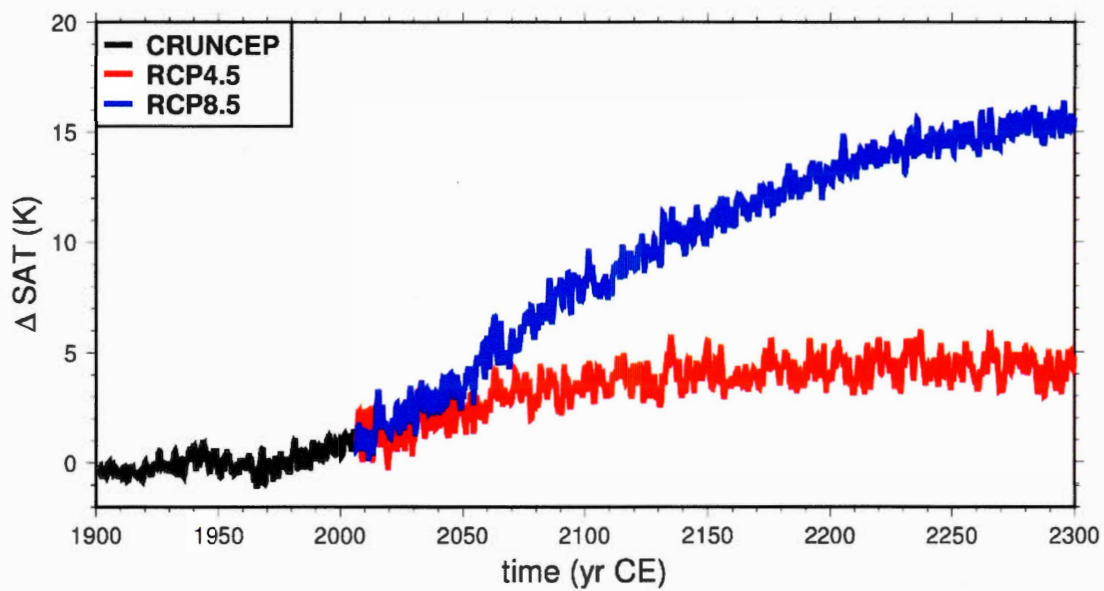


Figure 2.03: Mean Surface Air Temperature (SAT) over the region of study relative to the 20th century mean, from the CRUNCEP dataset (black) and the RCP 4.5 (red) and RCP 8.5 (blue) scenarios.

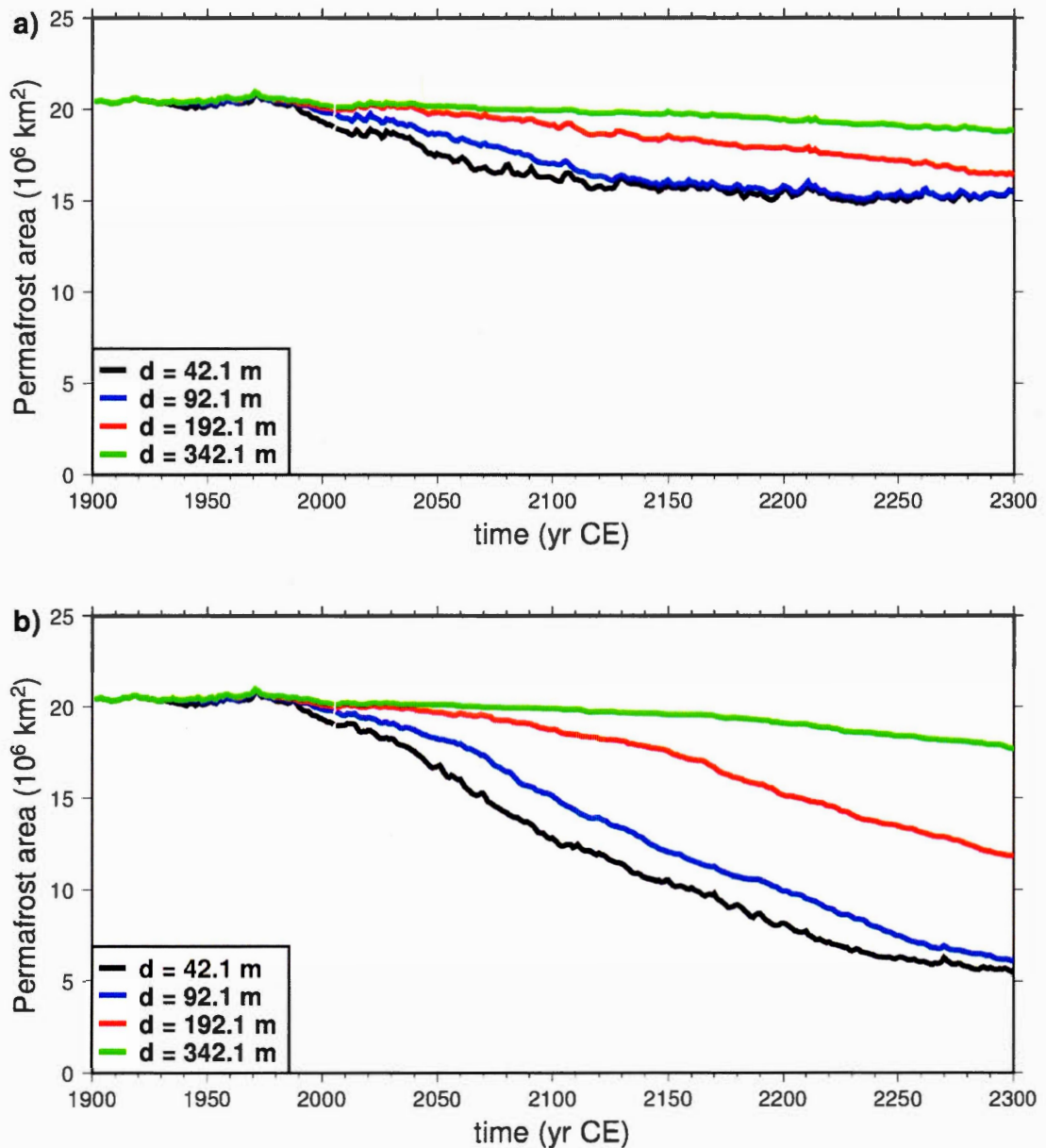


Figure 2.04: Northern Hemisphere intermediate-depth (0-42.1 m) permafrost area as function of time. Model versions with bottom boundary depth  $d$  at 42.1 m (black), 92.1 m (blue) 192.1 m (red) and 342.1 m (green). a) Simulations forced with CRUNCEP + RCP 4.5 data. b) Simulations forced with CRUNCEP + RCP 8.5 data.

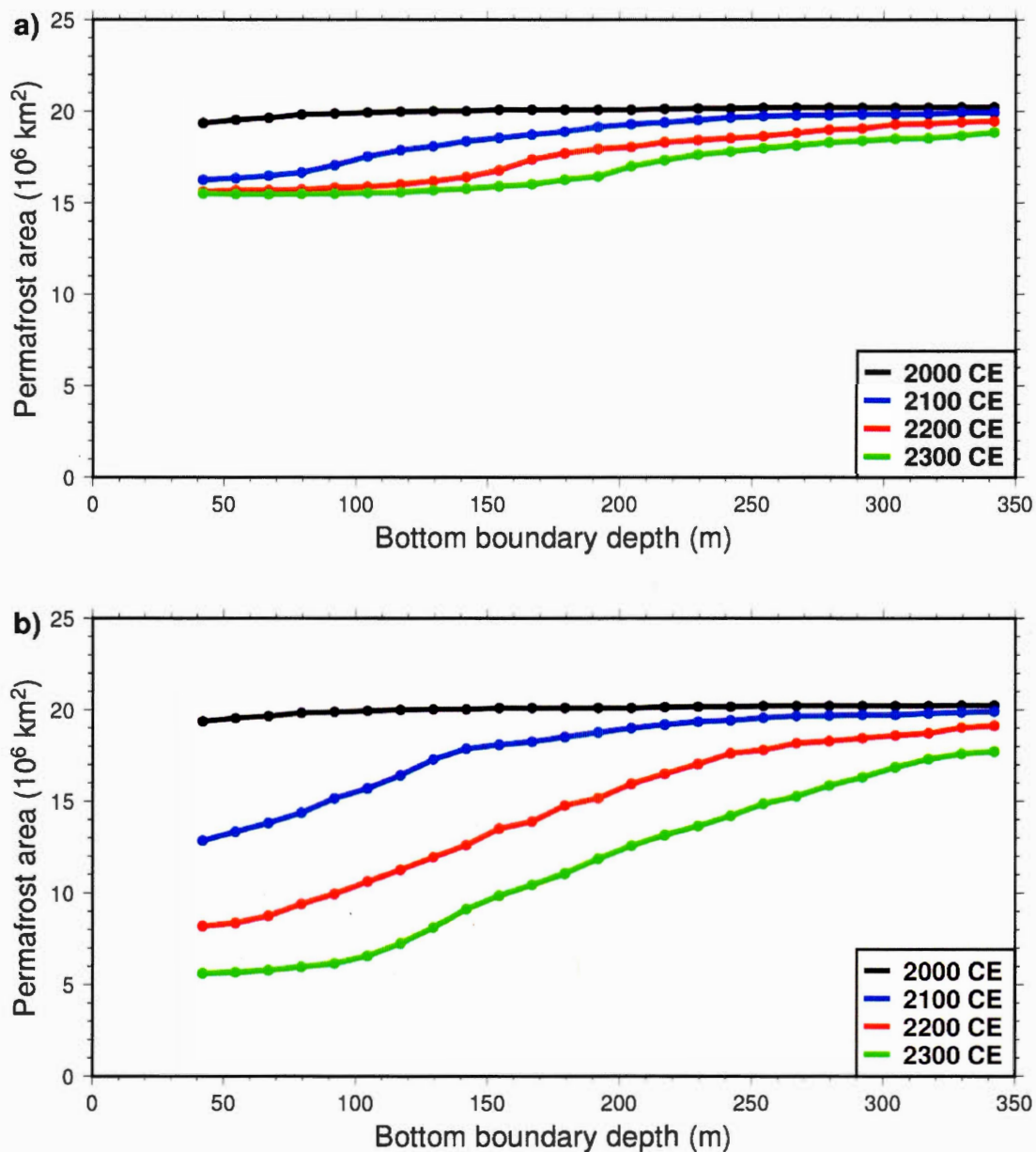


Figure 2.05: Northern Hemisphere intermediate-depth permafrost area as function of subsurface thickness  $d$ , at the years 2000 (black), 2100 (blue), 2200 (red) and 2300 (green). a) Simulations forced with CRUNCEP + RCP 4.5 data. b) Simulations forced with CRUNCEP + RCP 8.5 data.

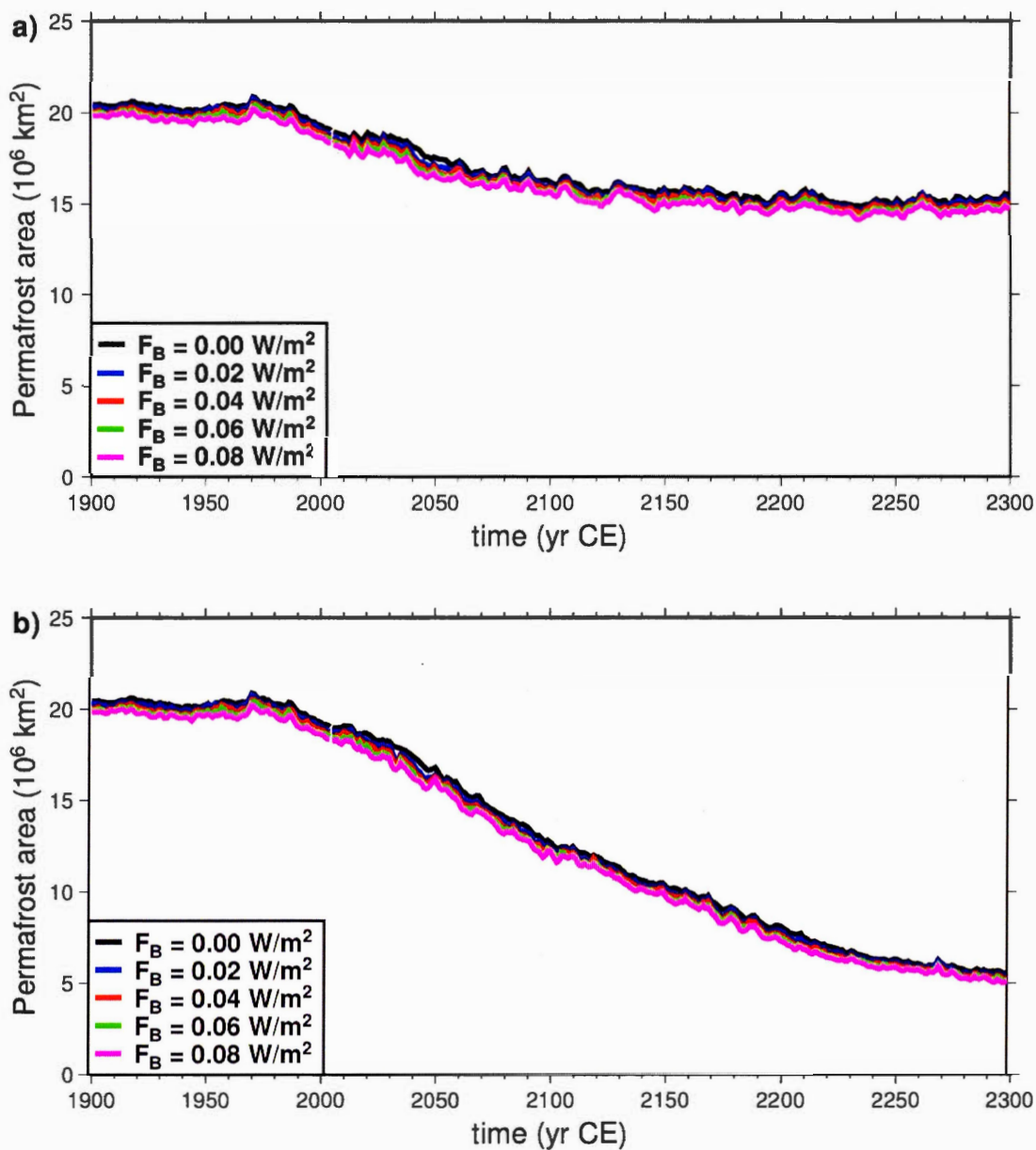


Figure 2.06: Northern Hemisphere intermediate-depth permafrost area as function of time. Model versions using different heat flux as bottom boundary. a) Simulations forced with CRUNCEP + RCP 4.5 data. b) Simulations forced with CRUNCEP + RCP 8.5 data.

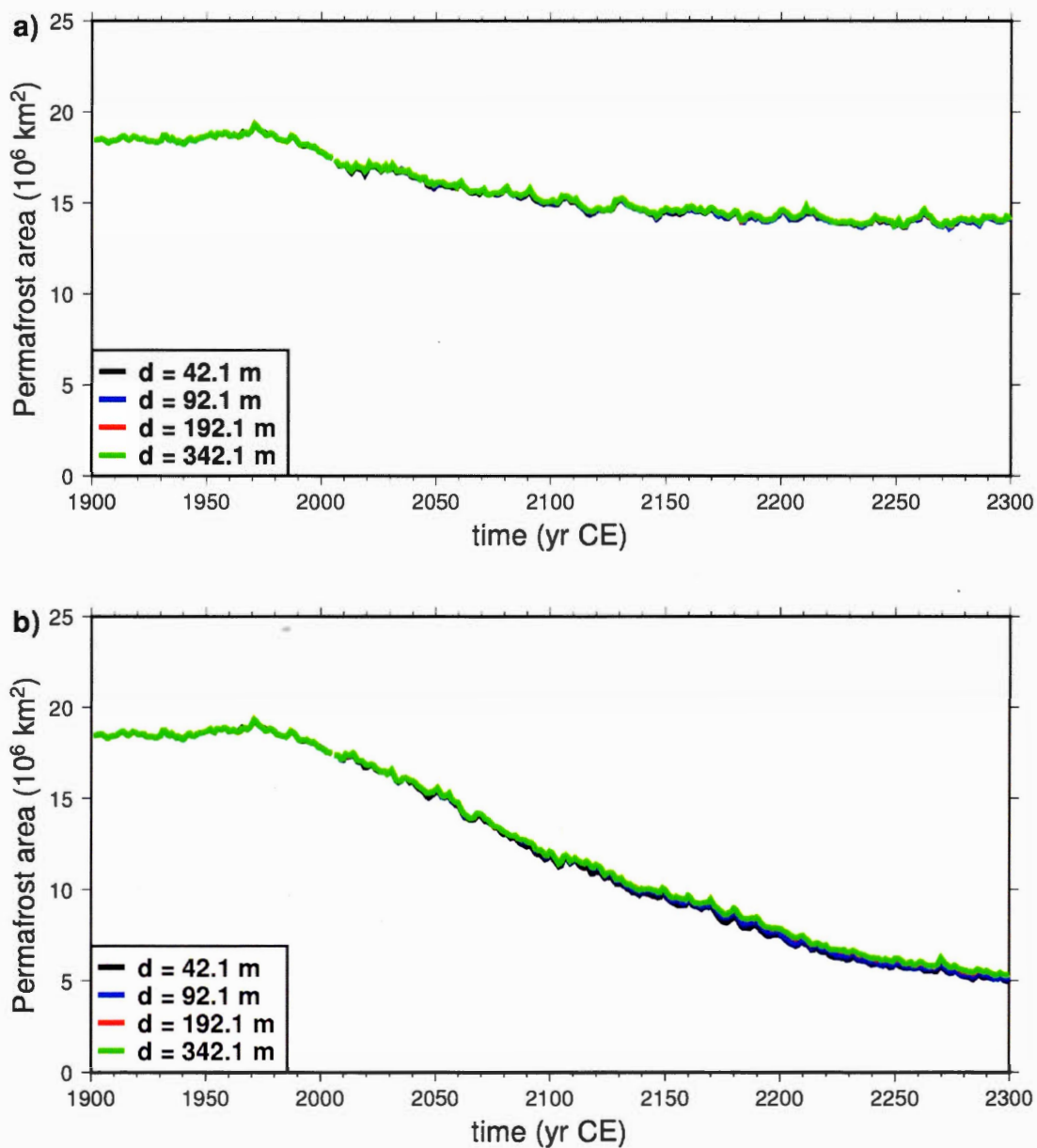


Figure 2.07: Northern Hemisphere near-surface permafrost area as function of time. Model versions with bottom boundary depth at 42.1 m (black), 92.1 m (blue) 192.1 m (red) and 342.1 m (green). a) Simulations forced with CRUNCEP + RCP 4.5 data. b) Simulations forced with CRUNCEP + RCP 8.5 data.

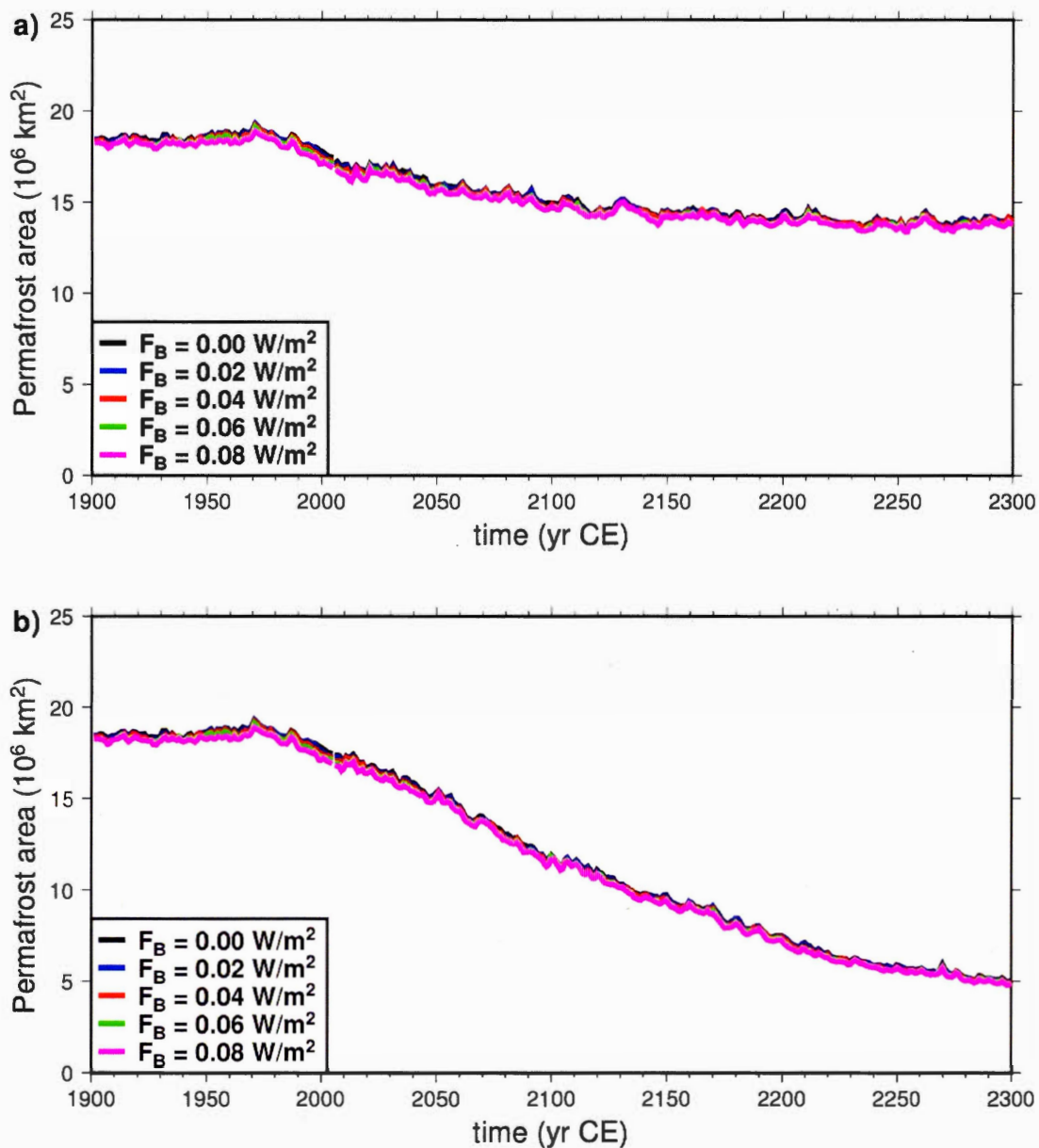


Figure 2.08: Northern Hemisphere near-surface permafrost area as function of time. Models using different heat flux as bottom boundary. a) Simulations forced with CRUNCEP + RCP 4.5 data. b) Simulations forced with CRUNCEP + RCP 8.5 data.

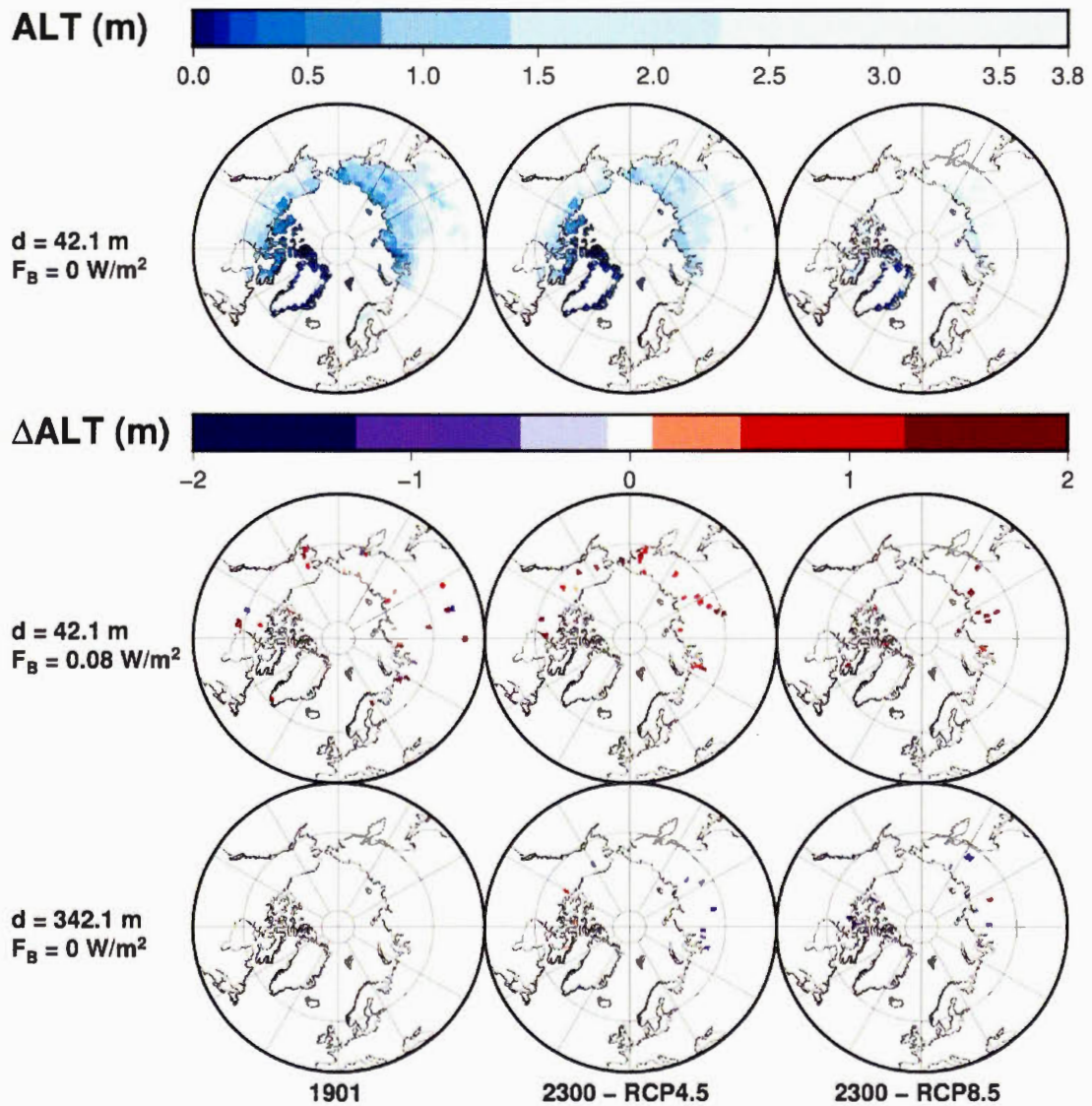


Figure 2.09: Active Layer Thickness for the unmodified model (top), and differences to the original model at each time frame for the modified model with  $F_B = 80$  mW m<sup>-2</sup> (middle) and the modified model with  $d = 342.1$  m (bottom). Time frames at 1901 CE and 2300 CE for the scenarios RCP 4.5 and RCP 8.5.

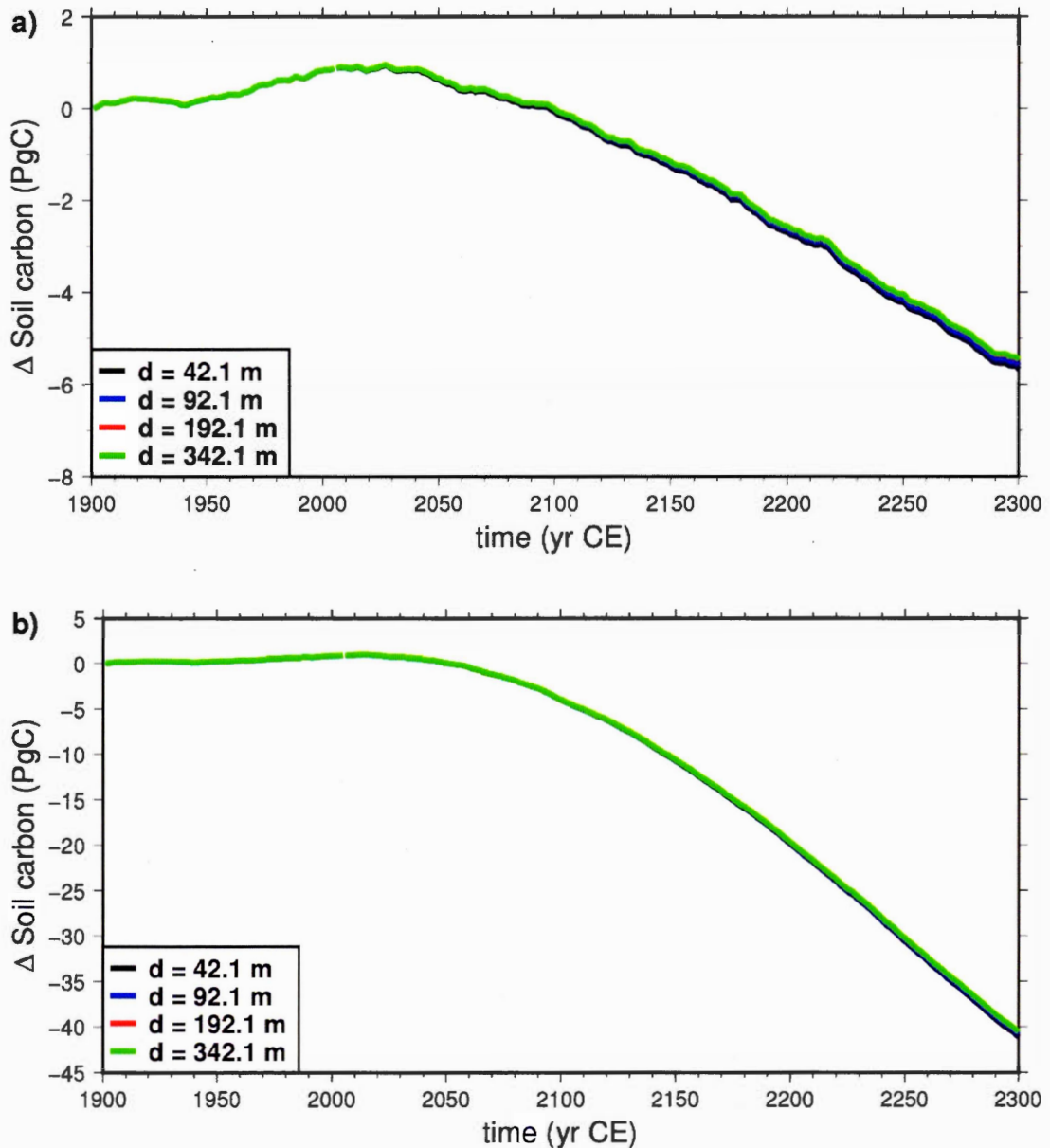


Figure 2.10: Evolution of soil carbon pool in the Northern Hemisphere permafrost region, compared to the size for the original model at 1901 CE. Models with varying bottom boundary depth. a) Simulations forced with CRUNCEP + RCP 4.5 data. b) Simulations forced with CRUNCEP + RCP 8.5 data. Note the different vertical scale in panel a and b.

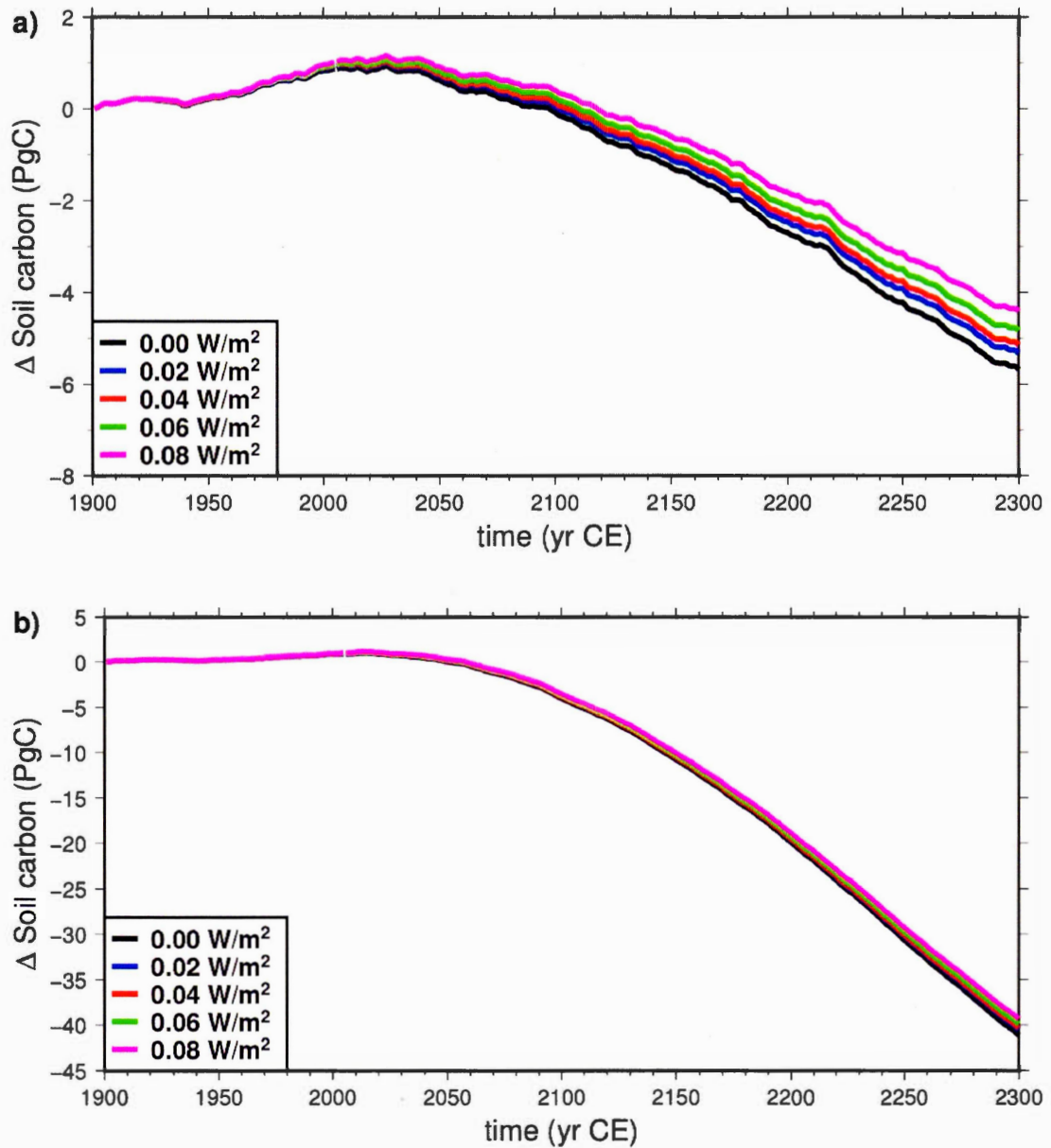


Figure 2.11: Evolution of soil carbon pool in the Northern Hemisphere permafrost region, compared to the size for the original model at 1901 CE. Models with varying basal heat flux. a) Simulations forced with CRUNCEP + RCP 4.5 data. b) Simulations forced with CRUNCEP + RCP 8.5 data. Note different vertical scale in panel a and b.

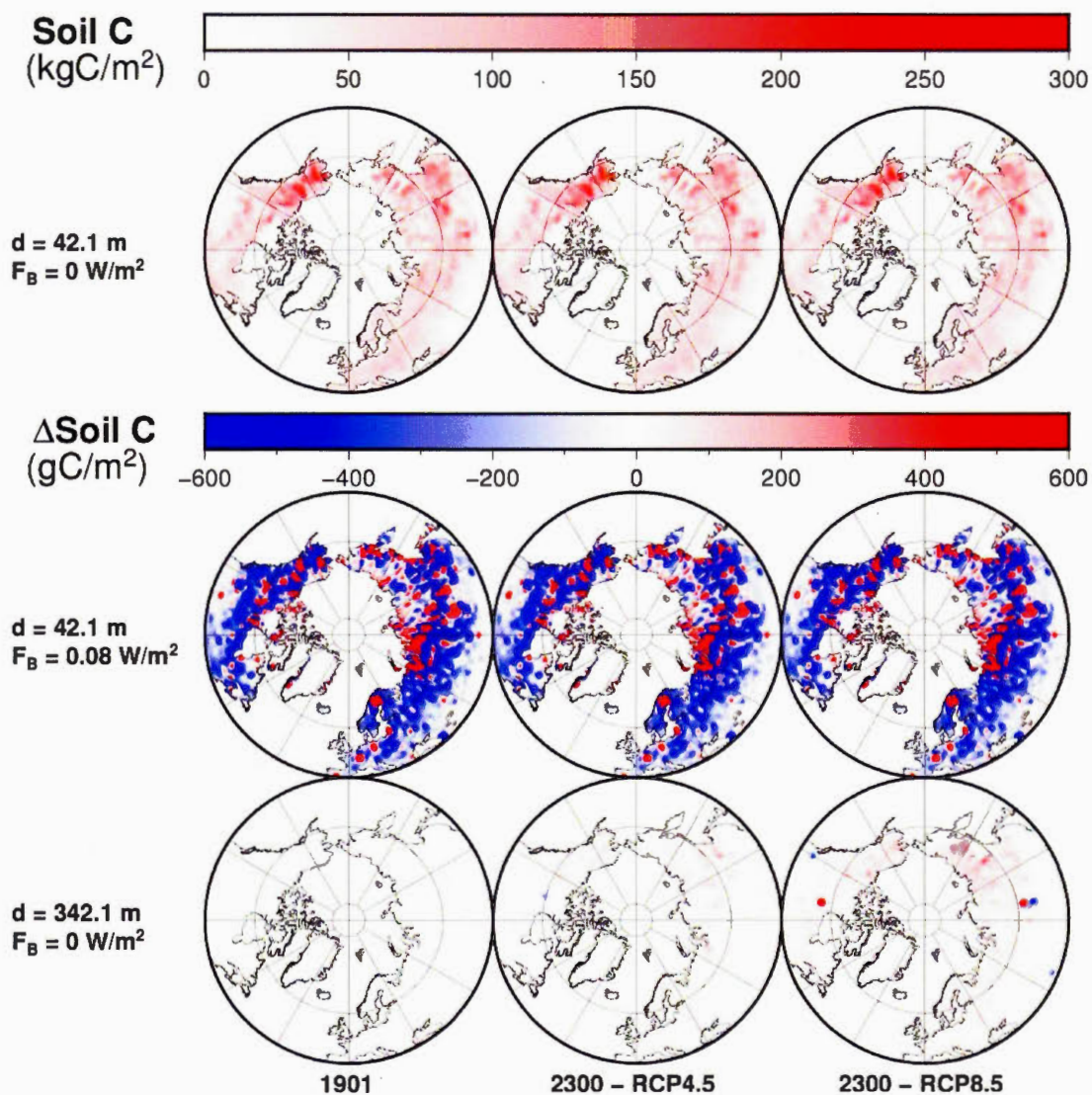


Figure 2.12: Distribution of soil carbon for the original model (top) in  $kgC/m^2$ , and differences to the original model at each time frame for the modified model with  $F_B = 0.08$   $W\ m^{-2}$  (middle) and the modified model with  $d = 342.1$  m (bottom), in  $gC/m^2$ . Time frames at 1901 CE and 2300 CE for the scenarios RCP 4.5 and RCP 8.5.

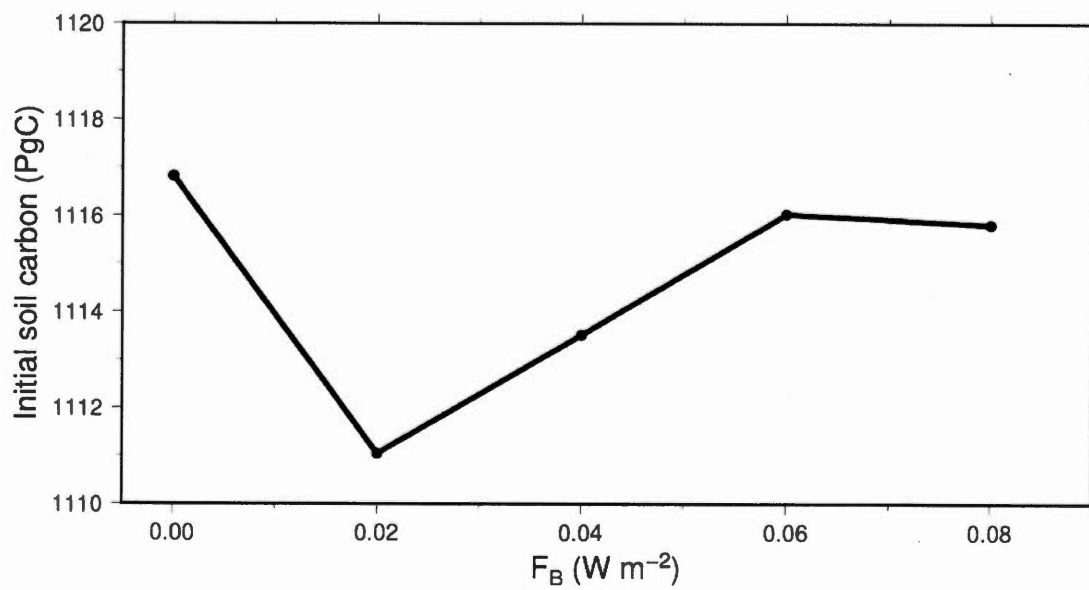


Figure 2.13: Mean size of the soil carbon pool in the Northern Hemisphere permafrost region between 1901-1910, as function of basal heat flux.

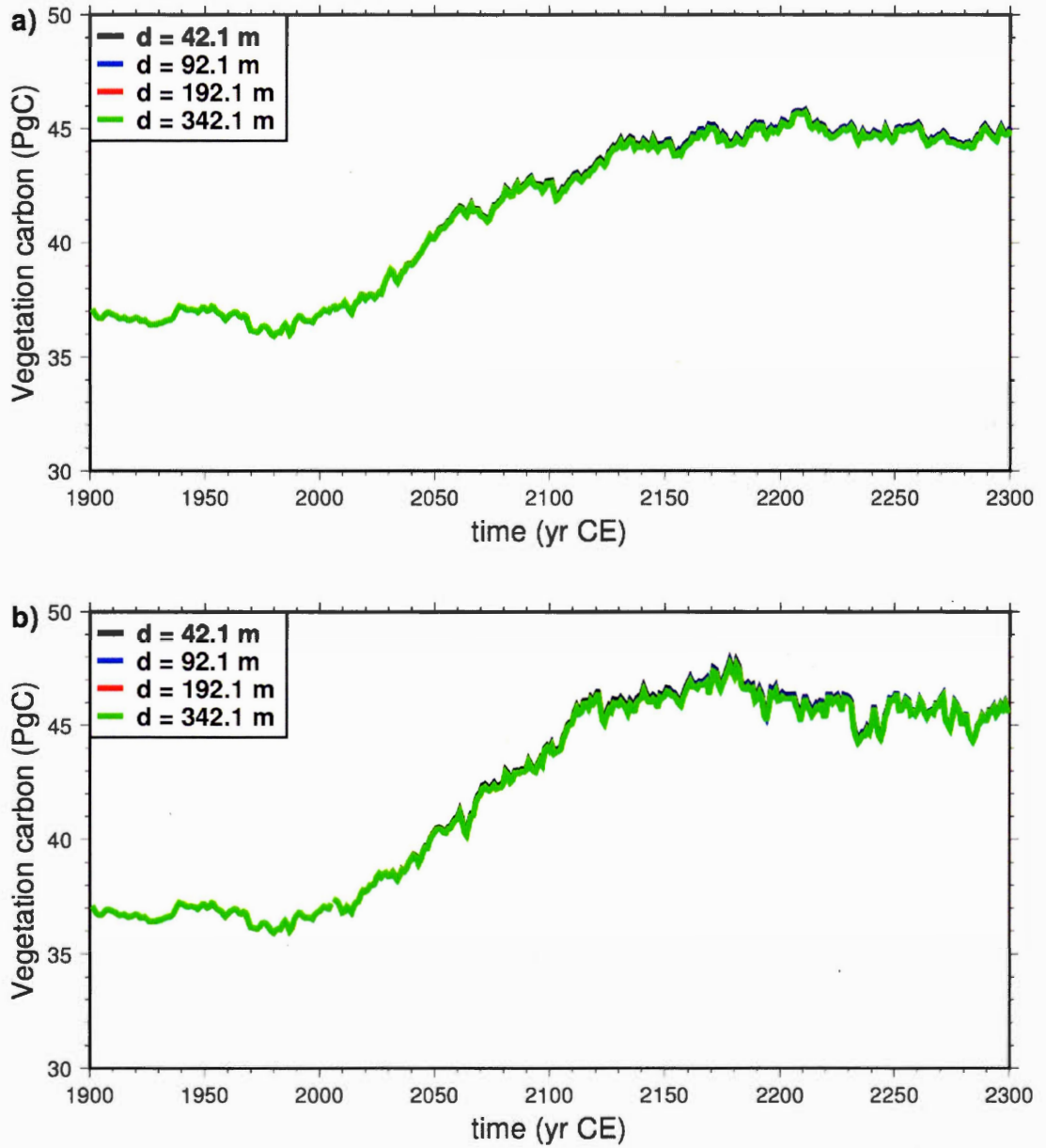


Figure 2.14: Vegetation carbon pool in the Northern Hemisphere permafrost region. Models with varying bottom boundary depth. b) Simulations forced with CRUNCEP + RCP 8.5 data.

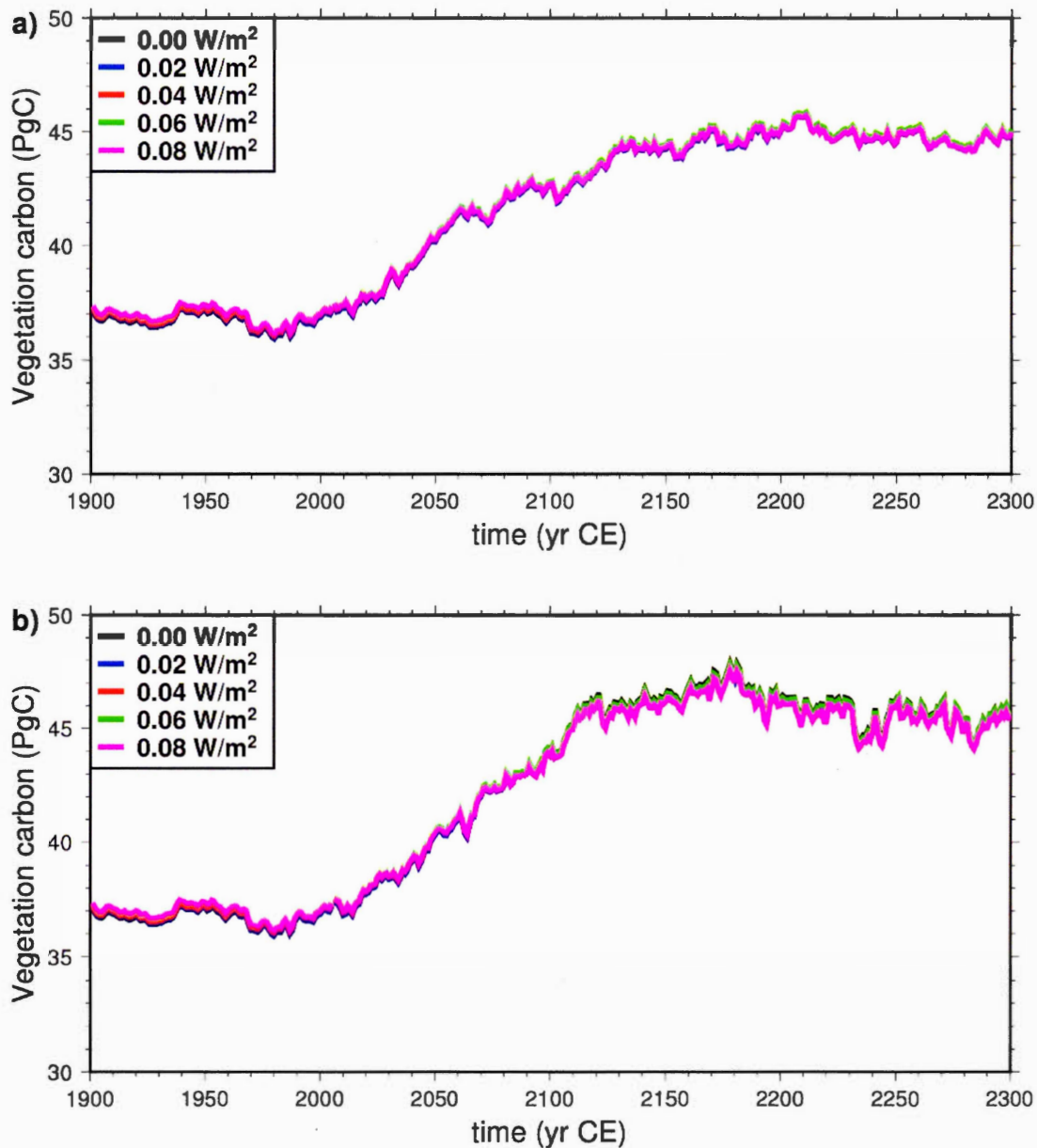


Figure 2.15: Vegetation carbon pool in the Northern Hemisphere permafrost region. Models with varying basal heat flux. a) Simulations forced with CRUNCEP + RCP 4.5 data. b) Simulations forced with CRUNCEP + RCP 8.5 data.

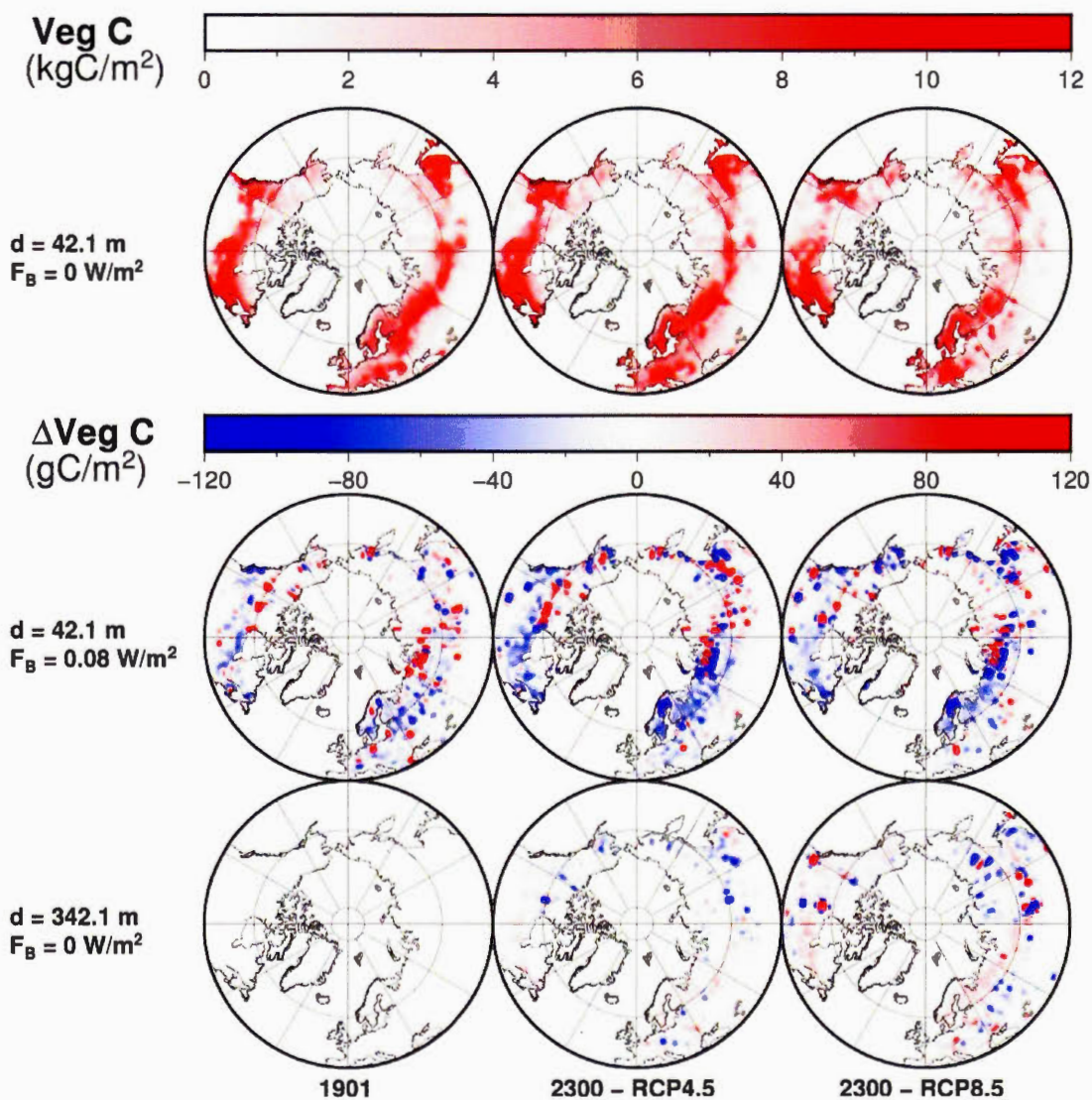


Figure 2.16: Distribution of vegetation carbon for the original model (top), and differences to the original model at each time frame for the modified model with  $F_B = 0.08 \text{ W m}^{-2}$  (middle) and the modified model with  $d = 342.1 \text{ m}$  (bottom). Time frames at 1901 CE and 2300 CE for the scenarios RCP 4.5 and RCP 8.5.

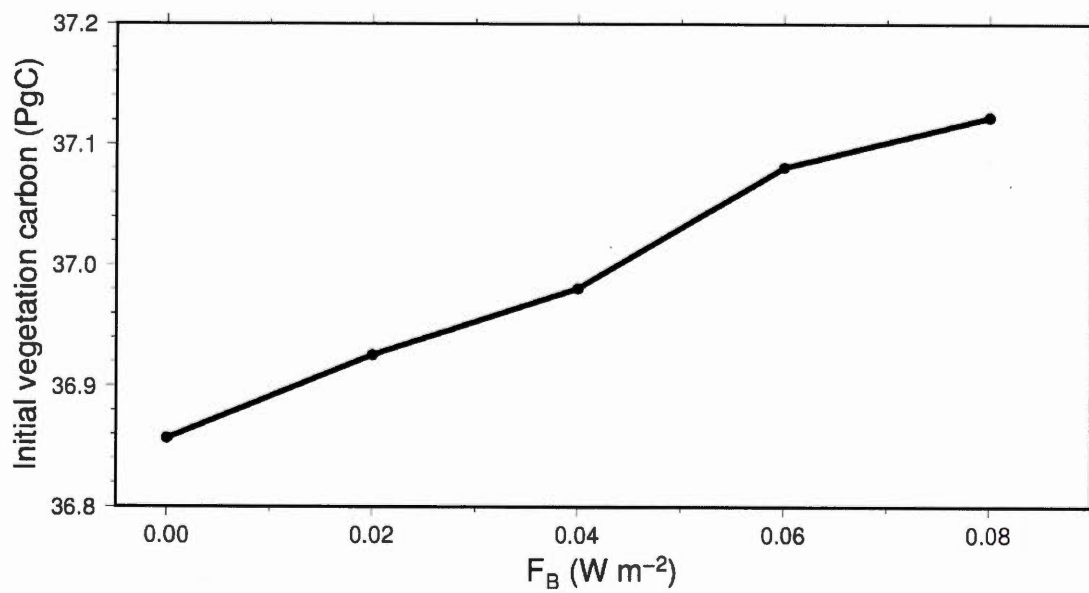


Figure 2.17: Mean size between 1901-1910 of the vegetation carbon pool in the Northern Hemisphere permafrost region, for models of different bottom heat flux.

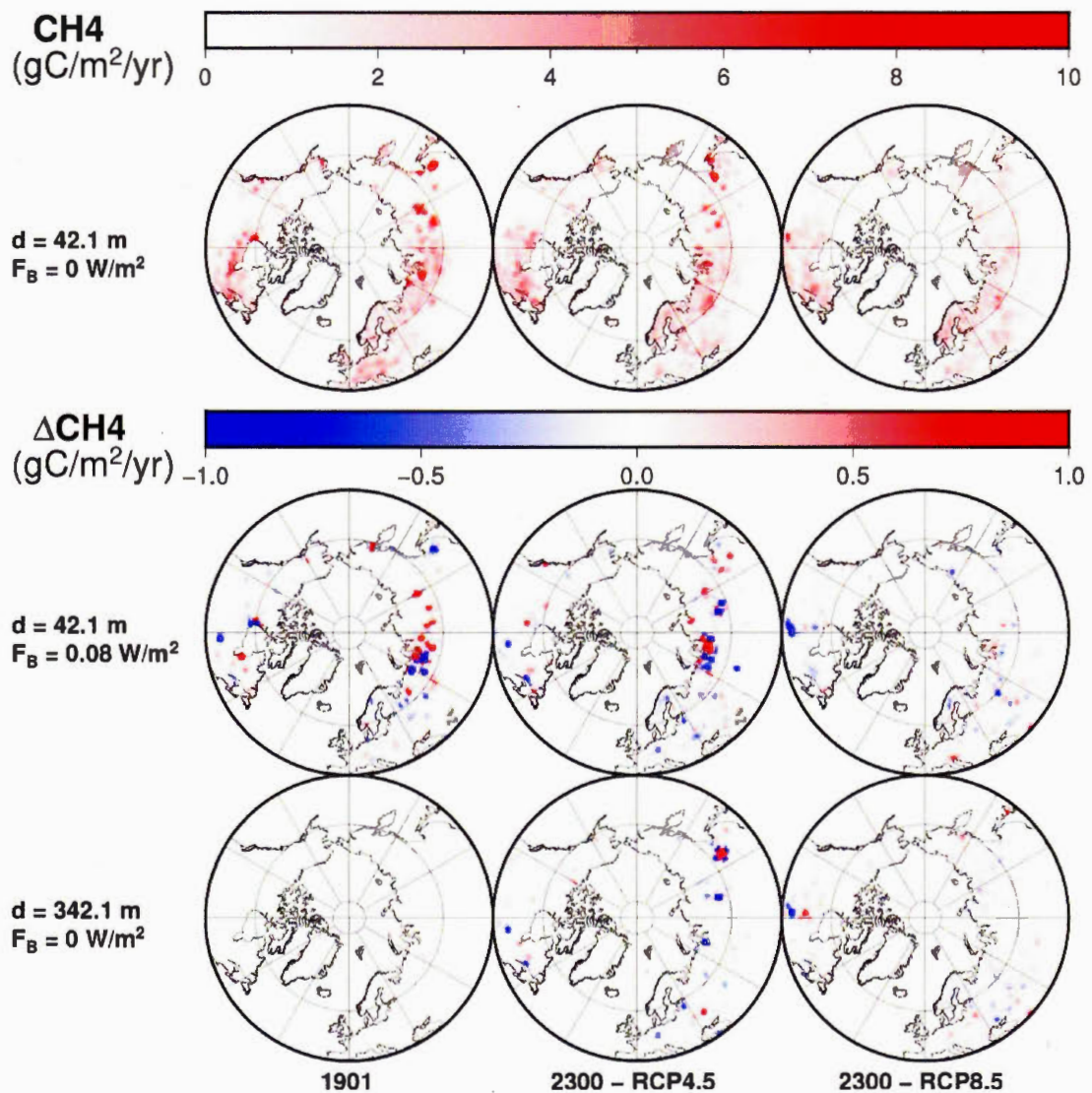


Figure 2.18: Distribution of methane yearly production for the original model (top), and differences to the original model at each time frame for the modified model with  $F_B = 0.08$  W m<sup>-2</sup> (middle) and the modified model with  $d = 342.1$  m (bottom). Time frames at 1901 CE and 2300 CE for the scenarios RCP 4.5 and RCP 8.5.

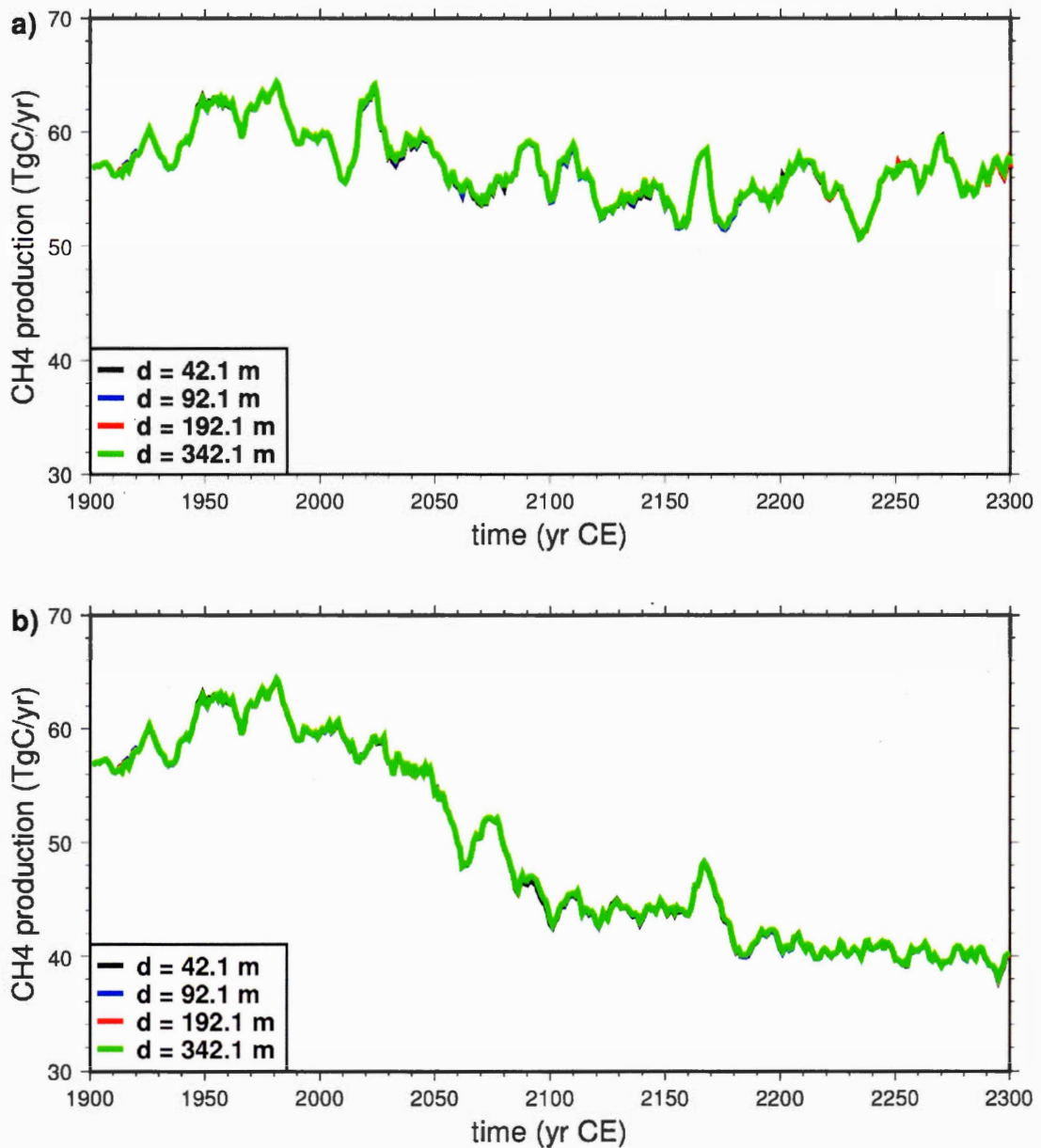


Figure 2.19: Global yearly methane production as function of time, moving average of 10 years. Models with varying bottom boundary depth. a) Simulations forced with CRUNCEP + RCP 4.5 data. b) Simulations forced with CRUNCEP + RCP 8.5 data.

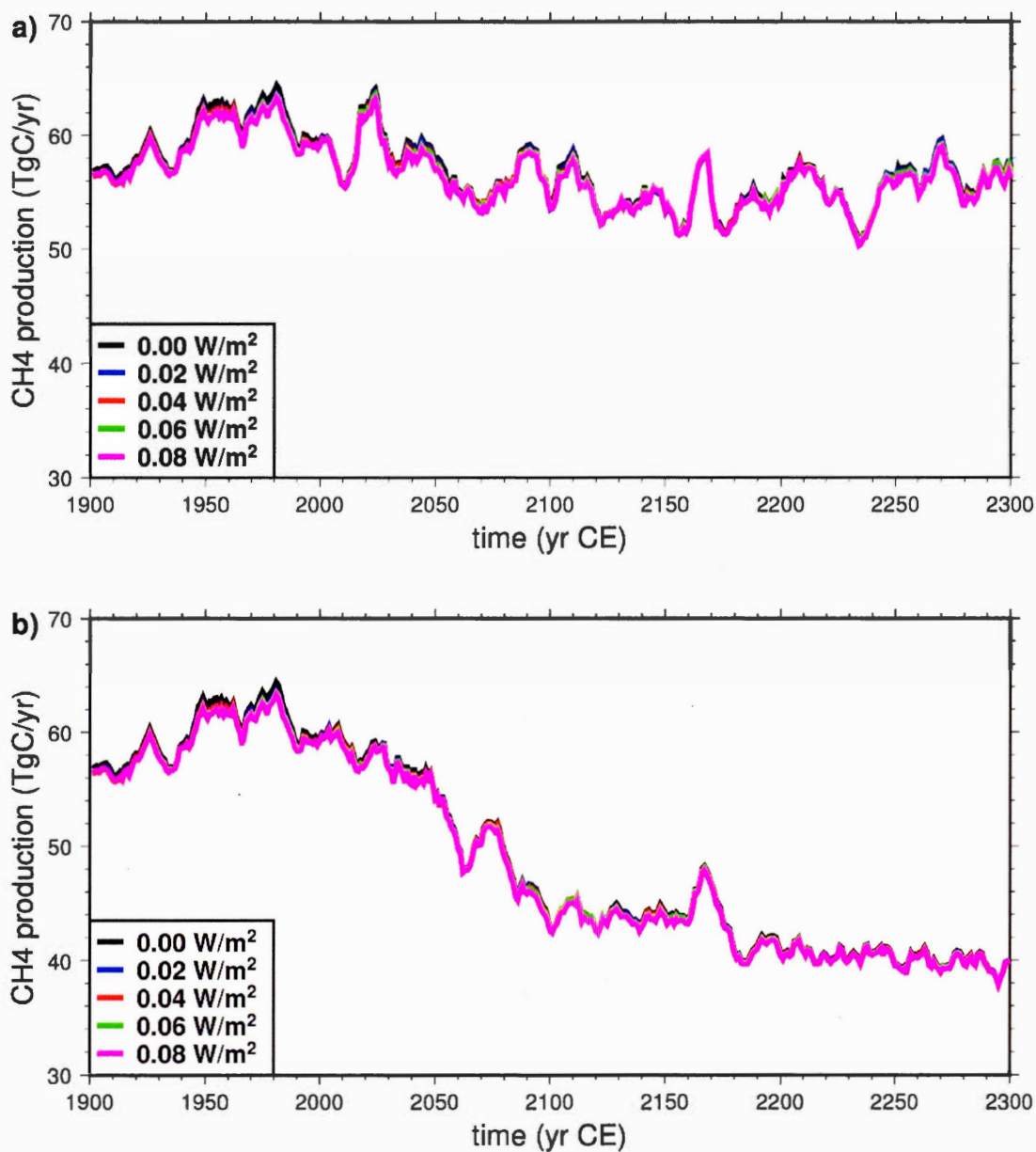


Figure 2.20: Global yearly methane production as function of time, moving average of 10 years. Models with varying basal heat flux. a) Simulations forced with CRUNCEP + RCP 4.5 data. b) Simulations forced with CRUNCEP + RCP 8.5 data.

Table 2.1: Areal extent of intermediate-depth permafrost at 1901 CE, 2000 CE and 2300 CE for the RCP 4.5 and RCP 8.5 scenarios.

Subsurface parameters	CRU-NCEP			RCP 4.5		RCP 8.5	
	PF area 1901 ( $\times 10^6 \text{ km}^2$ )	PF area 2000 ( $\times 10^6 \text{ km}^2$ )	PF area 2300 ( $\times 10^6 \text{ km}^2$ )	Fraction PF lost 1901-2300 (%)	Fraction PF lost 1901-2300 (%)	Fraction PF lost 1901-2300 (%)	Fraction PF lost 1901-2300 (%)
$d$ (m)	$F_B$ ( $\text{W m}^{-2}$ )						
42.1	0	20.43	19.33	15.49	24.18	5.58	72.68
42.1	0.08	19.85	18.65	14.72	25.84	5.11	74.25
342.1	0	20.43	20.21	18.84	7.78	17.69	13.41

Table 2.2: Areal extent of near-surface permafrost at 1901 CE, 2000 CE and 2300 CE for the RCP 4.5 and RCP 8.5 scenarios.

Subsurface parameters		CRU-NCEP		RCP 4.5		RCP 8.5	
$d$ (m)	$F_B$ ( $\text{W m}^{-2}$ )	PF area 1901 ( $\times 10^6 \text{ km}^2$ )	PF area 2000 ( $\times 10^6 \text{ km}^2$ )	PF area 2300 ( $\times 10^6 \text{ km}^2$ )	Fraction PF lost 1901-2300 (%)	PF area 2300 ( $\times 10^6 \text{ km}^2$ )	Fraction PF lost 1901-2300 (%)
42.1	0	18.45	17.8	14.17	23.17	5.07	72.49
42.1	0.08	18.25	17.09	13.80	24.40	4.90	73.15
342.1	0	18.45	17.5	14.25	22.75	5.34	71.07

## CHAPTER III

### CONSTRAINTS ON GLACIER FLOW FROM TEMPERATURE-DEPTH PROFILES IN THE ICE. APPLICATION TO EPICA DOME C.

#### 3.1 Abstract

A one-dimensional (1-D) ice flow and heat conduction model is used to calculate the temperature and heat flux profiles in the ice and to constrain the parameters characterizing the ice flow and the thermal boundary conditions at the Dome C drilling site in East Antarctica. We use the reconstructions of ice accumulation, glacier height and air surface temperature histories as boundary conditions to calculate the ice temperature profile. The temperature profile also depends on a set of poorly known parameters, the sliding, the Glen's exponent, the flux function parameter, basal heat flux, and air-ice surfaces temperature coupling. We use Monte Carlo methods to search the parameters' space of the model, compare the model output with the temperature data, and find probability distributions for the unknown parameters. We determined the basal heat flux  $q_b = 51.1 \pm 1.4(2\sigma)$  mW m<sup>-2</sup>, higher than the apparent value. We found a value for the Glen's exponent of  $n = 1.91 + 0.11(2\sigma)$  and an air-ice temperature coupling of  $0.36 \pm 1.2(2\sigma)$  K. We could not determine the sliding ratio  $s$  and the flux function parameter  $p$  because of their small effect on the thermal profile, but we could constrain maximum values of  $s < 0.4$  and  $p < 7.4$  with a  $2\sigma$  confidence. Our study confirms that the heat flux is low and does not destabilize the ice sheet in

East Antarctica.

### 3.2 Introduction

Climate change, as a consequence of human activities, has become a focus of attention of the scientific community. Climate change can be seen as the consequence of an imbalance between the emission and absorption of energy by the planet. Such global energy imbalance generates exchanges of energy among climate subsystems as the Earth follows a path towards a new equilibrium. The cryosphere, and in particular the polar ice sheets, play a key role in the climate system, influencing ocean temperatures, sea level, thermohaline circulation and global albedo, responding to the energy imbalance on time scales ranging from decades to millennia (Clark et al., 1999). Therefore, understanding ice sheet dynamics, controlled by basal heat flux (Oppenheimer, 1998), is of major importance for modelling future climate change.

Ice cores from Antarctica and Greenland provide reliable proxy records for the reconstruction of past climate, covering hundreds of thousands of years into the past (Parrenin et al., 2007a; Jouzel et al., 2007). In Greenland, the European Greenland Ice-core Project (GRIP) provides data on the last 110 ka (Johnsen et al., 1995; Dahl-Jensen et al., 1998). In Antarctica, deep ice cores from Dome Fuji, EPICA Dome C (EDC), Vostok, or EPICA Dronning Maud Land (EDML), allow reconstructions of past climate to 340 ka, 800 ka, 420 ka, and 150 ka, respectively (Watanabe et al., 1999; Augustin et al., 2004; Jouzel et al., 2007; Petit et al., 1999; Ruth et al., 2007).

The analysis of air bubbles trapped in the ice when it was formed allows for the reconstruction of past atmospheric concentrations of CO<sub>2</sub>, CH<sub>4</sub> and N<sub>2</sub>O (e.g. Barnola et al., 1987; Spahni et al., 2005). Past temperatures can be estimated from the stable oxygen isotope ratios ( $\delta^{18}\text{O}$ ) in air bubbles and deuterium in the

ice molecules (Pol et al., 2010). The deuterium content in the ice is also correlated to the snow accumulation rate, which allows its reconstruction (Jouzel et al., 2007; Pol et al., 2010).

The interactions of the ice sheet with the climate system and the solid earth are not straightforward. Ice sheets are complex systems with variable dynamics and structure, which depend on the thermal and mechanical basal boundary conditions (the basal heat flux and the sliding ratio of the ice sheet) (Marshall, 2005), and surface conditions (snow accumulation rates and atmospheric temperatures). Analysis of age versus depth of the ice cores provides some insight on ice flow mechanics, through the determination of the ice thinning function, the vertical velocity, as well as the basal melting rate and the sliding ratio (Parrenin et al., 2004, 2007b). These age-depth profiles also provide some constraints on the basal heat flux which is an essential factor affecting the dynamics of ice sheet models (Fisher et al., 2015).

High resolution temperature profiles measured in drill holes retain a record of the time dependent boundary conditions and ice sheet dynamics. These temperature-depth profiles provide another means to determine basal heat flux. In this paper, we use a numerical, one-dimensional (vertical) advective-conductive model which includes the key parameters driving ice-sheet dynamics. The model is forced by the local histories of atmospheric temperatures, snow precipitation and ice thickness, to determine temperature profiles for the ice-sheet. An additional constraint is the surface velocity that comes from geodetic surveys (Vittuari et al., 2004). We then use a Monte Carlo inversion scheme to find sets of values of the parameters that fit the observed temperature profile, determine their probability distributions and their most likely values.

We have applied this method to the ice core drilled at EPICA Dome C in Antarc-

tica, one of the longest ice core records presently available. The temperature profile through the entire thickness of the ice-sheet was measured in the drill hole (Pol et al., 2010). The forcing is provided by the precipitation and atmospheric conditions for the past 800 ka that have been reconstructed by analyzing the ice core extracted from the drill hole (Jouzel et al., 2007). The method used in the present study could be applied to any ice temperature profile extending through most of the ice-sheet thickness and provide independent constraints for ice dynamics parameters.

### 3.3 Basic assumptions and equations

The drilling at the Dome C site ( $75^{\circ}6'6.35''$  S,  $123^{\circ}23'42.76''$  E), with an ice thickness of  $3273 \pm 5$  m (Tabacco et al., 1998), was stopped  $\sim 15$  m above bedrock, allowing the measurement of the temperature profile through the entire glacier. The temperature profile (Fig. 3.01) is determined by both the thermal boundary conditions and the ice dynamics which controls heat transport by advection and produces shear heating.

We follow the theory of ice sheet dynamics of Paterson (1994). The ice sheet grows by accumulation of snow at the top, increasing its gravitational potential energy that drives the flow of the ice sheet toward the ocean. Due to basal friction, the velocity of the flow is maximum at the top of the ice sheet and decreases with depth, consequently thinning the ice layers and reducing the height of the glacier. The ice surface is in contact with the air above, absorbing heat from the ice sheet. As heat flows into the glacier from the underlying bedrock, the temperature gradient in the ice is positive downward, which could bring the base to melt. Meltwater reduces basal friction and allows the ice sheet to slide over the bedrock, a movement defined through the sliding parameter  $s$ , the ratio between the ice horizontal velocity at the base and at the top of the ice (Fig. 3.02).

We have developed a forward model to simulate the thermal processes that take place in the ice sheet, including both heat diffusion and advection by ice movement, and therefore defined as an advective-conductive model. This model calculates a temperature profile that is determined by heat conduction, the flow dynamics of the ice sheet, and their boundary conditions.

Ice sheet dynamics is described through the field equations, i.e. the conservation of mass and momentum. The mass conservation equation for a material of density  $\rho$  is:

$$\frac{\partial \rho}{\partial t} + \vec{\nabla} \cdot (\rho \vec{u}) = 0, \quad (3.1)$$

where  $\vec{u}$  is the velocity of the ice.

For an incompressible material ( $\frac{D\rho}{Dt} = 0$ ), a reasonable assumption for ice, the mass conservation equation reduces to:

$$\vec{\nabla} \cdot \vec{u} = 0. \quad (3.2)$$

For steady state flow (without acceleration), momentum conservation requires the balance between the body forces acting on the ice volume, i.e., weight  $\rho g$  (where  $g$  is the acceleration of gravity), and the internal forces described by the stress tensor  $\bar{\tau}$ :

$$\vec{\nabla} \bar{\tau} + \rho \vec{g} = 0. \quad (3.3)$$

For ice, the constitutive equation has been established by experimental work (Glen, 1955) and corresponds to non linear viscous rheology. The relationship between the strain rate  $\dot{\epsilon}$  and the shear stress  $\tau$  is given by an empirical law known as Glen's law:

$$\dot{\epsilon} = A\tau^n, \quad (3.4)$$

where  $n$  is Glen's exponent and  $A$  is a temperature-dependent empirical quantity (Paterson, 1994).

At the local scale it is possible to model ice flow in two dimensions by choosing the horizontal axis in the direction of ice flow. In addition, because the size of the ice sheet is much greater than its thickness and variations in crustal heat flux occur on a scale of tens of kilometers (Jaupart & Mareschal, 2015), we can assume that horizontal temperature gradients are negligible and therefore conductive heat flow  $q$  ( $\text{W m}^{-2}$ ) is vertical and given by Fourier's law in one dimension:

$$q = -\lambda \frac{\partial T}{\partial z}, \quad (3.5)$$

where  $\lambda$  ( $\text{W m}^{-1} \text{K}^{-1}$ ) is the thermal conductivity and  $z$  is the vertical coordinate, defined positive upwards with the origin at the base of the ice.

The one dimensional heat equation is (Carslaw & Jaeger, 1959):

$$\frac{\partial T}{\partial t} = \kappa \frac{\partial^2 T}{\partial z^2} - u_z \frac{\partial T}{\partial z} + \frac{\Omega}{\rho c_p}, \quad (3.6)$$

where  $\kappa = \frac{\lambda}{\rho c_p}$  ( $\text{m}^2 \text{s}^{-1}$ ) is the thermal diffusivity,  $\rho = 916.2 \text{ kg m}^{-3}$  is the ice density,  $c_p$  ( $\text{J kg}^{-1} \text{K}^{-1}$ ) is the specific heat, and  $u_z$  ( $\text{m yr}^{-1}$ ) is the vertical component of the ice velocity. The function  $\Omega$  ( $\mu\text{W m}^{-3}$ ) is the rate of heat production per unit volume, due to shear heating. Absorption or release of latent heat at the base is not included in this term but introduced in the basal heat flux boundary condition.

The conductive heat flux profile obtained for Dome C (Fig. 3.01) can be used to estimate the basal heat flux. From a linear regression of the lowermost 300 m of the heat flux profile, we obtain an apparent basal heat flux of  $q_{b,app} = 49.4 \pm 1.1 \text{ mW m}^{-2}$ . However, internal heating caused by shear deformation affects the profile and its effect must be taken into account. Therefore, we consider  $q_b$  as a free parameter, whose probability distribution is to be evaluated.

### 3.4 Boundaries

The heat equation requires two boundary conditions. At the top of the ice column, the temperature is the Ice Surface Temperature (IST). It is obtained directly by assuming a constant offset (see subsection 3.4.3) from the Surface Air Temperature (SAT) history, which is known from the analysis of the deuterium content of the ice core (Pol et al., 2010), and is in excellent agreement with the reconstruction from  $\delta^{18}O$  record (Jouzel et al., 2007). At the bottom, the contact between the ice column and the bedrock, the boundary condition is a fixed and constant basal heat flux  $q_b$ . If the basal temperature reaches the melting point, and basal heat flux is enough to maintain it, the excess heat flux is absorbed as latent heat (see subsection 3.5.1), and the melting temperature becomes the effective bottom boundary condition.

#### 3.4.1 Ice thickness history

Ice thickness  $H$  varied significantly (3100-3350 m) during the past 800 kyr that we model. We used a prescribed history of ice thickness, obtained from the simple linear perturbation model developed by Parrenin et al. (2007b). This is a conceptual 1-D model of ice thickness variations, whose parameters are tuned at each specific site to fit the results of a larger and complex 3-D thermo-mechanical model of the Antarctic ice sheet (Ritz et al., 2001).

$$a - \frac{\partial H}{\partial t} = k + k_H H + k_S S, \quad (3.7)$$

where  $a$  ( $\text{m yr}^{-1}$ ) is the accumulation,  $S$  is the surface elevation  $S = B + H$  and  $B$  is the bedrock elevation:

$$\frac{\partial B}{\partial t} = \frac{(B_0 - H/k_B) - B}{\tau_B}, \quad (3.8)$$

where  $B_0 = 915.5$  m corresponds to bedrock elevation without isostatic effect and

$k = 0.3917 \text{ m yr}^{-1}$ ,  $k_H = 6.114 \times 10^{-4} \text{ yr}^{-1}$ ,  $k_S = -7.018 \times 10^{-4} \text{ yr}^{-1}$ ,  $k_B = 3.8$  and  $\tau_B = 3000 \text{ yr}$  are parameters tuned to fit the results of the 3-D model at Dome C.

As noted by Parrenin, the formulation of this simple model of elevation does not guarantee that the present-day ice thickness is compatible with that measured at Dome C, because it depends on the accumulation scenario used. For this reason he took only the relative variations of ice thickness  $\Delta H(t) = H(t) - H(t = 0)$  from this model, using the measured present-day ice thickness to obtain the history of ice thickness. This is also the case for our application of the Parrenin model, as we obtain relative variations of ice thickness that are consistent with those obtained by Parrenin et al. (2007b), but the ice thickness being consistently lower ( $\sim 350 \text{ m}$ ). Therefore, we have used the relative variations of ice thickness defined by the Parrenin model, using as reference the present ice thickness at Dome C  $H_0 = 3266 \text{ m}$  (Fig. 3.03). This history of ice thickness was then used to calculate  $\frac{\partial H}{\partial t}$  dynamically, so that  $H$  follows the prescribed history.

### 3.4.2 Surface accumulation and SAT histories

The accumulation rate  $a$  ( $\text{m yr}^{-1}$ ), measured in ice-equivalent units, and the SAT are determined from deuterium content  $\Delta\delta D$  (Jouzel, 2007; Pol et al., 2010):

$$a = a_0 \exp(\beta \Delta\delta D_{smo}), \quad (3.9)$$

$$\text{SAT} = T_0 + \alpha \Delta\delta D_{cor}, \quad (3.10)$$

where  $a_0$  and  $T_0$  are the accumulation rate and the surface temperature for a reference deuterium content of  $-396.5\text{‰}$ .  $\Delta\delta D_{cor}$  is the corrected deviation (Lliboutry, 1979) from the current deuterium content of the ice.  $\Delta\delta D_{smo}$  is a 50-year smoothed version of  $\Delta\delta D_{cor}$  because the accumulation rate is only supposed to be related to the deuterium content over a certain time interval (Parrenin et al.,

2007b).

We use the values  $\alpha = 1/6.04K/\text{‰}$  and  $T_0 = 215.84$  K for Dome C of Parrenin et al. (2007b), who determined the values  $a_0 = 2.84 \pm 0.03$  cm yr<sup>-1</sup> and  $\beta = 0.0156 \pm 0.0012$  by inverse methods. The accumulation rate history and SAT history that result from these values are shown in Fig. 3.04 and in Fig. 3.05, respectively.

### 3.4.3 Temperature offset and snow-firn cover

Accumulation at the surface of the ice column is measured in ice equivalent units, but precipitations are first deposited in the form of snow. Before being transformed in ice, snow passes through an intermediate phase called firn (Arnaud et al., 2000; Goujon et al., 2003). These processes are driven mainly by the atmospheric temperatures and the accumulation rates. The density of snow/firn increases gradually with depth, until it becomes ice. We estimated the average firn density from Dome C data (Arnaud et al., 2000) and modeled the upper 80m as firn, with a uniform density 75% that of ice.

The temperature signal that propagates into the ice column is the IST, a filtered version of the SAT. Measurements at Vostok station over the last 50 years (Vostok, 2016) show that the IST is  $\approx 5$  K warmer than the SAT in summer and  $\approx -2.5$  K colder in winter. We assume the mean temperature offset  $T_{\text{offset}}$  (K) to be time-independent. Periodic temperature signals at the surface are filtered out as they propagate through the subsurface, at a depth of 80 m only the average surface temperature can be appreciated. This makes acceptable the approximation of the temperature offset as time-independent, because only the upper firn layer would be affected, and this layer is not taken into account when comparing present-day profiles.

$$T_{\text{offset}} = \text{IST} - \text{SAT} . \quad (3.11)$$

Because imprecisions on the estimate of the snow cover of the ice column make  $T_{\text{offset}}$  difficult to determine, we have considered it as a free parameter restricted within a range  $[-2.5\text{K}, 5\text{K}]$ . The unrealistic assumption of the upper layer as a uniform firn layer, as well as errors in the estimation of the thickness and density of this layer, will increase the error of this parameter, but it does not affect other parameters.

### 3.5 Methodology

#### 3.5.1 Basal melting

The forward model calculates dynamically the basal melting rate. When the basal ice layer reaches melting temperature  $T_m$  (K), the extra incoming energy is used to calculate melting rate  $m$  ( $\text{m yr}^{-1}$ ). The melting temperature depends on the pressure as follows:

$$T_m = 273.15 - \beta_{CC}P, \quad (3.12)$$

where  $\beta_{CC} = 7.42 \times 10^{-8} \text{ K Pa}^{-1}$  is the Clausius-Clapeyron slope and  $P$  (Pa) is the pressure at the glacier base.

When the basal temperature reaches  $T_m$ , the excess heat flux (incoming minus outgoing) at the base  $\Delta q_b$  ( $\text{mW m}^{-2}$ ) is absorbed as latent heat of fusion by the ice, and the melting rate  $m$  is calculated as:

$$m = \frac{\Delta q_b}{\rho L_f}, \quad (3.13)$$

where  $L_f = 3.337 \times 10^6 \text{ J kg}^{-1}$  is the latent heat of ice. If  $\Delta q_b < 0$ , the basal temperature drops below the melting point, and melting stops.

The melted ice is subtracted at the bottom of the ice column reducing its thickness. The effect of water on sliding is neglected.

### 3.5.2 Glacier movement

We calculated the vertical movement in the glacier of the ice with the 1-D ice flow model used in Parrenin et al. (2007b), which gives vertical velocity  $u_z$  (m yr<sup>-1</sup>) as:

$$u_z[z] = - \left( m + \left( a - \frac{\partial H}{\partial t} - m \right) \omega[\zeta] \right), \quad (3.14)$$

where  $a$  (m yr<sup>-1</sup>) and  $m$  (m yr<sup>-1</sup>) are the accumulation (at the surface) and the melting (at the base) rates respectively, and  $H$  (m) is the height of the glacier, expressed as ice equivalent. The flux shape function  $\omega[\zeta]$  depends on the non-dimensional vertical coordinate  $\zeta = z/H$  and includes contributions of the basal sliding term and the shear deformation term (Parrenin et al., 2006):

$$\omega[\zeta] = s\zeta + (1 - s)\omega_D[\zeta], \quad (3.15)$$

where  $s$  is the sliding ratio (varying between 0 and 1) and  $\omega_D[\zeta]$  is the vertical profile of deformation (Lliboutry, 1979), given by:

$$\omega_D[\zeta] = 1 - \frac{p+2}{p+1}(1-\zeta) + \frac{1}{p+1}(1-\zeta)^{p+2}, \quad (3.16)$$

where  $p$  is the parameter determining the shear deformation component of the flux shape function. Lliboutry (1979) suggested that it is approximately given by:

$$p = n - 1 + \frac{Q}{RT_b^2} G_0 H, \quad (3.17)$$

where  $n$  is the exponent of Glen's law in Eq. (3.4),  $Q = 6 \times 10^4$  J mol<sup>-1</sup> is the activation energy,  $R = 8.3145$  J mol<sup>-1</sup> K<sup>-1</sup> is the gas constant,  $T_b$  is the basal temperature, and  $G_0$  (K m<sup>-1</sup>) is the vertical temperature gradient at the bottom of the ice column.

In Dome C, using the values  $n = 3$ ,  $G_0 = 21.62$  K km<sup>-1</sup>,  $H = 3266$  m and the current basal temperature  $T_b = 270.2$  K, Parrenin et al. (2007b) obtained a value  $p \approx 9$ . All the parameter values except  $T_b$  and  $H$  are assumed constant, and  $p$

remains almost constant during the simulation. However, tests of the model using Eq. (3.17) failed to produce thermal profiles close enough to the measured Dome C profile. Parrenin et al. (2007b) pointed out several reasons why this value of  $p$  could be invalid at Dome C, and estimated a value  $p = 1.97 \pm 0.93$  by inverse method. Due to this uncertainty on the value of the parameter  $p$ , we decided to set  $p$  as a free parameter within a range  $[0, 9]$  for which we will obtain a probability distribution.

The value of the sliding parameter  $s$  at Dome C is not well constrained, but Parrenin et al. (2007b) concluded that it is less than 0.3, and less than 0.1 with 50% confidence. As the value of the sliding parameter is not well defined, we set  $s$  as a free parameter within a range  $[0, 0.5]$ .

### 3.5.3 Shear heating

Preliminary attempts to model the temperature profile at Dome C showed that the profile could not be fitted without some internal heat sources, that we assumed to be shear heating. The heat produced by shear deformation  $\Omega$  ( $\mu\text{W m}^{-3}$ ), or simply 'shear heating rate' is given as (see appendix C):

$$\Omega = \frac{2}{A^{1/n}} (\dot{\epsilon}_{zz}^2 + \dot{\epsilon}_{xz}^2)^{\frac{n+1}{2n}}, \quad (3.18)$$

where  $\dot{\epsilon}_{zz} = \frac{\partial u_x}{\partial z}$  is given in Appendix A and  $\dot{\epsilon}_{xz}$  is given by:

$$\dot{\epsilon}_{xz} = \frac{1}{2} \frac{\partial u_x}{\partial z} = \frac{\bar{U}_x}{2H} \omega''[\zeta], \quad (3.19)$$

where  $\bar{U}_x$  is the average horizontal velocity and  $\omega''[\zeta] = \frac{\partial^2 \omega}{\partial \zeta^2}$  is the second  $\zeta$ -derivative of the flux shape function in Eq. (3.15). We calculate it as  $\bar{U}_x = v_{\text{sur}}/\omega'(1)$ , where  $v_{\text{sur}}$  is the surface ice velocity, relative to the bedrock. Estimates of ice velocity from geodetic surveys at Dome C are a few mm per year at the topographical dome, and  $15 \pm 10 \text{ mm yr}^{-1}$  at the drilling site by tying it to a point 25 km away (Vittuari et al., 2004).

Heat production rate in Eq. (3.18) depends on the Glen's exponent  $n$  and the flux function parameter  $p$ , that determines the shear deformation component of the flux shape function. The effect of these parameters on the temperature profile can be seen in Fig. 3.06. Different values for  $n$  and  $p$  lead to different vertical distribution and magnitude of the shear heating and different thermal profiles at the end of the simulation. The value of the Glen's exponent  $n$  is not well constrained at Dome C (Legresy et al., 2000). For this reason, we let  $n$  as a free parameter and attempt to obtain a probability distribution for its value at Dome C.

#### 3.5.4 Free parameters

We have introduced five parameters that we consider free: the basal heat flux  $q_b$ , the flux function parameter  $p$ , the Glen's exponent  $n$ , the ice-air temperature offset  $T_{\text{offset}}$ , and the sliding  $s$ . For each set of parameter values, we calculate a temperature-depth profile with our advective-conductive model.

We select randomly the values of the parameters within a plausible range of values and calculate a temperature profile that we compare with the one measured at Dome C. For each combination of parameters, we calculate the misfits to temperature and heat flux profiles as the root mean square (RMS) difference between calculated and measured profiles. The upper 200 m and the lower 80 m are excluded from this comparison, the former to avoid the effect of our oversimplistic modelization of the upper firn layer, the latter because no data is available below that depth. We retain a set of parameters if both misfits are less than cutoff values for temperature and heat flux.

We set these cutoffs in such a way that we eliminate as many trials as possible, while keeping enough to obtain meaningful statistics. We set the temperature cutoff to 0.7 K and the heat flux cutoff to  $2 \text{ mW m}^{-2}$ . The procedure to obtain

these cutoffs is discussed in the appendix B.

Using these cutoff values, we retained  $\sim 0.25\%$  of all trials, obtaining histograms of accepted values for each free parameter. The number of accepted experiments within a range of values of the free parameters defines a probability density, from which we derive the mean and standard deviation to obtain the most likely values and a  $2\sigma$  confidence interval.

### 3.6 Initial conditions

The initial temperature profile of Dome C at 800 ka is impossible to determine from available data. However, because of the character of heat diffusion, the sensitivity of the temperature profile to the initial condition decreases with time. We performed several tests to confirm that the outcome of the simulations is independent of the initial temperature condition. We have thus used the same initial temperature profile for all simulations. This initial condition is obtained by applying the forward model to the present profile of Dome C, using as boundary conditions the time-reversed history of ice thickness, surface accumulation and SAT. The values of the free parameters are unknown for this backward-in-time simulation, but are not of critical importance because of the insensitivity to initial conditions. We chose basal heat flux  $q_b = 49.4 \text{ mW m}^{-2}$  (the apparent heat flux), while for the parameter  $p$ , the Glen's exponent, the surface velocity and the temperature offset we used  $p = 9$ ,  $n = 3$ ,  $v_{\text{sur}} = 15 \text{ mm yr}^{-1}$  and  $T_{\text{offset}} = 0 \text{ K}$ .

### 3.7 Results

The histograms show well marked peaks for the basal heat flux is  $q_b$ , the Glen's exponent  $n$  and the mean temperature offset  $T_{\text{offset}}$ , corresponding to the most likely values of the parameters are well marked. This suggest that the parameters are well constrained, except for the flux function parameter  $p$  and the sliding  $s$

(Fig. 3.07).

The most probable value for the basal heat flux is  $q_b = 51.1 \pm 1.4 \text{ mW m}^{-2}$ , slightly higher than the apparent heat flux of  $q_{b,app} = 49.4 \pm 1.1 \text{ mW m}^{-2}$  obtained from thermal conductivity and the thermal gradient at the lowermost 300 m of the measured profile, stopped 60 m above the bedrock. Scenarios with values of basal heat flux less than  $49 \text{ mW m}^{-2}$  are not accepted, while values as high as  $55 \text{ mW m}^{-2}$  produce profiles that are accepted. This is due to basal melting, because high values of basal heat flux keep the base of the glacier at melting point throughout the whole simulation. Higher basal heat flux increases melting while the base of the glacier stays at melting temperature, having little effect on the resulting profiles.

We have obtained a well constrained value for the Glen's exponent  $n = 1.91 \pm 0.11$ . This indicates that the Glen's exponent is critical to determine the magnitude of shear heating, without which the calculated temperature profiles can not fit that measured at Dome C.

The parameter  $p$  is not tightly constrained but low values of  $p$  are more likely, with a  $\sim 95\%$  probability for  $p < 7.4$ , and  $\sim 50\%$  probability for  $p < 1.8$ .

Sliding  $s$  is not well constrained, but the probability for  $s < 0.4$  is 95% and for  $s < 0.14$  is 50%. A higher sliding implies a smaller fraction of the glacier's movement at the top is due to shear deformation, producing less shear heating. However, shear heating also depends on the parameters  $p$  and  $n$ . The most critical parameter for shear heating is the Glen's exponent  $n$ , while it is much less sensitive to the parameters  $s$  and  $p$ . For this reason we obtain a well constrained peak for the Glen's exponent, while  $s$  and  $p$  could not be determined.

The most likely temperature offset between the IST and the SAT is  $T_{\text{offset}} =$

$0.36 \pm 1.2$  K. This result could be affected by errors on our estimation of the density and the thickness of the firn layer, as well as on the uniformity of the upper firn layer and the SAT reconstruction itself.

Finally, we used the numerical model to calculate a final present thermal profile, using the most likely values of the well constrained parameters  $q_b$ ,  $n$  and  $T_{\text{offset}}$  and the median values  $p = 1.8$  and  $s = 0.14$  for the poorly constrained parameters. The good match of the measured and calculated temperature profiles supports that the basal heat flux and the shear heating are in the correct range of values (Fig. 3.08).

### 3.8 Discussion and conclusions

In this study, we have modeled the ice flow and heat transport at Dome C with a 1-D thermal and mechanical model, using the reconstructions of air temperature, ice thickness and snow accumulation as boundary conditions. We have tuned key parameters of ice flow and thermal boundary conditions to fit the calculated temperature-depth profile to the measured thermal profile at Dome C, in order to obtain the most likely values of these parameters.

We have found that shear heating  $\Omega$  (determined by the parameters  $n$ ,  $p$  and  $s$ ) has a strong effect on the temperature profile. Attempts to fit the temperature and heat flux profiles without taking shear heating into consideration yielded profiles determined by the thermal boundary conditions at the surface and the base of the glacier (i.e., SAT and basal heat flux) but failed to explain the shape of the temperature-depth profile. For the highest estimates of basal heat flux (obtained from the temperature gradient near the base) the simulated temperature profiles were systematically  $\sim 5$  K colder than the one measured (Fig 3.09). Simple tests showed that both temperature and heat flux profiles could be fitted with a depth-uniform heating rate of  $\sim 3.5 \mu\text{W m}^{-3}$ , but a uniform heating rate has no physical

justification.

Shear heating is the only possible source of internal heating, but it varies with depth. The variation of shear heating with depth depends on the flux shape (Eq. (3.14)). Therefore it is possible to extract information about the flux shape function because it determines the goodness of the fit of the model to the profiles. The flux shape function is controlled by the parameter  $p$ , for which Lliboutry's approximation (Eq. 3.17) predicts values  $p \approx 9$ . Initial tests with this value failed to fit the Dome C profile satisfactorily, because shear heating was excessively concentrated in the lower part of the glacier (Fig 3.09). Parrenin et al. (2007b) argued that Eq. (3.17) is not applicable to Dome C, and found the most likely value for this parameter  $p = 1.97 \pm 0.93$ , based on a best fit of ice chronology to age markers. Although we have not been able to precisely determine the parameter  $p$ , our methodology suggests that the value of  $p$  is likely to be less than 3 and close to the value obtained by Parrenin et al. (2007b).

The Glen's exponent  $n$  is the main parameter controlling the magnitude of the shear heating through Eq. (3.18). An initial assumption  $n = 3$  for the Glen's exponent, the value assumed by Parrenin et al. (2007b), implied a shear heating too small to produce any significant difference in the simulated profiles. An initial trial letting the surface velocity at Dome C as a free parameter yielded velocities  $\approx 2000 - 3000$  times higher than the measurements of  $15 \pm 10$  mm/yr at Dome C (Vittuari et al., 2004). This was pointed out to us by Catherine Ritz (personal communication, December 12, 2016), and led us to reconsider the problem. We constrained the surface velocity and assumed Glen's exponent  $n$  to be undetermined at Dome C, as suggested by Legresy et al. (2000). We obtain a well constrained value  $n = 1.91 \pm 0.11$  at Dome C.

The mean temperature offset is also well constrained, but it is an operational

parameter that cannot be measured directly. The temperature offset varies during the year, but because seasonal signals are filtered as they propagate into the glacier, our model does not allow to obtain any information on this variability. This parameter is affected by the oversimplified model used for the firn at the top, which increases the uncertainty of our result. It has also been pointed out that the reconstruction of SAT could be flawed, as the relationship between water stable isotope ratios and temperature is not constant (Yang et al., 2018).

The basal heat flux value  $51.1 \text{ mW m}^{-2}$  is higher than the apparent heat flux near the base of the glacier. While we expected the shear heating to possibly overestimate the apparent heat flux, the melting is able to absorb more heat than that produced by shear deformation at the base. Because the apparent heat flux is estimated over 300 m, it may be slightly affected by shear heating near the base of the glacier. There is a very good fit between the Dome C profile and the thermal profile determined by the most likely values for our parameters, suggesting that these values are likely correct. The crust below East-Antarctica is believed to be made up of Archean and Proterozoic terranes that were welded together in the mid-Proterozoic (Dalziel, 1992; Harley, 2003). The value of  $51.1 \text{ mW m}^{-2}$  obtained for the heat flux below Dome C is well within the range of values characteristic of Archean or Proterozoic terranes (Jaupart & Mareschal, 2015). The heat flux value obtained is plausible and consistent with an estimate of heat flux beneath East Antarctica based on shear wave velocity profiles in the upper mantle (Shapiro & Ritzwoller, 2004). At Dome C, the horizontal velocity at the surface is very small and estimates of sliding, including our own, suggest very small movement at the base (Vittuari et al., 2004; Parrenin et al., 2007b). Dome C has experienced a constant heat flux for a time much longer than the characteristic heat conduction time, therefore we can be confident that the assumption of the heat flux at the base of the model as constant is correct.

The thermal model allows us to calculate basal melting dynamically. While basal melting does not have a direct feedback on our model, it is an important basal parameter that controls sliding. Solutions were obtained with high values of basal heat flux (higher than  $55 \text{ mW m}^{-2}$ ) that keep the base of the glacier at melting point. In this situation, increased basal heat flux can be absorbed by melting without affecting significantly the temperature profile. This has not been an issue in Dome C, but the method will not work for determining basal heat flux if it is high enough to keep the base of the glacier at melting point, unless we introduce another constraint on the melting rate. For Dome C we could determine an upper limit to melting, as both glacier height and accumulation follow prescribed histories. This upper limit is never reached through the simulations.

We have successfully used Monte-Carlo methods and a 1-D numerical model of heat and ice flow to produce constraints on several parameters of the glacier used in the numerical model, most significantly the basal heat flux  $q_b = 51.1 \pm 1.4(2\sigma) \text{ mW m}^{-2}$  and the Glen's exponent  $n = 1.91 + 0.11(2\sigma)$ , which had not been obtained for Dome C. Our methodology allows us to obtain this information from the thermal profile, which had been used before only to estimate basal heat flux without accounting for shear heating and melting. The success of the model at Dome C opens the gate to its application in other ice coring sites in Antarctica and Greenland.

### 3.9 Acknowledgements

Thanks to Catherine Ritz who provided us with the borehole temperature measurements.

This work was supported by grants from the Natural Sciences and Engineering Research Council of Canada Discovery grant (NSERC DG 140576948) and the Canada Research Program (CRC 230687) to H. Beltrami. H. Beltrami holds a

Canada Research Chair in Climate Dynamics. I. Hermoso de Mendoza is funded by a NSERC-CREATE Training Program in Climate Sciences based at St. Francis Xavier University.

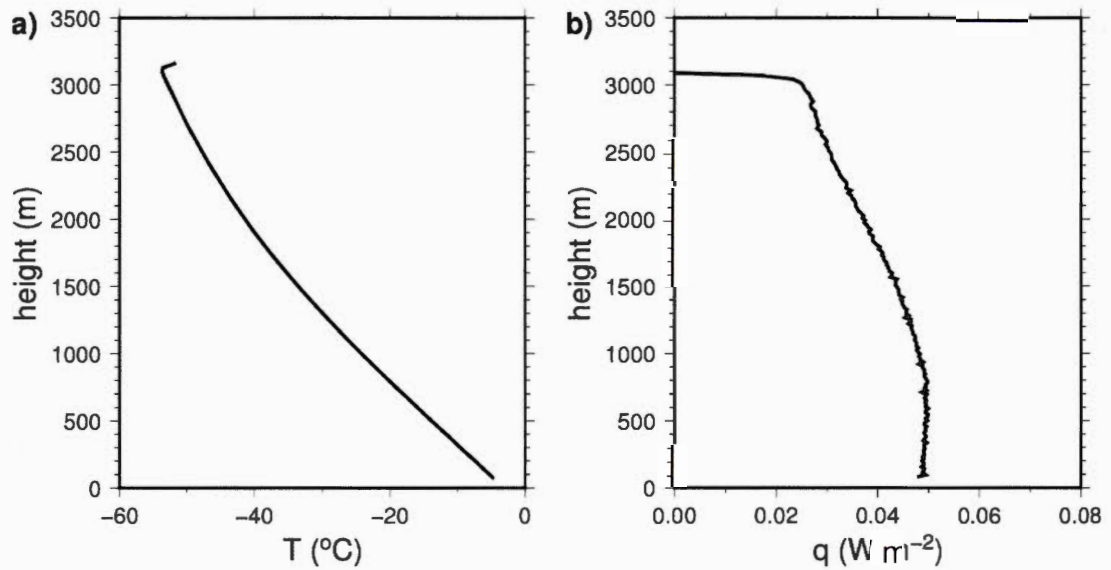


Figure 3.01: (a): Vertical temperature profile measured in Dome C. (b): Conductive heat flux profile, calculated from the temperature profile by Fourier law with a temperature-dependent thermal conductivity. Heat flux has been truncated for the upper 225 m because the temperature profile is very noisy near the surface of the ice sheet.

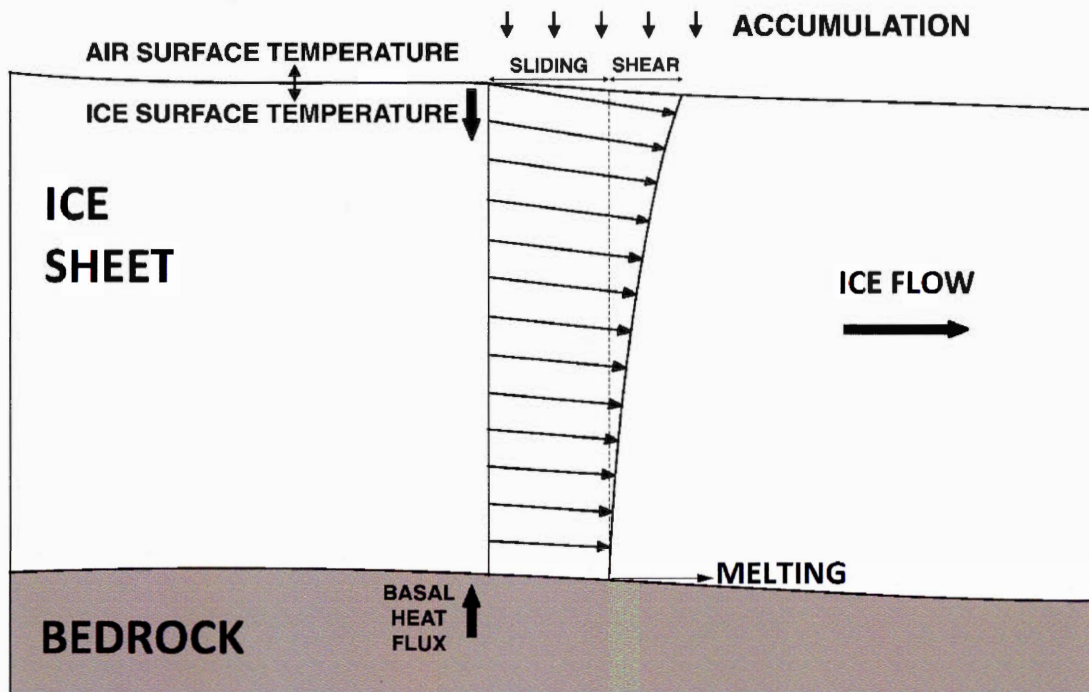


Figure 3.02: Sketch of flow in an ice sheet. The velocity of ice particles, both vertical and horizontal components, is highest near the surface and decreases at depth. The ice motion thins the ice layers and reduces the height of the glacier, while accumulation of snow at the surface increases its height. Temperature in the ice sheet increases downward, as heat flows out of the bedrock, and melting of ice could happen at the base. The ratio of the horizontal components of velocities at the bottom and at the surface of the ice defines the sliding ratio  $s$ .

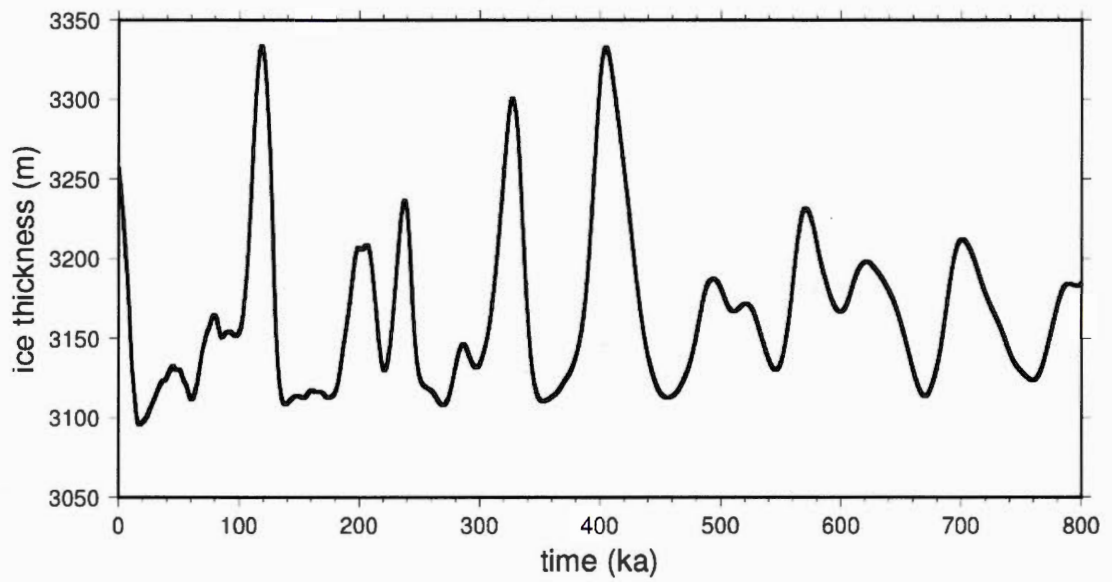


Figure 3.03: Variations of thickness in Dome C for the last 800 kyr, simulated with the linear perturbation model developed in Parrenin et al. (2007b).

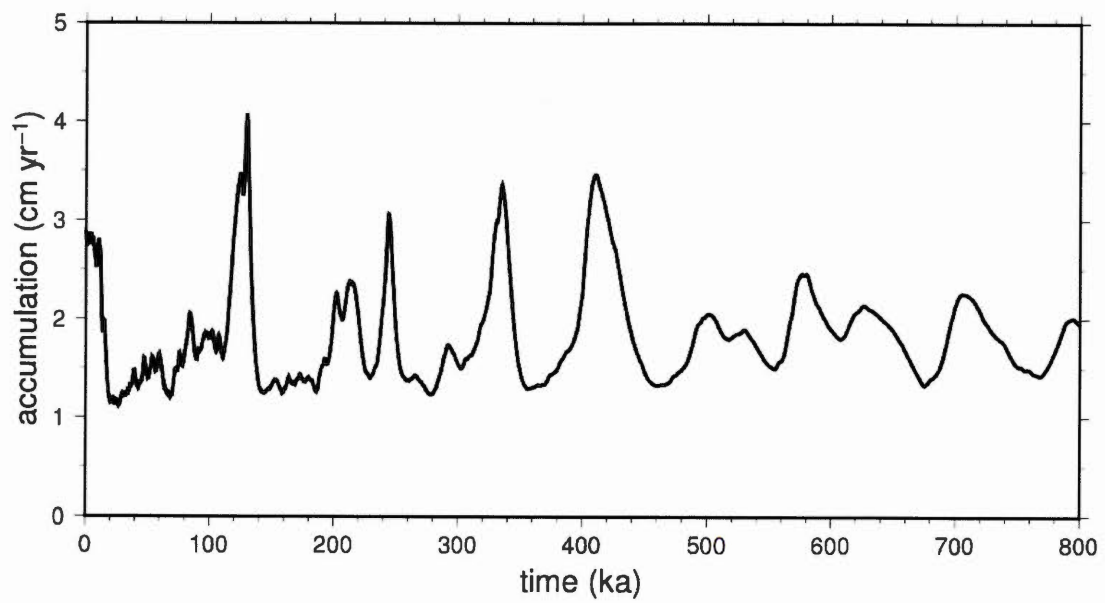


Figure 3.04: Surface accumulation rate history (in ice-equivalent units).

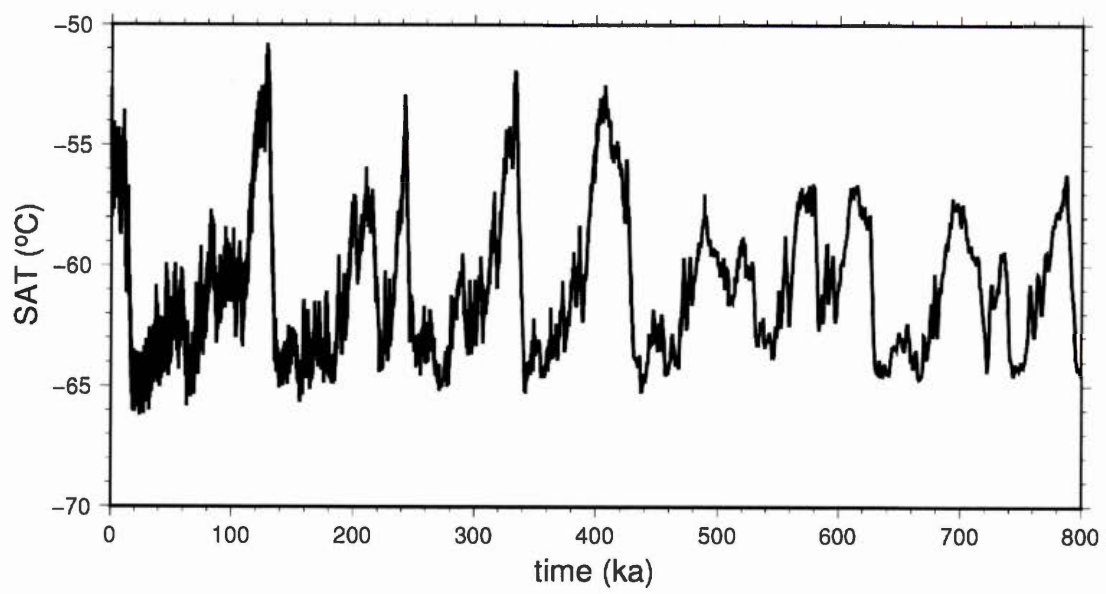


Figure 3.05: Surface Air Temperature (SAT) history.

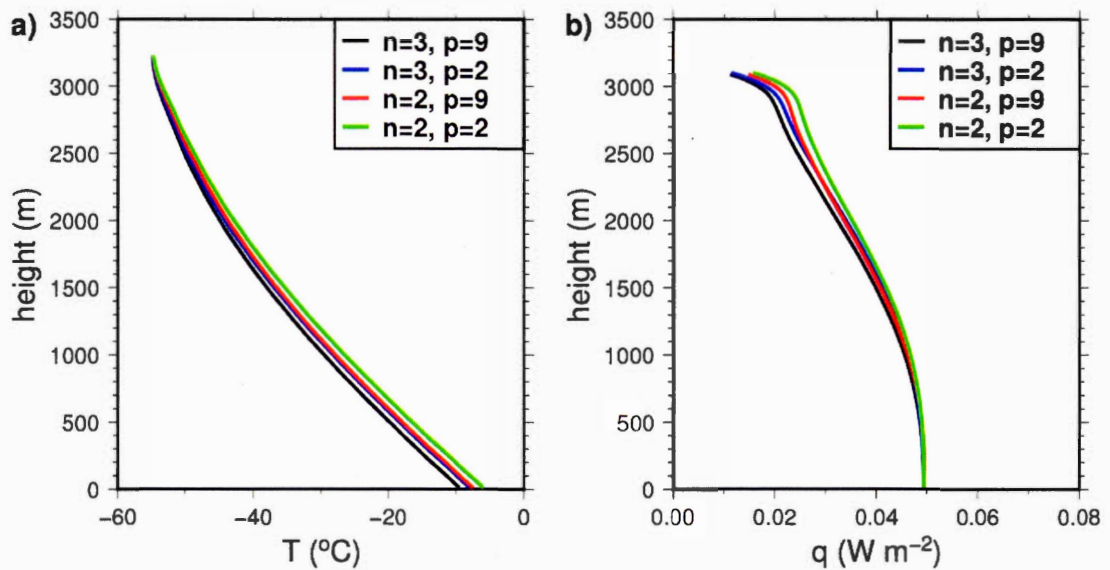


Figure 3.06: (a) Temperature-depth and (b) heat flux-depth profiles obtained at the end of the simulation with different values for the parameters  $n$  and  $p$ . Note how shear heating influences the shape of the temperature and heat flux profiles. The other parameters for these calculations are  $q_b = 49.4 \text{ mW m}^{-2}$ ,  $v_{\text{sur}} = 0.015 \text{ m yr}^{-1}$ , and  $T_{\text{offset}} = 0 \text{ K}$ .

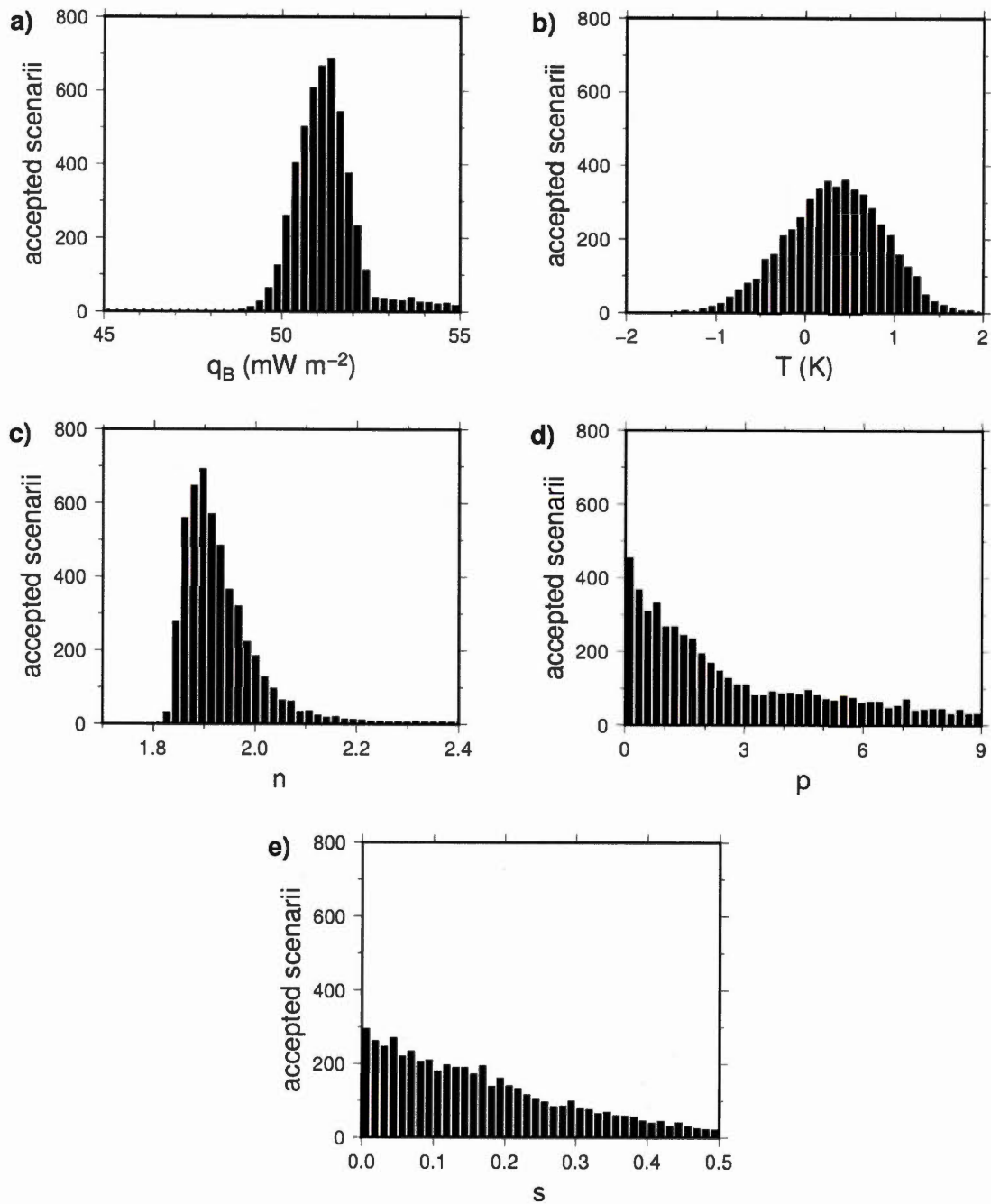


Figure 3.07: Histograms of retained values for the free parameters: (a) basal flux, (b) IST-SAT temperature offset, (c) Glen's exponent  $n$ , (d) flux function parameter  $p$ , and (e) sliding parameter  $s$ .

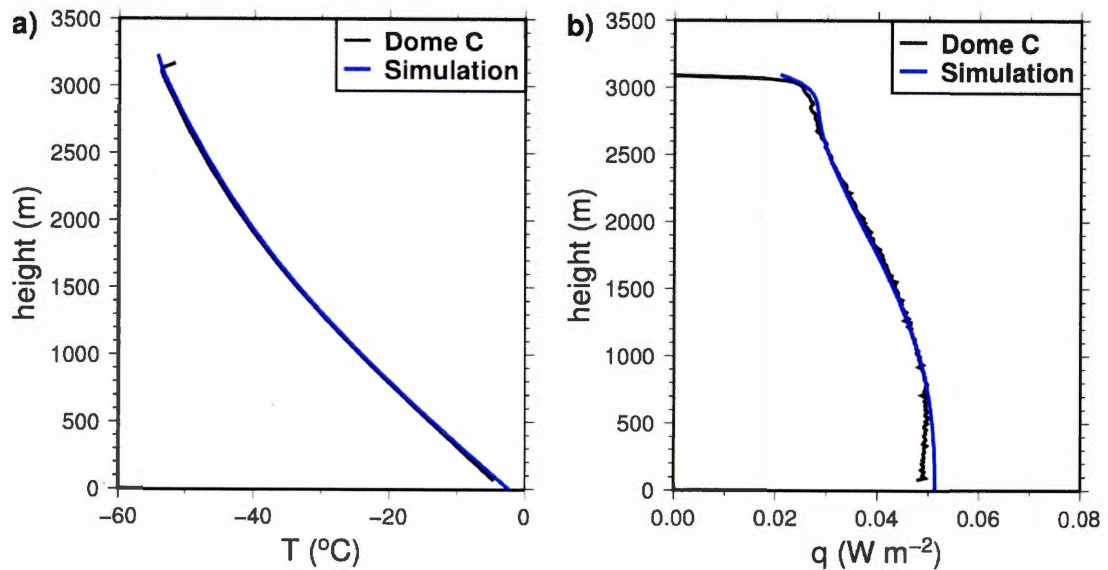


Figure 3.08: (a): Temperature-depth profile of Dome C (black) versus a simulation using  $p = 1.8$  and  $s = 0.14$  and the most likely values of the other parameters  $q_b = 51.1 \text{ mW m}^{-2}$ ,  $n = 1.91$  and  $T_{\text{offset}} = 0.36 \text{ K}$  (blue). (b): Conductive heat flux profile determined from the temperature profile, measured at Dome C (black) and calculated for the most likely values (blue).

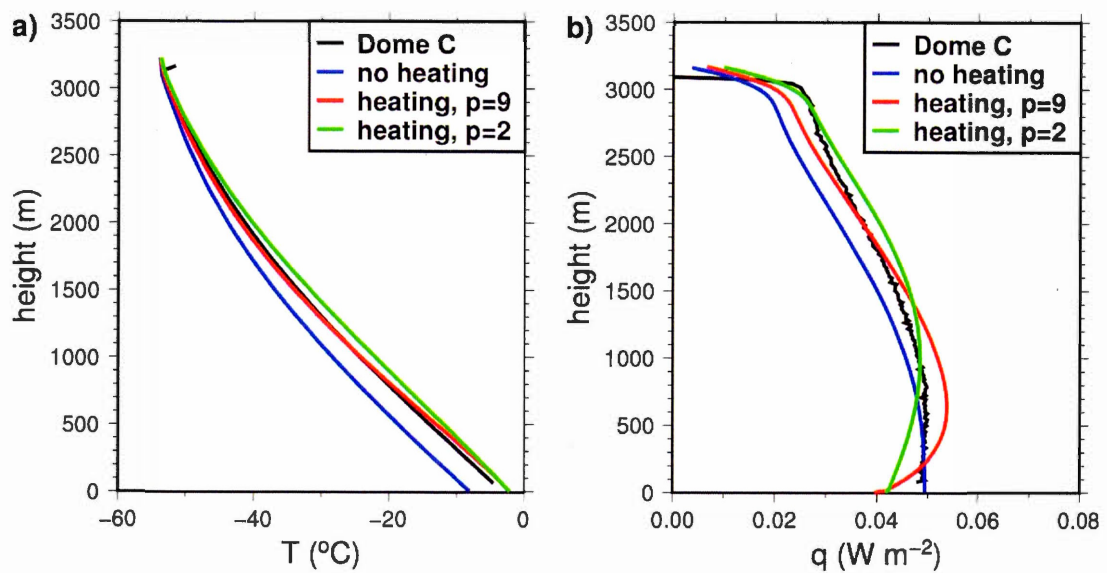


Figure 3.09: (a): Temperature-depth profile and (b) conductive heat flux profile determined from the temperature profile, measured at Dome C (black), calculated with artificially made zero shear heating (blue), calculated with shear heating and the theoretical value of the flux shape function parameter  $p = 9$ , and calculated with shear heating but  $p = 2$ . The values of the other parameters in the simulated profiles are  $n = 3$ ,  $s = 0.1$ ,  $q_b = 49.4 \text{ mW m}^{-2}$  and  $T_{\text{offset}} = 0 \text{ K}$ .

## CONCLUSION

This thesis groups three papers concerning the use of numerical models for the downward propagation of surface thermal signals. The objective of the first and second papers is to determine the effect that an inadequate bottom boundary condition in Land Surface Models (LSMs) has on heat storage, and the indirect repercussions on the rest of the model. The aim was to produce enough evidence for future land system modelers of the importance of using a realistic heat flux as bottom boundary condition for the subsurface and placing it at sufficient depth. The objective of the third paper is to produce constraints on glacier flow from the vertical temperature profile of the ice.

In the first chapter, we increased the depth of the bottom boundary from 42.1 m to 342.1 m and added a non-zero heat flux as bottom boundary condition in a LSM, the Community Land Model version 4.5 (CLM4.5). The original and modified versions of the CLM4.5 are run between the years 1901 and 2300, using historical forcing during the period 1901-2005 and two future scenarios of moderate (RCP 4.5) and high (RCP 8.5) emissions between 2005-2300. Our results show that increasing the thickness of the subsurface from 42.1 m to 342.1 m augments the heat stored in the subsurface between 1901 and 2300 by 217% in the Representative Concentration Pathway (RCP) 4.5 and 260% in the RCP 8.5. This result supports previous theoretical estimates that showed differences of one order of magnitude for the heat absorbed by a LSM during the 21st century between placing the bottom boundary at 10 m or at 600 m (Stevens et al., 2007). Because a thin subsurface underestimates the quantity of heat absorbed by the land model, it is redistributing this energy into other systems of the model. This energy

comes from the atmospheric system, so it would be mainly relocated to the other subsystem the atmosphere interacts with, the oceans. The energy gained by the continents in the last half of the 20th century is estimated to be  $9 \pm 1$  ZJ, whereas the oceans gained  $240 \pm 19$  ZJ (Beltrami et al., 2002; Levitus et al., 2012; Rhein et al., 2013). The heat gained in the continents is smaller than the uncertainty of the heat gained by the oceans, therefore, even though a big portion of the energy that should be absorbed by the land system would be misplaced into the oceanic system in a simulation, this would not be produce any significant effects.

However, we also see that a portion of this heat that is not absorbed by the deep subsurface remains in the land system, overheating the portion of the subsurface that is included in the model. In the part of the subsurface defined as soil, the upper 3.8 m, the original model (42.1 m) absorbs 1-3% more heat than the thickest model, which is large enough to affect locally the stability of permafrost. This result depends in the characteristics of the subsurface in CLM4.5, explicitly the thicknesses of the soil and the subsurface. Because the thermal signal is reflected upwards from the bottom boundary, the effect is larger for the portions of the subsurface closer to the bottom. A model using a more realistic soil thickness, which usually varies between 10-40 m with a global average of 13 m, would absorb more energy due to the effect of a shallow bottom boundary (Clair et al., 2015; Shangguan et al., 2017). The subsurface thickness of 42.1 m in CLM4.5 is by far the thickest among the models used in Climate Model Intercomparison Project phase 5 (CMIP5), most of which place the bottom boundary between 3 m to 10 m (Cuesta-Valero et al., 2016). The overheating effect for the soil in these models, and therefore the associated effects, can be expected to be much larger than for the CLM4.5.

In the second chapter, we studied how the depth and condition at the bottom boundary affect other elements of the CLM4.5: depth and areal extent of per-

mafrost, the evolution of the soil and vegetation carbon pools, and methane production. These effects are analyzed at two spatial scales: the regional scale of the Northern Hemisphere permafrost region, where the effects are expected to be maximal, and at the local scale of the land cells, defined by the spatial discretization of the numerical model. In the permafrost region, the evolution of permafrost is affected by the depth of the bottom boundary: the loss of near-surface permafrost area between 1901 and 2300 is reduced by 1.6% (RCP 4.5) to 1.9% (RCP 8.5) when the thickness of the subsurface is increased from 42.1 m to 342.1 m. It is safe to conclude that the overheating of the soil in a thin model reduces the stability of soil permafrost, though this reduction is small for CLM4.5. However, this overheating reduces greatly the stability of the intermediate-depth permafrost (upper 42.1 m), as increasing the subsurface thickness from 42.1 m to 342.1 m reduces the relative loss of permafrost between 1901 and 2300 from 42.2% to 7.8% in the RCP 4.5 scenario and from 72.7% to 13.4% in the RCP 8.5 scenario. Therefore, for subsurface models using a more realistic value of regolith thickness between 10-40 m, the depth of bottom boundary would have a larger effect on soil permafrost than it has in CLM4.5.

As deepening the bottom boundary from 42.1 m to 342.1 m increases the stability of permafrost, it reduces the loss of soil carbon in the Northern Hemisphere permafrost region by 1.3% (RCP 4.5) to 3.6% (RCP 8.5), lowers the stable vegetation level reached after 2100 by 0.1% (RCP 4.5) to 0.4% (RCP 8.5) and produces variations of 0.3% (RCP 4.5) to 0.5% (RCP 8.5) in methane production. The effects in vegetation are insignificant and the variations in methane production are small and unreliable, due to unrealistic hydrology model in CLM4.5, but the effect in soil carbon is considerable. As most of the soil carbon is located within the upper 3 m, we should not expect these results to be affected by the unrealistically thin soil used in CLM4.5. In the natural permafrost however, additional reserves exist

below 3 m which contain  $\sim 60\%$  as much carbon as the upper 3 m (Hugelius et al., 2014). A model including these additional reserves must use realistic regolith thickness and a sufficiently deep bottom boundary to avoid underestimating the stability of this deep soil carbon.

The bottom heat flux warms slightly the soil, and the reduction of extent and thickness of near-surface permafrost is small. However, the bottom heat flux determines the thermal steady state of the subsurface, which in a LSM is used to obtain the initial thermal state, and therefore it affects the initial size of the soil carbon pool. Because the time variations of the soil carbon pool depend on the size of this pool, we see a decrease in the loss of soil carbon during the simulation, from 1.1% (RCP 4.5) to 5.6% (RCP 8.5), when we increase the bottom heat flux by  $20 \text{ mW m}^{-2}$ . This points to the importance of initialization for LSMs. The method followed in CLM4.5 is the standard for LSMs, where the model is driven from initial conditions to a steady state, which is determined by the atmospheric inputs to the land system during the initialization period. However, in the real subsurface the temperature-depth profiles of the subsurface are not a steady state but a superposition of the steady state and the record of past atmospheric temperatures, which is the base of borehole climatology (Beltrami & Mareschal, 1991; González-Rouco et al., 2009). This is not relevant in LSMs with shallow bottom boundaries because the subsurface adapts quickly to the Ground Surface Temperature (GST) signal, but for LSMs with bottom boundaries at depths of hundreds of meters, the initial temperature of the subsurface has an effect lasting the whole duration of the simulation. A possible solution is the use in LSM of subsurface temperature data from borehole measurements to initialize the subsurface. It is worth asserting the importance of this issue, which would be a logical continuation of the present work.

The local variability of the results across the Northern Hemisphere permafrost

region is difficult to interpret with certainty. Increasing the thickness of the subsurface or the crustal heat flux reduces the size of the carbon pools and the production of methane in some areas, but it increases it in others. There is a possible explanation for the local differences found in the production of methane: the increase in Active Layer Thickness (ALT) allows more methane to be produced if there is still a frozen soil layer beneath, restricting the seepage of water and allowing the active layer to be inundated, however if the entirety of the soil thaws, the water can percolate to the aquifer and less methane is produced. This might also explain the local differences in the size of the carbon pool, as the differences in the production of methane accumulate over time. The local differences in vegetation carbon are more difficult to interpret, but the dominant trend is that warmer soil (because of a larger crustal heat flux or a thinner subsurface) results in more vegetation carbon in the coldest areas of the permafrost region, and less vegetation carbon in the periphery. A tentative explanation is that, while a warmer soil favors the colonization of plants, it may result in less available water in areas where additional heat thaws the soil completely and allows water to percolate to the aquifer and slightly reduce the growth of the vegetation.

The small magnitude of the effects on vegetation carbon raises the question of whether they could be completely due to statistical noise. Increasing the depth of the bottom boundary or the crustal heat flux produces a decrease in the vegetation carbon pool that is smaller than the yearly variations in the size of this pool. These yearly variations are due to fluctuations in precipitation and solar radiation, which can be considered as noise in the numerical model. However, increasing the crustal heat flux or the depth of the model induces a decrease in the size of the vegetation carbon pool that is consistent in time. Therefore, this decrease is not noise, despite being quantitatively small. However, it is too small to be considered an important result.

Finally, the main concern in the interpretation of these results is their relevance for the whole of a Earth System Model (ESM) simulation. The effects of our changes in the thermal state of the subsurface result in variations on the soil carbon pool as permafrost carbon is released to the atmosphere, part of which would be absorbed by the oceans. From anthropogenic carbon emissions levels of 6.8 PgC/yr at 2000, carbon emissions stabilize at 2100 to 4.1 PgC/yr in the RCP 4.5 scenario, and to 22.6 PgC/yr in the RCP 8.5 scenario (Thomson et al., 2011; Riahi et al., 2011). In contrast, in the simulations for the original CLM4.5, the soil carbon pool in the Northern Hemisphere permafrost region decreases between 2000 and 2100 by 0.89 PgC in the RCP 4.5 scenario and by 4.87 PgC in the RCP 8.5 scenario. This carbon is released to the atmosphere during the 21st century, but corresponds to roughly one fifth of the anthropogenic emissions for just the year 2100. The effect of increasing the thickness of the subsurface from 42.1 m to 342.1 m is to release additional permafrost soil carbon to the atmosphere: 0.074 PgC in the RCP 4.5 scenario and 0.099 PgC in the RCP 8.5 scenario. Using a crustal heat flux of  $60 \text{ mW m}^{-2}$ , because of the effect on the initial size of the soil carbon pool, results in a higher soil carbon content in the Northern Hemisphere permafrost region than in the original model at 2100: 0.46 PgC in the RCP 4.5 scenario and 0.414 PgC in the RCP 8.5 scenario. These differences are very small compared to yearly anthropogenic emission for both scenarios, let alone the entirety of the 21st century emissions. Therefore, it has to be concluded that the use of unrealistic bottom boundary conditions for the subsurface model in CLM4.5 does not have a significant impact on the other components of the Community Earth System Model version 1.2 (CESM1.2).

There are several lines of research that can be derived from this work. As we have exposed, the initial state of a LSM has long term consequences on the evolution of the simulations. While LSMs use spin-up simulations to drive the model

from to a steady state, this does not necessarily correspond to the state of the natural world at the initial time of the simulation. This is particularly true for natural systems with long-term memory, such as the subsurface (Beltrami, 2002; González-Rouco et al., 2009). A future line of research would therefore be the creation of a dataset of subsurface temperatures using borehole data, to use in the initialization of LSMs. Other possible expansions of this work would investigate how the simulation of a LSM is affected by other common simplifications of the subsurface, such as bedrock homogeneity or uniform regolith depth, as we have done for the impacts of the crustal heat flux and the subsurface thickness in this thesis.

In the third chapter titled « Constraints on glacier flow from temperature-depth profiles in the ice. Application to EPICA Dome C », we have used a Monte-Carlo method to constrain several parameters of glacier flow in the EPICA Dome C site in East Antarctica. We were able to obtain well-constrained values for the basal heat flux at the bottom of the glacier, the Glen's exponent, and the air-ice temperature coupling. These are parameters that affect the shape of the thermal profile directly, as they are the main factors determining the temperature gradient, the heat production and the surface temperature, respectively. Our approach is therefore able to estimate the values of the parameters of the glacier that determine the present vertical temperature profile, because this is the element used to test the different combinations of parameters. The present thermal profile at Dome C is less dependent on the sliding and the flux function than on the above parameters. For this reason the method was not able to obtain well-constrained values for the sliding and the flux shape function, though it was able to estimate a probability distribution for them.

The successful use of the temperature-depth profile measured at EPICA Dome C to constrain several parameters of glacier flow suggests that same methodology

can be applied to other glacier temperature profiles. A potential limitation comes from the presence of melting at the base of the glacier, since it keeps the base at melting temperature if the basal heat flux is higher than a certain value, thus introducing a bias towards higher estimates of basal heat flux. This problem could be solved by the introduction of new constraints, such as independent estimates of basal melting. Another key constraint for the model was the surface speed of the glacier, obtained from geodetic data. Because the generation of heat at any depth is directly proportional to the surface speed, a fixed value of the surface speed allowed to calculate the Glen's exponent with a high degree of certainty. The lack of a certain value for the surface speed would be a limitation for the application of the method in other sites, which would require additional constraints on the generation of heat.

Another limitation comes from the lack of initial conditions for the numerical model. Under the same parameters, different initial temperature profiles converge to the same final profile, which allows arbitrary initial conditions to be used within reasonable limits. The convergence of initial conditions can take variable times in the order of 10-30 kyr; therefore, the history of 800 kyr that can be reconstructed from the ice core at Dome C allows the method to be used at this location without knowledge of the initial conditions. The numerical model can also be used in the Greenland ice sheet, where the ice is 110 kyr old (Johnsen et al., 1995; Dahl-Jensen et al., 1998). However, the model can not be applied to high-mountain ice cores, where records are much shorter ( $\approx$  5-25 kyr) and ice flow is driven by slopes and more rapid than in Antarctica (Tandong & Thompson, 1992; Thompson et al., 1998).

## APPENDIX A

### CONSTRAINTS ON GLACIER FLOW FROM TEMPERATURE-DEPTH PROFILES IN THE ICE. APPLICATION TO EPICA DOME C: NUMERICAL MODEL

The forward model simulates the thermal and mechanical processes at Dome C for the past 800 kyr, the time period for which data of air temperature and snow accumulation are available. To numerically resolve the equations, we discretize time with a time-step  $dt$  and discretize space by dividing the vertical ice column in homogeneous layers of variable thickness  $\Delta z$ . We have chosen a time-step of 1 year, which offers a resolution higher than that of the data on temperature and accumulation rates. Because we use an explicit scheme for solving the heat equation, the ice layers must be thicker than a minimum value to ensure the convergence of the solution.

#### 1.1 Layer discretization and thinning

We model the ice sheet at Dome C as an ice column discretized in layers of thickness  $\Delta z$ , which decreases in time. Given the vertical velocity  $u_z[z]$ , we can calculate the thinning of ice layers from the vertical strain rate  $\dot{\epsilon}_{zz}$ :

$$\dot{\epsilon}_{zz} = \frac{\partial u_z[z]}{\partial z} = -\frac{1}{H} \left( a - \frac{\partial H}{\partial t} - m \right) \omega'[\zeta], \quad (\text{A.1})$$

where  $\omega'[\zeta]$  is the  $\zeta$ -derivative of the flux shape function in equation (3.15):

$$\omega'[\zeta] = s + (1 - s)\omega'_D[\zeta], \quad (\text{A.2})$$

where  $s$  is the sliding ratio and the  $\zeta$ -derivative of the deformation component of the flux shape function:

$$\omega'_D[\zeta] = \frac{p+2}{p+1} (1 - (1 - \zeta)^{p+1}). \quad (\text{A.3})$$

With the definition of  $\dot{\epsilon}_{zz}$ , the thickness  $\Delta z$  of a layer at time  $t + dt$  is computed as:

$$\Delta z_{t+dt} = \Delta z_t \times (1 + \dot{\epsilon}_{zz} dt). \quad (\text{A.4})$$

The ice sheet grows continuously due to compaction of accumulated snow. We simulate this process by letting the top ice layer thicken with accumulation, and when reaching the maximal thickness of 60 m, splitting it in two layers of equal thickness. On top of the ice layers we place a layer of firn, with a fixed thickness of 80 m and a density 75% that of ice. These values are estimated by averaging firn density data at Dome C (Arnaud et al., 2000). This layer is used for temperature calculations but it is not subject to mechanical thinning nor taken into account for flow calculations. Accumulation is added directly to the first ice layer directly below the firn layer, as we assume that, at the base, a mass of firn equal to the mass of snow accumulated at the top of the firn is instantly compacted into ice.

Through Eq. (A.4) the thicknesses of the ice layers decrease in time and therefore in depth, becoming extremely thin at the bottom. To ensure the convergence of heat conduction calculations, we merge neighbouring layers when their thickness drops below 15 m.

Each ice layer is homogeneous and has temperature-dependent thermal properties. The dependence of thermal conductivity  $\lambda$  ( $\text{W m}^{-1} \text{K}^{-1}$ ) and specific heat  $c_p$

( $\text{J kg}^{-1} \text{K}^{-1}$ ) on temperature for ice were taken from Handbook (2012), where values of  $\lambda$  and  $c_p$  for ice are tabulated for different temperatures. We fitted these values to polynomial functions, to have continuous functions. Thermal properties for the firn were taken from Jordan (1991b).

## APPENDIX B

### CONSTRAINTS ON GLACIER FLOW FROM TEMPERATURE-DEPTH PROFILES IN THE ICE. APPLICATION TO EPICA DOME C: METHOD SENSITIVITY

As remarked before, we accept experiments when the misfit between the calculated and the measured profiles of both temperature and heat flux are below two cutoff values, that we set as  $T_{\text{cutoff}} = 0.7$  K and  $q_{\text{cutoff}} = 2$  mW m<sup>-2</sup>. The value for the peak for  $q_b$  is weakly dependent on these values, but fluctuates when we reject too many experiments (because there are not enough experiments to make reliable statistics), and when accepting too many experiments we tend to a flat histogram.

For this reason, we want to keep the value of the cutoffs as low as possible, otherwise the results would be meaningless. If the value is too small, the retained parameters will not yield a meaningful histogram. To decide the appropriate value, we examined how the value of the basal heat flux  $q_b$  shifts with the value of the cutoffs.

The variation of the heat flux peak position is minimal around the values  $T_{\text{cutoff}} = 0.7$  K and  $q_{\text{cutoff}} = 2$  mW m<sup>-2</sup>, therefore we selected these values as our cutoffs (Fig. 2.01). To accept an experiment in our histogram, we require both misfits of temperature and heat flux to be below their respective cutoffs. Under these conditions, only  $\sim 0.25\%$  of 2.4 million trials are accepted, sufficient to yield

reliable statistics.

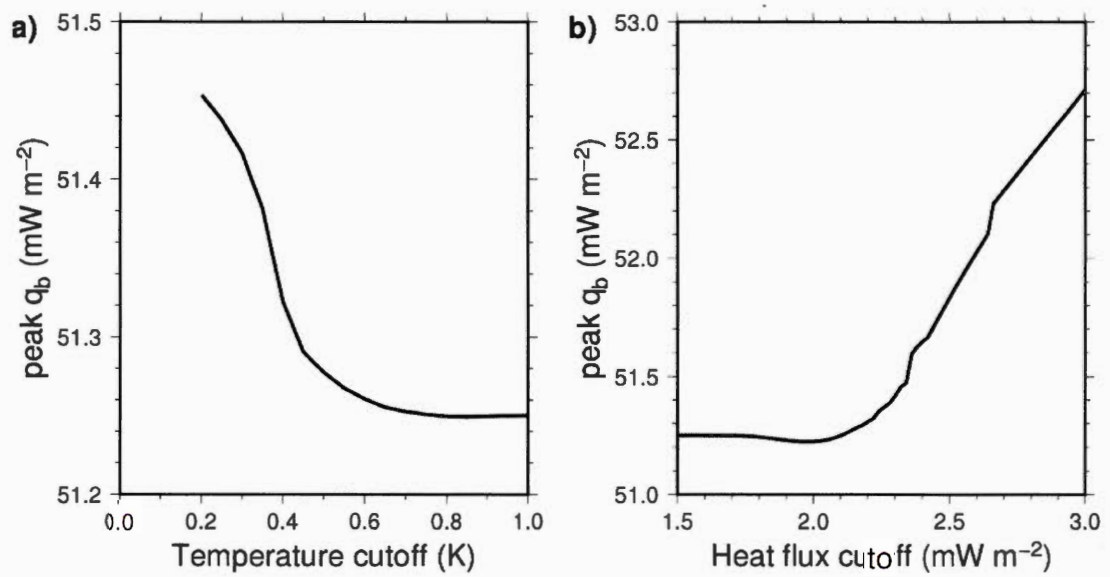


Figure 2.01: Change in the position of the  $q_b$  peak, as function of: a) The temperature cutoff  $T_{\text{cutoff}}$ , with heat flux cutoff set to  $q_{\text{cutoff}} = 2 \text{ mW m}^{-2}$ , and b) The heat flux cutoff  $q_{\text{cutoff}}$ , with temperature cutoff set to  $T_{\text{cutoff}} = 0.7 \text{ K}$ .

## APPENDIX C

### CONSTRAINTS ON GLACIER FLOW FROM TEMPERATURE-DEPTH PROFILES IN THE ICE. APPLICATION TO EPICA DOME C: CALCULATION OF SHEAR HEATING

$\Omega$  ( $\mu\text{W m}^{-3}$ ), the heat production due to shear deformation (Paterson, 1994), is given by:

$$\Omega = tr(\dot{\epsilon}\sigma) = \dot{\epsilon}_{xx}\sigma_x + \dot{\epsilon}_{yy}\sigma_y + \dot{\epsilon}_{zz}\sigma_z + 2\dot{\epsilon}_{xz}\tau_{xz} + 2\dot{\epsilon}_{yz}\tau_{yz} + 2\dot{\epsilon}_{xy}\tau_{xy}, \quad (\text{C.1})$$

where  $\tau_{xz}$ ,  $\tau_{yz}$  and  $\tau_{xy}$  are the shear-stress components and  $\sigma_x$ ,  $\sigma_y$  and  $\sigma_z$  are the normal-stress components, being  $x$ ,  $y$  and  $z$  (m) the two horizontal and the one vertical coordinates, respectively. The components of strain rate and the stress are related through the Glen's law:

$$\dot{\epsilon}_{xx} = \frac{\partial u_x}{\partial x} = A\tau^{n-1}\sigma'_x, \quad (\text{C.2})$$

$$\dot{\epsilon}_{xz} = \frac{1}{2} \left( \frac{\partial u_x}{\partial z} + \frac{\partial u_z}{\partial x} \right) = A\tau^{n-1}\tau_{xz}, \quad (\text{C.3})$$

where  $u_i$  ( $\text{m s}^{-1}$ ) are the components of the ice velocity.  $\sigma'_x$  is defined as:

$$\sigma'_x = \sigma_x - \frac{1}{3}(\sigma_x + \sigma_y + \sigma_z), \quad (\text{C.4})$$

and therefore:

$$\sigma'_x + \sigma'_y + \sigma'_z = 0, \quad (\text{C.5})$$

$$\dot{\epsilon}_{xx} + \dot{\epsilon}_{yy} + \dot{\epsilon}_{zz} = \frac{\partial u_x}{\partial x} + \frac{\partial u_y}{\partial y} + \frac{\partial u_z}{\partial z} = 0. \quad (\text{C.6})$$

In Eq. (C.2) and Eq. (C.4),  $n$  is the Glen's exponent and  $A$  ( $\text{Pa}^{-n} \text{s}^{-1}$ ) is a quantity whose units depend on the Glen's exponent and that depends only on temperature:

$$A = A_0 \exp\left(-\frac{Q_0}{RT}\right), \quad (\text{C.7})$$

where  $A_0 = 3.985 \times 10^{-13} \text{Pa}^{-n} \text{s}^{-1}$ ,  $Q_0 = 6 \times 10^4 \text{J mole}^{-1}$  is an activation energy,  $R = 8.3145 \text{J mole}^{-1} \text{K}^{-1}$  is the ideal gas constant, and  $T$  (K) is the absolute temperature.

The quantity  $\tau$  is the effective shear stress, defined as:

$$2\tau^2 = \sigma'_x{}^2 + \sigma'_y{}^2 + \sigma'_z{}^2 + 2(\tau_{xz}^2 + \tau_{yz}^2 + \tau_{xy}^2). \quad (\text{C.8})$$

For the sake of simplicity, we assume a state of plane strain, with all components of velocity, strain and stress are independent of  $y$ , and their  $y$ -components  $u_y = 0$ ,  $\dot{\epsilon}_{yy} = 0$  and  $\sigma_y = 0$  are zero. Consequently, we have from Eq. (C.4) and Eq. (C.5):

$$\sigma'_x = -\sigma'_z = \frac{1}{2}(\sigma_x - \sigma_z), \quad (\text{C.9})$$

while Eq. (C.6) and Eq. (C.8) are reduced respectively to to:

$$\dot{\epsilon}_{xx} + \dot{\epsilon}_{zz} = \frac{\partial u_x}{\partial x} + \frac{\partial u_z}{\partial z} = 0, \quad (\text{C.10})$$

$$\tau^2 = \sigma'_x{}^2 + \tau_{xz}^2. \quad (\text{C.11})$$

With these simplifications, the heat production Eq. (C.1) becomes:

$$\Omega = \dot{\epsilon}_{xx}\sigma_x + \dot{\epsilon}_{zz}\sigma_z + 2\dot{\epsilon}_{xz}\tau_{xz} = 2\dot{\epsilon}_{xx}\sigma'_x + 2\dot{\epsilon}_{xz}\tau_{xz}. \quad (\text{C.12})$$

We can solve  $\tau$ ,  $\tau_{xz}$  and  $\sigma'_x$  from the Eqs. (C.2), (C.3) and (C.11). It gives:

$$\Omega = \frac{2}{A^{1/n}} (\dot{\epsilon}_{zz}^2 + \dot{\epsilon}_{xz}^2)^{\frac{n+1}{2n}}. \quad (\text{C.13})$$

The value of  $\dot{\epsilon}_{zz}$  is obtained from Eq. (A.1). Assuming the ice flow to be laminar ( $\frac{\partial u_x}{\partial x}=0$ ),  $\dot{\epsilon}_{xz}$ , Eq. (C.2) is reduced to:

$$\dot{\epsilon}_{xz} = \frac{1}{2} \left( \frac{\partial u_x}{\partial z} + \frac{\partial u_z}{\partial x} \right) = \frac{1}{2} \frac{\partial u_x}{\partial z}. \quad (\text{C.14})$$

The horizontal velocity  $u_x$  is unknown, but it varies with depth (Parrenin et al., 2006) as:

$$u_x = \bar{U}_x \omega'(\zeta), \quad (\text{C.15})$$

where  $\bar{U}_x$  is the average horizontal velocity at the surface of the glacier. Therefore, Eq. (C.14) can be written as:

$$\dot{\epsilon}_{xz} = \frac{1}{2} \frac{\partial u_x}{\partial z} = \frac{1}{2H} \bar{U}_x \omega''(\zeta). \quad (\text{C.16})$$

## BIBLIOGRAPHY

- Anderson, E. A. (1976). A point energy and mass balance model of a snow cover. *NOAA Technical Report NWS, 19*.
- Arnaud, L., Barnola, J. M. & Duval, P. (2000). Physical modeling of the densification of snow/firn and ice in the upper part of polar ice sheets. In *Physics of ice core records*, pp. 285–305. Hokkaido University Press. <http://dx.doi.org/2115/32472>
- Augustin, L., Barbante, C., Barnes, P. R., Barnola, J. M., Bigler, M., Castellano, E., Cattani, O., Chappellaz, J., Dahl-Jensen, D., Delmonte, B. et al. (2004). Eight glacial cycles from an antarctic ice core. *Nature, 429*, 623–628. <http://dx.doi.org/10.1038/nature02599>
- Avis, C. A., Weaver, A. J. & Meissner, K. J. (2011). Reduction in areal extent of high-latitude wetlands in response to permafrost thaw. *Nature Geoscience, 4*(7), 444. <http://dx.doi.org/10.1038/NGE01160>
- Barnola, J.-M., Raynaud, D., Korotkevich, Y. S. & Lorius, C. (1987). Vostok ice core provides 160,000-year record of atmospheric co<sub>2</sub>. *Nature, 329*(6138), 408. <http://dx.doi.org/10.1038/329408a0>
- Beltrami, H. (2002). Earth's long-term memory. *Science, 297*(5579), 206–207. <http://dx.doi.org/10.1126/science.1074027>
- Beltrami, H. & Mareschal, J.-C. (1991). Recent warming in eastern Canada inferred from geothermal measurements. *Geophysical Research Letters, 18*(4), 605–608. <http://dx.doi.org/10.1029/91GL00815>

- Beltrami, H., Smerdon, J., Pollack, H. N. & Huang, S. (2002). Continental heat gain in the global climate system. *Geophysical Research Letters*, 29(8), 1–3. <http://dx.doi.org/10.1029/2001GL014310>
- Best, M. J., Pryor, M., Clark, D. B., Rooney, G. G., Essery, R. L. H., Ménard, C. B., Edwards, J. M., Hendry, M. A., Porson, A., Gedney, N., Mercado, L. M., Sitch, S., Blyth, E., Boucher, O., Cox, P. M., Grimmond, C. S. B. & Harding, R. J. (2011). The Joint UK Land Environment Simulator (JULES), model description. *Geoscientific Model Development*, (4), 677–699. <http://dx.doi.org/10.5194/gmd-4-677-2011>
- Bonan, G. B. (2008). Forests and climate change: forcings, feedbacks, and the climate benefits of forests. *Science*. <http://dx.doi.org/10.1126/science.1155121>
- Bray, N. (1988). Thermohaline circulation in the Gulf of California. *Journal of Geophysical Research: Oceans*, 93(C5), 4993–5020. <http://dx.doi.org/10.1029/JC093iC05p04993>
- Carlsaw, H. S. & Jaeger, J. C. (1959). Conduction of heat in solids. *Oxford: Clarendon Press, 1959, 2nd ed.* <http://dx.doi.org/10.1063/1.3057871>
- Clair, J. S., Moon, S., Holbrook, W., Perron, J., Riebe, C., Martel, S., Carr, B., Harman, C., Singha, K. et al. (2015). Geophysical imaging reveals topographic stress control of bedrock weathering. *Science*, 350(6260), 534–538. <http://dx.doi.org/10.1126/science.aab2210>
- Clark, P. U., Alley, R. B. & Pollard, D. (1999). Northern hemisphere ice-sheet influences on global climate change. *Science*, 286(5442), 1104–1111. <http://dx.doi.org/10.1126/science.286.5442.1104>

- Collins, M., Knutti, R., Arblaster, J., Dufresne, J. L., Fichet, T., Friedlingstein, P., Gao, X., Gutowski, W. J., Johns, T., Krinner, G., Shogwe, M., Tebaldi, C., Weaver, A. J. & Wehner, M. (2013). *Climate Change 2013: The Physical Science Basis. Long-term Climate Change: Projections, Commitments and Irreversibility*, In T. Stocker (ed.). *Climate Change 2013: The Physical Science Basis. Contribution of Working Group I to the Fifth Assessment Report of the Intergovernmental Panel on Climate Change*. Cambridge University Press.
- Cubasch, U., Wuebbles, D., Chen, D., Facchini, M., Frame, D., Mahowald, N. & Winther, J.-G. (2013). *Climate Change 2013: The Physical Science Basis. Introduction*, In *Climate Change 2013: The Physical Science Basis. Contribution of Working Group I to the Fifth Assessment Report of the Intergovernmental Panel on Climate Change*. Cambridge University Press.
- Cuesta-Valero, F. J., García-García, A., Beltrami, H. & Smerdon, J. E. (2016). First assessment of continental energy storage in CMIP5 simulations. *Geophysical Research Letters*, 43(10), 5326–5335. <http://dx.doi.org/10.1002/2016GL068496>
- Dahl-Jensen, D., Mosegaard, K., Gundestrup, N., Clow, G. D., Johnsen, S. J., Hansen, A. W. & Balling, N. (1998). Past temperatures directly from the greenland ice sheet. *Science*, 282(5387), 268–271. <http://dx.doi.org/10.1126/science.282.5387.268>
- Dalziel, I. W. (1992). Antarctica; a tale of two supercontinents? *Annual Review of Earth and Planetary Sciences*, 20(1), 501–526. <http://dx.doi.org/10.1146/annurev.ea.20.050192.002441>
- Fan, Y., Li, H. & Miguez-Macho, G. (2013). Global patterns of groundwater table depth. *Science*, 339(6122), 940–943. <http://dx.doi.org/10.1126/science.1229881>

- Fisher, A. T., Mankoff, K. D., Tulaczyk, S. M., Tyler, S. W., Foley, N. et al. (2015). High geothermal heat flux measured below the west antarctic ice sheet. *Science advances*, 1(6), e1500093. <http://dx.doi.org/10.1126/sciadv.1500093>
- Friend, A. D. & Kiang, N. Y. (2005). Land surface model development for the GISS GCM: Effects of improved canopy physiology on simulated climate. *Journal of Climate*, 18(15), 2883–2902. <http://dx.doi.org/10.1175/JCLI3425.1>
- Glen, J. W. (1955). The creep of polycrystalline ice. *Proc. R. Soc. Lond. A*, 228(1175), 519–538. <http://dx.doi.org/10.1098/rspa.1955.0066>
- González-Rouco, J., Beltrami, H., Zorita, E. & Stevens, M. (2009). Borehole climatology: a discussion based on contributions from climate modeling. *Climate of the Past*, 5(1), 97–127. <http://dx.doi.org/10.5194/cp-5-97-2009>
- Goujon, C., Barnola, J.-M. & Ritz, C. (2003). Modeling the densification of polar firn including heat diffusion: Application to close-off characteristics and gas isotopic fractionation for antarctica and greenland sites. *Journal of Geophysical Research: Atmospheres*, 108(D24). <http://dx.doi.org/10.1029/2002JD003319>
- Handbook, C. (2012). Crc handbook of chemistry and physics 2012-2013.
- Hansen, J. & Nazarenko, L. (2004). Soot climate forcing via snow and ice albedos. *Proceedings of the National Academy of Sciences*, 101(2), 423–428. <http://dx.doi.org/10.1073/pnas.2237157100>
- Harley, S. (2003). Archaean-cambrian crustal development of east antarctica: metamorphic characteristics and tectonic implications. *Geological Society, London, Special Publications*, 206(1), 203–230. <http://dx.doi.org/10.1144/GSL.SP.2003.206.01.11>

- Harris, I., Jones, P., Osborn, T. & Lister, D. (2014). Updated high-resolution grids of monthly climatic observations—the CRU TS3.10 Dataset. *International Journal of Climatology*, *34*(3), 623–642. <http://dx.doi.org/10.1002/joc.3711>
- Harris, S., French, H., Heginbottom, J., Johnston, G., Ladanyi, B., Sego, D. & van Everdingen, R. (1988). *Glossary of permafrost and related ground-ice terms*. Permafrost Subcommittee, National Research Council of Canada. Technical report, Technical memorandum
- Heimann, M. & Reichstein, M. (2008). Terrestrial ecosystem carbon dynamics and climate feedbacks. *Nature*, *451*(7176), 289. <http://dx.doi.org/10.1038/nature06591>
- Hermoso de Mendoza, I. (2018). Lower boundary conditions improvement in clm4.5. <http://dx.doi.org/10.5281/zenodo.1420497>. Retrieved from <https://zenodo.org/record/1420497>
- Hugelius, G., Strauss, J., Zubrzycki, S., Harden, J. W., Schuur, E., Ping, C.-L., Schirrmeister, L., Grosse, G., Michaelson, G. J., Koven, C. D. et al. (2014). Estimated stocks of circumpolar permafrost carbon with quantified uncertainty ranges and identified data gaps. *Biogeosciences*, *11*(23), 6573–6593. <http://dx.doi.org/10.5194/bg-11-6573-2014>
- Jaupart, C. & Mareschal, J.-C. (2010). *Heat generation and transport in the Earth*. Cambridge university press.
- Jaupart, C. & Mareschal, J.-C. (2015). *Heat flow and thermal structure of the lithosphere*, In A. Watts (ed.). *Treatise on Geophysics*, volume 6, (pp. 217–253). Elsevier BV, (2 éd.)

- Ji, D., Wang, L., Feng, J., Wu, Q., Cheng, H., Zhang, Q., Yang, J., Dong, W., Dai, Y., Gong, D. et al. (2014). Description and basic evaluation of Beijing Normal University Earth system model (BNU-ESM) version 1. *Geoscientific Model Development*, 7(5), 2039–2064. <http://dx.doi.org/10.5194/gmd-7-2039-2014>
- Johnsen, S. J., Dahl-Jensen, D., Dansgaard, W. & Gundestrup, N. (1995). Greenland palaeotemperatures derived from grip bore hole temperature and ice core isotope profiles. *Tellus B*, 47(5), 624–629. <http://dx.doi.org/10.1034/j.1600-0889.47.issue5.9.x>
- Jordan, R. (1991a). *A one-dimensional temperature model for a snow cover: Technical documentation for SNTHERM. 89*. Technical report, Cold Regions Research and Engineering Lab Hanover NH.
- Jordan, R. (1991b). *A one-dimensional temperature model for a snow cover: Technical documentation for SNTHERM. 89*. Technical report, DTIC Document
- Jouzel, J. (2007). Epica dome c ice core 800kyr deuterium data and temperature estimates. <http://dx.doi.org/10.1594/PANGAEA.683655>. Retrieved from [ftp.ncdc.noaa.gov/pub/data/paleo/icecore/antarctica/epica\\_domec/edc3deuttemp2007.txt](ftp.ncdc.noaa.gov/pub/data/paleo/icecore/antarctica/epica_domec/edc3deuttemp2007.txt)
- Jouzel, J., Masson-Delmotte, V., Cattani, O., Dreyfus, G., Falourd, S., Hoffmann, G., Minster, B., Nouet, J., Barnola, J.-M., Chappellaz, J. et al. (2007). Orbital and millennial antarctic climate variability over the past 800,000 years. *Science*, 317(5839), 793–796. <http://dx.doi.org/10.1126/science.1141038>
- Kalnay, E., Kanamitsu, M., Kistler, R., Collins, W., Deaven, D., Gandin, L., Iredell, M., Saha, S., White, G., Woollen, J. et al. (1996). The NCEP/NCAR 40-year reanalysis project. *Bulletin of the American meteorological Society*,

- 77(3), 437–471. [http://dx.doi.org/10.1175/1520-0477\(1996\)077<0437:TNYRP>2.0.CO;2](http://dx.doi.org/10.1175/1520-0477(1996)077<0437:TNYRP>2.0.CO;2)
- Kluzek, E. (2013). Cesm research tools: Clm4.5 in cesm1.2.0 user's guide documentation. Retrieved from <http://www.cesm.ucar.edu/models/cesm1.2/clm/models/lnd/clm/doc/UsersGuide/x12544.html>
- Koven, C. D., Riley, W. J. & Stern, A. (2013). Analysis of permafrost thermal dynamics and response to climate change in the CMIP5 Earth System Models. *Journal of Climate*, 26(6), 1877–1900. <http://dx.doi.org/10.1175/JCLI-D-12-00228.1>
- Koven, C. D., Ringeval, B., Friedlingstein, P., Ciais, P., Cadule, P., Khvorostyanov, D., Krinner, G. & Tarnocai, C. (2011). Permafrost carbon-climate feedbacks accelerate global warming. *Proceedings of the National Academy of Sciences*, 108(36), 14769–14774. <http://dx.doi.org/10.1073/pnas.1103910108>
- Lawrence, D., Fisher, R., Koven, C., Oleson, K., Swenson, S., Vertenstein, M. et al. (2018). *Technical Description of version 5.0 of the Community Land Model (CLM)*. Technical report, NCAR Technical Note NCAR/TN-503+ STR, Boulder, Colorado
- Lawrence, D. M. & Slater, A. G. (2005). A projection of severe near-surface permafrost degradation during the 21st century. *Geophysical Research Letters*, 32(24). <http://dx.doi.org/10.1029/2005GL025080>
- Legresy, B., Rignot, E. & Tabacco, I. E. (2000). Constraining ice dynamics at dome c, antarctica, using remotely sensed measurements. *Geophysical research letters*, 27(21), 3493–3496. <http://dx.doi.org/10.1029/2000GL011707>

- Lesperance, M., Smerdon, J. E. & Beltrami, H. (2010). Propagation of linear surface air temperature trends into the terrestrial subsurface. *Journal of Geophysical Research: Atmospheres*, 115(D21). <http://dx.doi.org/10.1029/2010JD014377>
- Levitus, S., Antonov, J. I., Boyer, T. P., Baranova, O. K., Garcia, H. E., Locarnini, R. A., Mishonov, A. V., Reagan, J., Seidov, D., Yarosh, E. S. et al. (2012). World ocean heat content and thermosteric sea level change (0–2000 m), 1955–2010. *Geophysical Research Letters*, 39(10). <http://dx.doi.org/10.1029/2012GL051106>
- Lliboutry, L. (1979). *A critical review of analytical approximate solutions for steady state velocities and temperature in cold ice-sheets.*
- MacDougall, A. H. & Beltrami, H. (2017). Impact of deforestation on subsurface temperature profiles: implications for the borehole paleoclimate record. *Environmental Research Letters*, 12(7), 074014. <http://dx.doi.org/10.1088/1748-9326/aa7394>
- MacDougall, A. H., Beltrami, H., González-Rouco, J. F., Stevens, M. B. & Bourlon, E. (2010). Comparison of observed and general circulation model derived continental subsurface heat flux in the Northern Hemisphere. *Journal of Geophysical Research: Atmospheres*, 115(D12). <http://dx.doi.org/10.1029/2009JD013170>
- MacDougall, A. H., González-Rouco, J. F., Stevens, M. B. & Beltrami, H. (2008). Quantification of subsurface heat storage in a GCM simulation. *Geophysical Research Letters*, 35(13). <http://dx.doi.org/10.1029/2008GL034639>
- Mareschal, J.-C. & Beltrami, H. (1992). Evidence for recent warming from per-

- turbed geothermal gradients: examples from eastern canada. *Climate Dynamics*, 6(3-4), 135–143. <http://dx.doi.org/10.1007/BF00193525>
- Marshall, S. J. (2005). Recent advances in understanding ice sheet dynamics. *Earth and Planetary Science Letters*, 240(2), 191–204. <http://dx.doi.org/10.1016/j.epsl.2005.08.016>
- McGuffie, K. & Henderson-Sellers, A. (2001). Forty years of numerical climate modelling. *International Journal of Climatology*, 21(9), 1067–1109. <http://dx.doi.org/10.1002/joc.632>
- Nicolson, D., Romanovsky, V., Alexeev, V. & Lawrence, D. (2007). Improved modeling of permafrost dynamics in a GCM land-surface scheme. *Geophysical research letters*, 34(8). <http://dx.doi.org/10.1029/2007GL029525>
- O'Connor, F. M., Boucher, O., Gedney, N., Jones, C., Folberth, G., Coppel, R., Friedlingstein, P., Collins, W., Chappellaz, J., Ridley, J. et al. (2010). Possible role of wetlands, permafrost, and methane hydrates in the methane cycle under future climate change: A review. *Reviews of Geophysics*, 48(4). <http://dx.doi.org/10.1029/2010RG000326>
- Oleson, K., Lawrence, D., Bonan, G., Drewniak, B., Huang, M. et al. (2013). *Technical Description of Version 4.5 of the Community Land Model (CLM)*. Technical report, NCAR Technical Note NCAR/TN-503+ STR, Boulder, Colorado
- Oppenheimer, M. (1998). Global warming and the stability of the West Antarctic Ice Sheet. *Nature*, 393(6683), 325. <http://dx.doi.org/10.1038/30661>
- Parrenin, F., Barnola, J.-M., Beer, J., Blunier, T., Castellano, E., Chappellaz, J., Dreyfus, G., Fischer, H., Fujita, S., Jouzel, J. et al. (2007a). The EDC3

- chronology for the EPICA Dome C ice core. *Climate of the Past*, 3(3), 485–497. <http://dx.doi.org/10.5194/cpd-3-575-2007>
- Parrenin, F., Dreyfus, G., Durand, G., Fujita, S., Gagliardini, O., Gillet, F., Jouzel, J., Kawamura, K., Lhomme, N., Masson-Delmotte, V. et al. (2007b). 1-D-ice flow modelling at EPICA Dome C and Dome Fuji, East Antarctica. *Climate of the Past*, 3(2), 243–259. <http://dx.doi.org/10.5194/cp-3-243-2007>
- Parrenin, F., Hindmarsh, R. & Rémy, F. (2006). Analytical solutions for the effect of topography, accumulation rate and lateral flow divergence on isochrone layer geometry. *Journal of Glaciology*, 52(177), 191–202. <http://dx.doi.org/10.3189/172756506781828728>
- Parrenin, F., Remy, F., Ritz, C., Siegert, M. J. & Jouzel, J. (2004). New modeling of the vostok ice flow line and implication for the glaciological chronology of the vostok ice core. *Journal of Geophysical Research: Atmospheres*, 109(D20). <http://dx.doi.org/10.1029/2004JD004561>
- Paterson, W. (1994). *The physics of glaciers*. Butterworth-Heinemann. [http://dx.doi.org/10.1002/\(SICI\)1096-9837\(199610\)21:10<980::AID-ESP586>3.0.CO;2-G](http://dx.doi.org/10.1002/(SICI)1096-9837(199610)21:10<980::AID-ESP586>3.0.CO;2-G)
- Pelletier, J. D., Broxton, P. D., Hazenberg, P., Zeng, X., Troch, P. A., Niu, G.-Y., Williams, Z., Brunke, M. A. & Gochis, D. (2016). A gridded global data set of soil, intact regolith, and sedimentary deposit thicknesses for regional and global land surface modeling. *Journal of Advances in Modeling Earth Systems*, 8(1), 41–65.
- Petit, J.-R., Jouzel, J., Raynaud, D., Barkov, N. I., Barnola, J.-M., Basile, I., Bender, M., Chappellaz, J., Davis, M., Delaygue, G. et al. (1999). Climate

- and atmospheric history of the past 420,000 years from the Vostok ice core, Antarctica. *Nature*, 399(6735), 429–436. <http://dx.doi.org/10.1038/20859>
- Phillips, N. A. (1956). The general circulation of the atmosphere: A numerical experiment. *Quarterly Journal of the Royal Meteorological Society*, 82(352), 123–164. <http://dx.doi.org/10.1002/qj.49708235202>
- Pickler, C., Beltrami, H. & Mareschal, J.-C. (2016). Laurentide ice sheet basal temperatures during the last glacial cycle as inferred from borehole data. *Climate of the Past*, 12(1), 115–127. <http://dx.doi.org/10.5194/cp-12-115-2016>
- Pitman, A. (2003). The evolution of, and revolution in, land surface schemes designed for climate models. *International Journal of Climatology*, 23(5), 479–510. <http://dx.doi.org/10.1002/joc.893>
- Pol, K., Masson-Delmotte, V., Johnsen, S., Bigler, M., Cattani, O., Durand, G., Falourd, S., Jouzel, J., Minster, B., Parrenin, F. et al. (2010). New MIS 19 EPICA Dome C high resolution deuterium data: Hints for a problematic preservation of climate variability at sub-millennial scale in the “oldest ice”. *Earth and Planetary Science Letters*, 298(1), 95–103. <http://dx.doi.org/10.1016/j.epsl.2010.07.030>
- Ramanathan, V. & Carmichael, G. (2008). Global and regional climate changes due to black carbon. *Nature geoscience*, 1(4), 221–227. <http://dx.doi.org/10.1038/ngeo156>
- Rhein, M., Rintoul, S., Aoki, S., Campos, E., Chambers, D., Feely, R. A., Gulev, S., Josey, G. C. J. S. A., Kostianoy, A., Mauritzen, C., Roemmich, D., Talley, L. D. & Wang, F. (2013). *Climate Change 2013: The Physical Science Basis. Observations: Ocean*, In *Climate Change 2013: The Physical Science Basis*.

- Contribution of Working Group I to the Fifth Assessment Report of the Intergovernmental Panel on Climate Change*, (pp. 264–265). Cambridge University Press.
- Riahi, K., Rao, S., Krey, V., Cho, C., Chirkov, V., Fischer, G., Kindermann, G., Nakicenovic, N. & Rafaj, P. (2011). RCP 8.5—A scenario of comparatively high greenhouse gas emissions. *Climatic Change*, 109(1-2), 33. <http://dx.doi.org/10.1007/s10584-011-0149-y>
- Riley, W., Subin, Z., Lawrence, D., Swenson, S., Torn, M., Meng, L., Mahowald, N. & Hess, P. (2011). Barriers to predicting changes in global terrestrial methane fluxes: analyses using CLM4Me, a methane biogeochemistry model integrated in CESM. *Biogeosciences*, 8(7), 1925–1953. <http://dx.doi.org/10.5194/bg-8-1925-2011>
- Ritz, C., Rommelaere, V. & Dumas, C. (2001). Modeling the evolution of Antarctic ice sheet over the last 420,000 years: Implications for altitude changes in the Vostok region. *Journal of Geophysical Research: Atmospheres*, 106(D23), 31943–31964. <http://dx.doi.org/10.1029/2001JD900232>
- Running, S. W. & Gower, S. T. (1991). FOREST-BGC, a general model of forest ecosystem processes for regional applications. II. Dynamic carbon allocation and nitrogen budgets. *Tree physiology*, 9(1-2), 147–160. [http://dx.doi.org/10.1175/1520-0442\(1997\)010<2040:LSMDFT>2.0.CO;2](http://dx.doi.org/10.1175/1520-0442(1997)010<2040:LSMDFT>2.0.CO;2)
- Running, S. W. & Hunt, E. R. (1993). *Generalization of a forest ecosystem process model for other biomes, BIOME-BCG, and an application for global-scale models*, In *Scaling Physiological Processes: Leaf to Globe*, (pp. 141–158). Elsevier
- Ruth, U., Barnola, J.-M., Beer, J., Bigler, M., Blunier, T., Castellano, E., Fischer, H., Fundel, F., Huybrechts, P., Kaufmann, P. et al. (2007). "EDML1": a

- chronology for the EPICA deep ice core from Dronning Maud Land, Antarctica, over the last 150 000 years. *Climate of the Past Discussions*, 3(2), 549–574. <http://dx.doi.org/10.5194/cp-3-475-2007>
- Scharlemann, J. P., Tanner, E. V., Hiederer, R. & Kapos, V. (2014). Global soil carbon: understanding and managing the largest terrestrial carbon pool. *Carbon Management*, 5(1), 81–91. <http://dx.doi.org/10.4155/CMT.13.77>
- Schmidt, G. A., Kelley, M., Nazarenko, L., Ruedy, R., Russell, G. L., Aleinov, I., Bauer, M., Bauer, S. E., Bhat, M. K., Bleck, R. et al. (2014). Configuration and assessment of the GISS ModelE2 contributions to the CMIP5 archive. *Journal of Advances in Modeling Earth Systems*, 6(1), 141–184. <http://dx.doi.org/10.1002/2013MS000265>
- Schuur, E., McGuire, A., Schädel, C., Grosse, G., Harden, J., Hayes, D., Hugelius, G., Koven, C., Kuhry, P., Lawrence, D. et al. (2015). Climate change and the permafrost carbon feedback. *Nature*, 520(7546), 171–179. <http://dx.doi.org/10.1038/nature14338>
- Seneviratne, S. I., Corti, T., Davin, E. L., Hirschi, M., Jaeger, E. B., Lehner, I., Orlowsky, B. & Teuling, A. J. (2010). Investigating soil moisture–climate interactions in a changing climate: A review. *Earth-Science Reviews*, 99(3-4), 125–161. <http://dx.doi.org/10.1016/j.earscirev.2010.02.004>
- Shangguan, W., Hengl, T., de Jesus, J. M., Yuan, H. & Dai, Y. (2017). Mapping the global depth to bedrock for land surface modeling. *Journal of Advances in Modeling Earth Systems*. <http://dx.doi.org/10.1002/2016MS000686>
- Shapiro, N. M. & Ritzwoller, M. H. (2004). Inferring surface heat flux distributions guided by a global seismic model: particular application to Antarctica. *Earth*

- and Planetary Science Letters*, 223(1-2), 213–224. <http://dx.doi.org/10.1016/j.epsl.2004.04.011>
- Slater, A. G. & Lawrence, D. M. (2013). Diagnosing present and future permafrost from climate models. *Journal of Climate*, 26(15), 5608–5623. <http://dx.doi.org/10.1175/JCLI-D-12-00341.1>
- Smerdon, J. E. & Stieglitz, M. (2006). Simulating heat transport of harmonic temperature signals in the earth's shallow subsurface: Lower-boundary sensitivities. *Geophysical research letters*, 33(14). <http://dx.doi.org/10.1029/2006GL026816>
- Spahni, R., Chappellaz, J., Stocker, T. F., Loulergue, L., Hausammann, G., Kawamura, K., Flückiger, J., Schwander, J., Raynaud, D., Masson-Delmotte, V. et al. (2005). Atmospheric methane and nitrous oxide of the late Pleistocene from Antarctic ice cores. *Science*, 310(5752), 1317–1321. <http://dx.doi.org/10.1126/science.1120132>
- Stern, I. (2013). Permafrost carbon rcn forcing data. Retrieved from [http://www.earthsystemgrid.org/dataset/ucar.cgd.cesm4.permafrostRCN\\_protocol2\\_forcing.html](http://www.earthsystemgrid.org/dataset/ucar.cgd.cesm4.permafrostRCN_protocol2_forcing.html)
- Stevens, M. B., Smerdon, J. E., González-Rouco, J. F., Stieglitz, M. & Beltrami, H. (2007). Effects of bottom boundary placement on subsurface heat storage: Implications for climate model simulations. *Geophysical research letters*, 34(2). <http://dx.doi.org/10.1029/2006GL028546>
- Stocker, T., Qin, D., Plattner, G. K., Tignor, M., Allen, S. K., Boschung, J., Nauels, A., Xia, Y., Bex, V. & Midgley, P. M. (2013). *Climate Change 2013: The Physical Science Basis*.

- Swenson, S., Lawrence, D. & Lee, H. (2012). Improved simulation of the terrestrial hydrological cycle in permafrost regions by the Community Land Model. *Journal of Advances in Modeling Earth Systems*, 4(3). <http://dx.doi.org/10.1029/2012MS000165>
- Tabacco, I., Passerini, A., Corbelli, F. & Gorman, M. (1998). Determination of the surface and bed topography at Dome C, East Antarctica. *Journal of Glaciology*, 44(146), 185–191. <http://dx.doi.org/10.3189/S0022143000002501>
- Tandong, Y. & Thompson, L. G. (1992). Trends and features of climatic changes in the past 5000 years recorded by the Dunde ice core. *Annals of Glaciology*, 16, 21–24. <http://dx.doi.org/10.3189/1992AoG16-1-21-24>
- Taylor, K. E., Stouffer, R. J. & Meehl, G. A. (2012). An overview of CMIP5 and the experiment design. *Bulletin of the American Meteorological Society*, 93(4), 485–498. <http://dx.doi.org/10.1175/BAMS-D-11-00094.1>
- Thompson, L. G., Davis, M. E., Mosley-Thompson, E., Sowers, T., Henderson, K. A., Zagorodnov, V. S., Lin, P.-N., Mikhailenko, V. N., Campen, R. K., Bolzan, J. F. et al. (1998). A 25,000-year tropical climate history from Bolivian ice cores. *Science*, 282(5395), 1858–1864. <http://dx.doi.org/10.1126/science.282.5395.1858>
- Thomson, A. M., Calvin, K. V., Smith, S. J., Kyle, G. P., Volke, A., Patel, P., Delgado-Arias, S., Bond-Lamberty, B., Wise, M. A., Clarke, L. E. et al. (2011). RCP4. 5: a pathway for stabilization of radiative forcing by 2100. *Climatic change*, 109(1-2), 77. <http://dx.doi.org/10.1007/s10584-011-0151-4>
- Thornton, P. E., Law, B. E., Gholz, H. L., Clark, K. L., Falge, E., Ellsworth, D. S., Goldstein, A., Monson, R. K., Hollinger, D., Falk, M. et al. (2002). Modeling and measuring the effects of disturbance history and climate on carbon and wa-

- ter budgets in evergreen needleleaf forests. *Agricultural and forest meteorology*, 113(1), 185–222. [http://dx.doi.org/10.1016/S0168-1923\(02\)00108-9](http://dx.doi.org/10.1016/S0168-1923(02)00108-9)
- Thornton, P. E. & Rosenbloom, N. A. (2005). Ecosystem model spin-up: Estimating steady state conditions in a coupled terrestrial carbon and nitrogen cycle model. *Ecological Modelling*, 189(1), 25–48. <http://dx.doi.org/10.1016/j.ecolmodel.2005.04.008>
- Van Vuuren, D. P., Edmonds, J., Kainuma, M., Riahi, K., Thomson, A., Hibbard, K., Hurtt, G. C., Kram, T., Krey, V., Lamarque, J.-F. et al. (2011). The representative concentration pathways: an overview. *Climatic change*, 109(1-2), 5. <http://dx.doi.org/10.1007/s10584-011-0148-z>
- Viovy, N. (2018). CRUNCEP Version 7 - Atmospheric Forcing Data for the Community Land Model. Retrieved from <http://rda.ucar.edu/datasets/ds314.3/>
- Vittuari, L., Vincent, C., Frezzotti, M., Mancini, F., Gandolfi, S., Bitelli, G. & Capra, A. (2004). Space geodesy as a tool for measuring ice surface velocity in the Dome C region and along the ITASE traverse. *Annals of Glaciology*, 39(1), 402–408. <http://dx.doi.org/10.3189/172756404781814627>
- Vostok, S. (2016). Federal Program 'World Ocean'. Antarctic Research and Investigation. Retrieved from [http://www.aari.aq/default\\_en.html](http://www.aari.aq/default_en.html)
- Wania, R., Ross, I. & Prentice, I. (2010). Implementation and evaluation of a new methane model within a dynamic global vegetation model: Lpj-whyme v1. 3.1. *Geoscientific Model Development*, 3(2), 565–584.
- Watanabe, O., Kamiyama, K., Motoyama, H., Fujii, Y., Shoji, H. & Satow, K. (1999). The paleoclimate record in the ice core at Dome Fuji station, East

- Antarctica. *Annals of Glaciology*, 29(1), 176–178. <http://dx.doi.org/10.3189/172756499781821553>
- Weaver, A. J., Eby, M., Wiebe, E. C., Bitz, C. M., Duffy, P. B., Ewen, T. L., Fanning, A. F., Holland, M. M., MacFadyen, A., Matthews, H. D. et al. (2001). The UVic Earth System Climate Model: Model description, climatology, and applications to past, present and future climates. *Atmosphere-Ocean*, 39(4), 361–428. <http://dx.doi.org/10.1080/07055900.2001.9649686>
- Wu, T., Song, L., Li, W., Wang, Z., Zhang, H., Xin, X., Zhang, Y., Zhang, L., Li, J., Wu, F. et al. (2014). An overview of BCC climate system model development and application for climate change studies. *Journal of Meteorological Research*, 28(1), 34–56. <http://dx.doi.org/10.1007/s13351-014-3041-7>
- Yang, J.-W., Han, Y., Orsi, A. J., Kim, S.-J., Han, H., Ryu, Y., Jang, Y., Moon, J., Choi, T., Hur, S. D. et al. (2018). Surface temperature in twentieth century at the styx glacier, northern victoria land, antarctica, from borehole thermometry. *Geophysical Research Letters*, 45(18), 9834–9842. <http://dx.doi.org/10.1029/2018GL078770>
- Yongjiu, D. & Qingcun, Z. (1997). A land surface model (IAP94) for climate studies part I: Formulation and validation in off-line experiments. *Advances in Atmospheric Sciences*, 14(4), 433–460. <http://dx.doi.org/10.1007/s00376-997-0063-4>